DEPARTAMENT DE FÍSICA ATÒMICA
MOLECULAR I NUCLEAR


VNIVERSITAT DE VALÈNCIA

# Integration and First Results of the Optical Beacon Calibration System of the ANTARES Neutrino Telescope

Treball d'Investigació

Francisco Salesa Greus

September 2006

D. JUAN JOSÉ HERNÁNDEZ REY, Investigador Científic del C.S.I.C, i
D. JUAN ZÚÑIGA ROMÁN, Profesor Titular de la Universitat de València,

CERTIFIQUEN:

Que la present memòria, **Integration and First Results of the Optical Beacon Calibration System of the ANTARES Neutrino Telescope** ha estat realitzada baix la seua direcció en el Institut de Física Corpuscular (Centre Mixt Universitat de València - CSIC) per D. Francisco Salesa Greus i constitueix el seu treball d'Investigació del Tercer Cicle que segueix en el Departament de Física Atòmica, Molecular i Nuclear de la Universitat de València per a optar al grau de Doctor en Física.

I per a que conste, en cumpliment de la legislació vigent, signem el present Certificat a Paterna a 18 de Setembre de 2006.

Signat: Juan José Hernández Rey

Signat: Juan Zúñiga Román

Vist i plau del tutora de Tercer Cicle:
D.Victoria Castillo Giménez

Als meus pares

# Agraïments

Primer de tot m'agradaria donar les gràcies a Juan Jose Hernández i Juan Zuñiga per haver-me donat la oportunitat d'entrar a formar part del grup ANTARES i per haver-me dirigit en la realització d'aquest treball d'investigació. Els seus consells, explicacions del detector i la física associada així com les seues correccions, han sigut d'ajuda inestimable i han fet possible la realització d'aquest treball.

També vull aprofitar aquestes línies per a agraïr al grup del Silici, en especial a Carmen Garcia i Joan Fuster, per haver-me donat la oportunitat de iniciar-me en el món de la investigació i poder coneixer així l'IFIC i els grups de Física que ací treballen.

També, com no, als meus companys físics dins del grup ANTARES: a Juanan per ser un molt bon company de despatx i de pis durant les estàncies en Marsella. També Juande i Emiliano durant el temps que coincidirem en el grup. A tots ells els done les gràcies per haver-me integrat rapidament en el grup i estar sempre disposats a discutir i aclarir-me qualsevol dubte sobre l'experiment.

També als enginyers del grup Diego i Victor, companys de viatge en les intregracions de Marsella. Ells han sabut explicar-me detalladament els dubtes sobre la part més tècnica del detector, tant important per a aquest treball d'investigació.

Apart dels membres del grup, també vull agraïr als meus compays físics dins i fora de l'IFIC: Ana, Arantxa, Carlos, Javi, Jose, Loli, Mercedes, Ximo, etc. pels bons moments viscuts durant i després de la carrera.

També als meus amics del poble per haver-me ajudat a desconectar de la feina i no haver perdut mai el contacte amb mi a pesar dels multiples viatges realitzats.

Finalment, donar les gràcies als meus pares i a la meua germana per haver-me recolzat en els moments difícils d'aquest complicat camí que és la vida. Esta clar que sense ells aquest treball no hauria vist la llum.

Per últim, agraïr a la resta de la gent que no he citat pero que també ha estat ahi, en major o menor mesura, ajudant-me. Gràcies a tots ells també.

# Contents

# Resum

## Introducció

Aquest treball d'investigació s'ha centrat en l'estudi de les balises òptiques del telescopi submarí de neutrins ANTARES. Aquest estudis han estat realitzats primer a València com a lloc on es produeixen les balises, i a Marsella com a lloc on se integren amb la resta del detector. Les balises òptiques han sigut dissenyades amb la finalitat de calibrar temporalment el detector. Aquesta calibració és necessaria pel tal d'aconseguir una resolució angular per a les traces de neutrins còsmics, millor que $0.3^o$. L'última part d'aquest treball està dedicada al repàs dels primers resultats obtinguts amb les balises submergides amb la línia d'instrumentacio (MILOM) des de la primavera de 2005. Aquest resultats han vingut a confirmar una resolució temporal de $\sim 0.4$ ns per als OMs, la qual proporciona la resolució angular prevista pel detector.

### Astronomia de neutrins

L'astronomia de neutrins és una nova forma de fer astronomia de recent aparició, on, a diferència de l'astronomia tradicional, no són els fotons sinó els neutrins els missatgers utilitzats per a l'estudi de l'univers.

Els neutrins són partícules fermiòniques de càrrega neutra i massa molt menuda, que apleguen a la superfície de la Terra provinents de l'espai junt a la resta de raigs còsmics, és a dir, partícules que no són fotons.

La primera evidència de l'existència d'aquestos raigs còsmics fou descoberta per V.Hess l'any 1912. A més, Hess va demostrar que el seu flux augmentava conforme anava pujant amb un globus aerostàtic, quedant així provat el seu origen extraterrestre.

Els estudis fets sobre l'espectre dels raigs còsmics mostra que aquestos apleguen a la Terra amb un flux que va com:

$$\frac{dN}{dE} \propto E^{-\gamma} \tag{1}$$

on $\gamma$ es l'anomenat índex espectral.

L'observació de neutrins en compte de fotons, té un clar avantatge quan es tracta de mirar objectes densos i llunyans. En aquest cas, els neutrins provinents d'aquest objectes, degut al seu caracter neutre, no interaccionen amb els camps magnètics, com fan per exemple els protons. També, degut a la seua baixa secció eficaç, els neutrins

interaccionen molt poc amb la matèria i poden per tant, travessar les denses superfícies, on es produeixen les reaccions mes energètiques, sense ser absorbits, cosa que no ocorre amb els fotons. Apart, tant els protons com els fotons d'alta energia interaccionen amb la radiació de fons, els protons amb la radiació de microones (efecte GZK) i els fotons amb el fons d'infrarrojos. Aquesta interacció fa que el seu recorregut lliure mig es veja reduït considerablement per a distàncies de l'ordre de 100 Mpc.

Entre les fonts de neutrins candidates, trobem els nuclis actius de galaxies (AGN) i les explosions de raigs gamma (GRB) com a candidats d'emissors extragalàctics. També microquasars, remanents de supernoves, el centre galàctic, sistemes binaris, etc. com a candidats de fonts galàctiques. L'emissió a altes energies d'algunes d'aquestes fonts ja han sigut confirmades pels moderns telescopis de raigs gamma, com és el cas de HESS o MAGIC.

Apart de la detecció d'aquestes fonts, ja comprovades experimentalment en raigs gamma, els telescopis de neutrins ens podem servir per a detectar o descartar altres possibles fonts de neutrins d'alta energia com ara els que prediuen els models "top-down", on els neutrins serien emessos en el decaïment de partícules molt massives. També s'han postulat altres teories on l'emissó de neutrins com a producte de defectes topològics, com monopols, cordes còsmiques, etc. A més a més, per a neutrins de més baixes energies, el telescopis de neutrins poden aportar alguna ajuda a l'estudi d'oscil.lacions observant un deficit en els neutrins atmosfèrics.

## ANTARES i els telescopis de neutrins

Pero tot no son avantatges amb els neutrins. De fet, el seu principal avantatge, és a dir, que interaccionen molt rarament degut a la seua baixa secció eficaç, és a la vegada el seu major inconvenient ja que eixa escassa interacció fa necessari grans volums de detecció. Es per açò que l'astronomia de neutrins necessita de grans aparells per tal de poder detectar un nombre significatiu d'events.

La idea de construir aquest tipus de detectors fou concebuda per primera vegada l'any 1960 per Markov. El principi de detecció està basat en recollir la llum Cherenkov que és emesa per un muó produït en una interacció prèvia d'un neutrí còsmic d'alta energia amb la matèria que envolta al detector. Per tal d'aconseguir açò, es construeix una xarxa de fotomultiplicadors (PMT) distribuïts dins d'un medi òpticament adecuat per a la propagació de la llum, com pot ser per exemple l'aigua o el gel.

Com hem vist, els volums de detecció han de ser grans, típicament de l'ordre del $km^3$, per a que el nombre d'events provinents de neutrins còsmics siga important. A més, s'ha de tindre en compte les possibles fonts d'events no desitjats com són els muons atmosfèrics, o be els muons produïts per neutrins atmosfèrics. Els primers estan altament suprimits gràcies a la profunditat a la que es coloquen els telescopis de neutrins, a més, els PMTs es solen colocar mirant cap avall, cosa que fa possible una reducció major dels muons atmosfèrics, si se consideren solament el events amb traça ascendent. Pel que fa als muons induïts per neutrins atmosfèrics, aquestos són més difícils de rebutjar, i la manera de distinguir-los dels neutrins còsmics està basada en

el diferent índex espectral que presenten ambdos.

La col.laboració ANTARES (Astronomy with a Neutrino Telescope and Abyss environmental RESearch), constituïda per 21 institucions de 6 països europeus, està actualment en plena fase de construcció d'un telescopi de neutrins en el fons del mar Mediterrani a 2500 metres de profunditat en front de la costa de Toulon (França). El detector estarà format per 900 fotomultiplicadors distribuïts en 12 línies d'uns 400 metres d'alçada formant una xarxa tridimensional, que s'encarregarà de detectar la llum Cherenkov. Aquestos PMTs estan ubicats dins d'una esfera que els protegeix de les altes pressions submarines, formant un conjunt anomenat Modul Òptic (OM). Els OMs estan orientats 45 graus cap avall per tal de reduir el fons de muons atmosfèrics, per tant, el telescopi de neutrins cobreix el cel oposat al que voria un telescopi tradicional de fotons en el mateix emplaçament.

Els principals elements del detector ANTARES són:

- El Mòdul Òptic (OM), és el element més important del detector, ja que alberga el fotomultiplicador (PMT) amb 10" de diametre de fotocatode. A més, també conté, entre altres, un LED intern per a calibrar el PMT.
- El Pis, constituït basicament per 3 OMs i un Mòdul de Control Local (LCM) on està l'electrònica de lectura del detector, on el principal component és la tarjeta ARS, que s'encarrega de processar la informacio de càrrega (AVC) i temps (TVC i TS) per als dos modes possibles de lectura de la senyal (SPE i WF) recollida en el PMT. A més, certs pisos poden estar equipats amb una Balisa LED o un hidrofón utilitzat per a la calibració espacial.
- Les 12 línies que constituixen el detector, amb 25 pisos cadascuna, ancorades en el fons del mar.
- El Cable Electro-Òptic, de uns 40 km de llargària que connecta l'estació de control en la costa amb el detector, s'encarrega de subministrar el potencial d'alimentació, la senyal de rellotge i la transmissió de dades, entre altres.

La col.laboració ha dedicat un llarg període de temps a la investigació i desenvolupament dels components finals per al detector, i ha fet també diverses campanyes marines en diferents parts del Mediterrani, per tal de trobar el lloc idoni per a ubicar el detector.

Actualment, el detector es troba en fase de producció. A més, 2 línies han sigut ja desplegades, una d'instrumentació (MILOM) i una del propi detector (Línia 1). El conjunt de les 12 línies s'espera que estiga submergit i operatiu cap a finals del 2007.

## El sistema de calibració temporal d'ANTARES i les balises òptiques

Tot telescopi de neutrins necessita d'una bona calibració temporal que permeta aconseguir una bona resolució temporal relativa ($\sim 0.5$ ns). Aquesta resolució temporal

relativa és important per tal d'obtenir una resolució angular òptima, que permeta apuntar el millor possible cap a les fonts de neutrins còsmics. També és necessària una bona resolució temporal absoluta ($\sim$ 1 ms) per a poder obtenir correlacions amb fenòmens físics d'interés, com per exemple explosions de raigs gamma, etc. Per tal d'aconseguir aquesta desitjada calibració, es duen a terme proves tant en el mar com en el laboratori. Aquestes proves són en alguns casos redundants. Les proves de calibració poden classificar-se depenent d'on es realitzen:

- Proves de calibració en el mar:

- Calibració amb el rellotge intern: Aquesta prova es realitza amb un sistema eco distribuït amb la senyal de rellotge. Açò dóna una senyal comú de referència a tots els LCMs. Amb aquest sistema, es pot coneixer el temps que tarda la senyal eco en fer tot el trajecte (anada i tornada). El temps que tarda en recorrer la meitat d'aquest trajecte s'anomena "fase del rellotge", la qual es calcula amb una precissió d'uns 100 ps.

- Calibració amb LEDs interns: Aquesta prova es du a terme amb el LED intern, el qual es troba apegat a la part de darrere del PMT dins del OM i és capaç de il.luminar-lo. Com el temps d'emissió de la llum del LED intern és conegut, es pot fer un seguiment del temps de transit del PMT.

- Les balises òptiques: Hi han dos tipus de balises òptiques, d'una banda està la Balisa LED. Aquesta consta d'un prisma hexagonal on cada cara conté 6 circuits pulsadors que contenen un LED cadascun d'ells. Aquest circuit permet la variació de la intensitat de llum emesa pels LEDs quan variem l'alimentació del circuit de 0V a 24V. L'activació d'aquest pulsadors es produeix en resposta al flanc de pujada d'una senyal cuadrada externa. Els LEDs emeten llum blava de 472 nm de longitud d'ona, i proporcionen en cada pols una energia de $\sim$ 158 nJ, treballant a màxima intensitat. La senyal que donen estan caracteritzades per tenir un ràpid flanc de pujada d'uns 2 ns. Una de les principals característiques de la Balisa LED, és que pot il.luminar els LEDs per grups (central, superior i 4 centrals) i per cares, separadament. A més, disposa de la possibilitat de ajustar la intensitat d'emissió dels mateixos. Tot açò dóna un ampli ventall de possibilitats a l'hora de configurar l'emissió de la balisa, lo qual es molt útil per a fer estudis de calibració. La lectura de la llum emesa pels LEDs es fa mitjançant un PMT emplaçat dins de la propia balisa, el qual proporciona el temps d'emissió de la llum.

  L'altra balisa òptica, la laser, està formada per un diode bombetjat de "Q-switched Nd-YAG" laser, construït per Nanolase el qual emet llum verda de 532 nm de longitud d'ona, i proporciona una energia per pols de $\sim$ 1 $\mu$J. A diferència de la balisa de LEDs, la seua emissió no és variable, i aquesta es fa a traves un difussor òptic que dóna una emissió lambertiana. L'enregistrament de la senyal del laser es fa utilitzant un fotodiode intern, el qual proporciona el temps d'emissió de la llum.

- Calibració amb muons atmosfèrics: Utilitzant el fons de muons atmosfèrics, es pot fer un seguiment dels desfasaments temporals ($\Delta$t) dels OMs. La idea es veure si amb els desfasaments temporals utilitzats en el ajustos, les traces dels muons reconstruïts són prou precises.

- Proves de calibració en el laboratori:

  Aquestes proves es realitzen utilitzant un sistema laser el qual proporciona una senyal comú, via fibra òptica, a un determinat nombre d'OMs. El temps d'emissió de la senyal del laser és registrat per un fotodiode intern que envia les dades a un LCM de referència. Aquest sistema permet la mesura dels parametres de calibració tals com:

- Desfasaments temporal entre OMs ($\Delta$t): Els desfasaments temporals relatius entre OMs es produeix degut a les diferencies en el temps de trànsit i la electrònica en cada OM. Els valors d'aquests desfasaments s'obtenen de la diferència temporal entre la senyal que ens dóna el LCM de referència i la que ens dóna el ARS del OM corresponent.

- Calibració del TVC: El TVC permet arrivar a una precissió, en la mesures temporals, de 50 ns. El que es preten amb aquesta calibració és calcular el rang real del TVC ($TVC_{min}$ i $TVC_{max}$). Açò és possibleja que l'emissió del laser es produeix amb una incertesa d'un centenar de nanosegons. Aquesta senyal donaria una distribució uniforme dins del rang de 50 ns que té el TVC.

- Calibració del llindar dels ARS: Aquesta prova es realitza utilitzant varies intensitats de la llum del laser, i ens permet, mitjançant un ajust, coneixer la equivalència entre les unitats del llindar del ARS i mV (p.e.), ja que es suposa una resposta lineal de l'AVC.

- Calibració de la càrrega: Els valors del pedestal (AVC_0) i el pic d'un fotoelectró (AVC_1) són calculats amb un tests similar a l'anterior, on s'utilitzen diferents intensitats del laser. Aquestos valors en permeten fer l'equivalència entre unitats de l'AVC i mV (p.e.).

# Objectius

Els objectius d'aquest treball han sigut, per una banda, establir un banc de proves per a comprovar que les balises òptiques funcionaven tal i com s'esperava del seu disseny en les fases de producció, integració amb la resta d'elements del detector, i ja amb la línia submergida. Per altra banda, l'altre objectiu ha sigut analitzar els resultats de calibració obtinguts amb les primeres dades en el mar de les balises òptiques.

## Proves de producció a València

Podem distinguir les proves atenent al tipus de balisa:

- balisa de LEDs

  La cadena de proves establida a València va estar basada en la funcionalitat i la sincronització de la emissió de llum pels LEDs. Provant la funcionalitat ens asegurem que podem canviar la intensitat de la llum emesa pels LEDs així com la ganancia del PMT xicotet que s'encarrega de enregistrar la senyal del LED per a saber el temps en el que ha sigut emés.

  Amb la sincronització ens asegurem que la emissió de tots els LEDs del beacons es fa en un interval menor a 0.3 ns, açò qual és important per a afectar el menys possible al temps de putjada de la senyal que recull el PMT de la balisa, ja que, açò esta directament correlacionat amb la resolució temporal que pot abastar el detector.

  També es va fer un estudi per Monte Carlo de com pot afectar aquesta desincronitzacio al temps de putjada de la senyal.

- Balisa Laser

  La Balisa Laser al igual que la balisa de LEDs ha estat provada funcionalment, com es mostra per exemple en l'estudi de l'estabilitat de l'emissió d'energia.

  Apart, al igual que passa amb la balisa de LEDs, el temps de pujada que recull el fotodiode intern encarregat de la lectura de la senyal és crucial per a abastar una bona resolució temporal. Per tant, es va fer un estudi de les fluctuacions aleatories que poden causar, durant l'enregistrament de la senyal, un empitjorament del temps medit.

## Proves d'integració a Marsella

En Marsella es dugueren a terme les proves de les primeres balises òptiques amb el disseny definitiu, per a la integració de la MILOM.

Una vegada amb les balises integrades en el sistema d'adquisió, es repetiren les proves de funcionalitat, i es mesuraren algunes propietats com el temps de pujada de la senyal, el soroll que s'indueix en montatge final, distribucions de AVC i TVC, taxa d'emissio de la balisa, etc. Amb aquestes mesures es comprovà que les balises funcionaven correctament.

Un estudi del temps de pujada de la senyal es va fer per a veure com canvia la resposta de les balises amb diferents muntatges experimentals

També es feren proves més especifiques per a la Balisa LED com il.luminar diferents grups i cares per separat.

### Proves amb les balises òptiques de la línia instrumental

La prova definitiva de les balises fou realitzada quan aquestes foren submergides amb la resta de la línia d'instrumentació la primavera de 2005. Amb la MILOM les primeres senyals de les balises òptiques foren presses, donant els primers resultats de calibració.

## Discussió dels resultats

### Tets de producció a València

En València les balises òptiques són muntades i provades avans de ser enviades al laboratori on es fa l'integració amb la resta d'elements del detector. Les banc de proves finalment ideat inclou:

- Balisa LED

- Muntatge i revisió visual de cadascun dels components de la Balisa LED.

- Comprovació de l'emissió de llum d'intensitat variable dels LEDs i correcta resposta del PMT intern.

- Mesura del rang d'emissió del LEDs individualment.

- Elecció d'un valor de sincronització comú a tots el LEDs i posterior sincronització d'aquestos.

- Comprovació de la correcta sincronització cara a cara amb la Balisa LED emplaçada dins d'una caixa negra.

- Prova tèrmica, on la Balisa LED es sotmesa a canvis de temperatura entre 10 i 40 graus.

- Revisió final dels components despres d'haver passat la prova tèrmica.

- Comprovació del nivell de soroll i sincronització abans de tancar la balisa en el seu contenidor.

- Tancament de la Balisa LED dins del seu contenidor i verificació final del funcionament i sincronització abans d'enviar la Balisa LED al lloc d'integració.

- Balisa Laser

- Estudi de la resposta temporal del fotodiode intern del laser. La qual, segons les dades obtingudes, proporciona mesures temporals amb una precissió de 50 ps.

- Estudi de l'estabilitat de l'energia emesa en cada pols del laser.

## Tets de integració

Les proves d'integracio i pre-integració de la MILOM i la Línia 1 foren realitzades al CPPM de Marsella. Allí s'obteniren les primeres senyals de les balises òptiques treballant amb el sistema d'adquisició d'ANTARES.

Per a la Balisa LED, les senyals preses en mode WF confirmaren la senyal vista amb l'oscil.loscopi a València. Les distribucions de càrrega mostraren que eren sensibles a canvis en la configuració (intensitat dels LEDs i/o ganància del PMT) de la Balisa LED tal com s'esperava. La distribució de TVC obtinguda resulta ser molt picada degut a la emissió sincronització i estable de la Balisa LED. El nivell de soroll va ser medit i s'estudiaren les possibles causes.

Les mesures fetes per a la integració de la MILOM, serviren per a establir les proves definitives que se faran a les balises òptiques de les futures 12 línies del detector abans de submergir-les. Les proves escollides foren finalment dos:

Primer s'il.luminà directament el PMT de la balisa de LEDs amb una senyal laser propagada mitjançant una fibra òptica. Amb aquesta prova es preten mesurar el parametre $\mathrm{TVC}_{min}$ i $\mathrm{TVC}_{max}$ del ARS destinat a la lectura del PMT de la balisa de LEDs. També es poden obtindre d'aquesta prova el valor del $\Delta$t del ARS de la balisa, al igual com es fa per a la calibració dels OMs.

En l'altra prova a realitzar, és la llum dels propis LEDs la que és recollida pel xicotet PMT. Aquesta prova ens serveix com a tests de la sincronització i funcionalitat de la balisa, així com una estimació del nivell de soroll. Aquest soroll s'haura d'eliminar "a posteriori" incrementant el valor del llindar per a l'ARS de la balisa.

Altres proves més especifiques foren fetes durant el llarg periode de pre-integració i integracio de la MILOM. Per exemple, l'estudi dels temps de pujada tant de tota la Balisa LED com de cada LED individualment, aixi com l'estudi detallat del soroll el qual va ser reduït notablement, o també l'estudi de la taxa d'emissió amb la qual il.lumina la Balisa LED.

Per a la Balisa Laser les proves realitzades en la integració de la MILOM mostraren valors de càrrega en saturació degut a la gran amplada de la senyal, i una distribució de TVC plana com s'esperava degut a la fluctuació en l'emissió dels polses del laser. La senyal en mode WF també fou obtesa, la qual va permetre la mesura del temps de pujada de la senyal.

Les senyal obtingudes per a les balises òptiques (laser i LED) una vegada integrades en el sistema d'adquisició, es podem vore a la Figura 1.

## Resultats amb les balises òptiques de la MILOM

Amb la MILOM a l'aigua es feren les primeres proves del sistema de calibració, il.luminat els OMs amb la llum emesa per les balises òptiques. Açò mostrà un bon accord entre les dades obteses en el laboratori i en el aigua, per als desfasaments temporals ($\Delta$t). La resolucio temporal individual dels OMs fou estimada en $\sim 0.4$ ns (Figura 2).

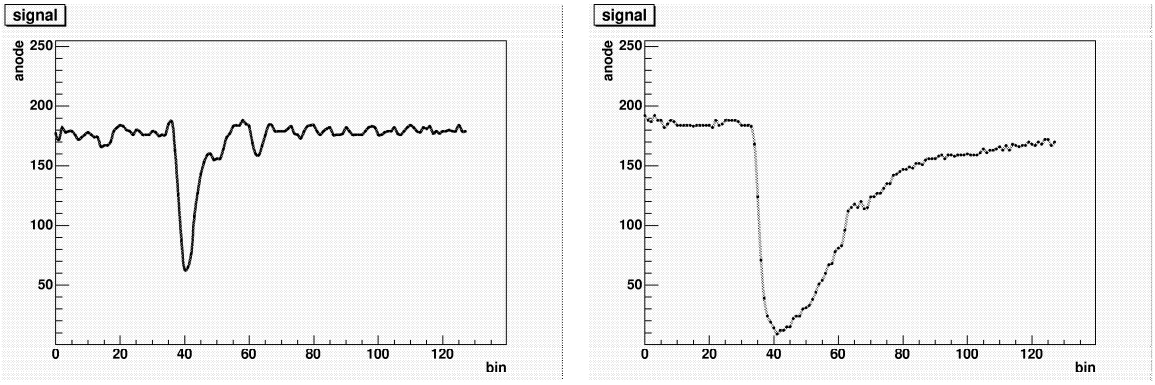


**Figure 1:** Dibuixos de les senyal obtesses per a la Balises LED (dreta) i per a la Balisa Laser (esquerra) una vegada integrades en el sistema d'adquisició.

Apart d'aquestes mesures i les necesaries de funcionalitat, també fou estimada la estabilitat d'emissió de la Balisa LED, estudiant les fluctuacions de les diferencies temporals Balisa LED-OM, aixi com la càrrega i temps recollits en l'ARS del PMT de la Balisa LED durant un periode de 45 dies.

# Conclusions

Els resultats més importants obtesos per a la part d'integració serien:

- En les balises de LEDs la sincronització feta en València proporciona una emissió simultània, cara a cara, dins d'un rang de temps menor que 0.3 ns. La qual, com s'ha mostrat per Monte Carlo, no s'espera que influisca el temps de pujada de la senyal i per tant, no s'espera que afecte a la resolució temporal.
- El nivell de soroll ha estat reduït des de les primeres probes que es fern amb les balises. Cal triar adecuadament el valor triat com a llindar, per a evitar aquestes senyals de soroll.
- Les mesures de carrega i temps fetes per a la balisa de LEDs amb el sistema d'adquisició, mostren un acord amb les mesures fetes a València tan per a tota la balisa il.luminant com per al cas en que sols un LED il.lumine.
- La Balisa Laser proveïx una senyal, d'energia estable, que pot ser mesurada amb el fotodiode intern amb una precisió temporal millor que 50 ps.
- Les mesures de càrrega i temps fetes per a la Balisa Laser amb el sistema d'adquisició, mostren un acord amb les mesures fetes a València.
- Totes les balises construïdes per a la MILOM, i la Línia 1 han mostrat un correcte funcionament.

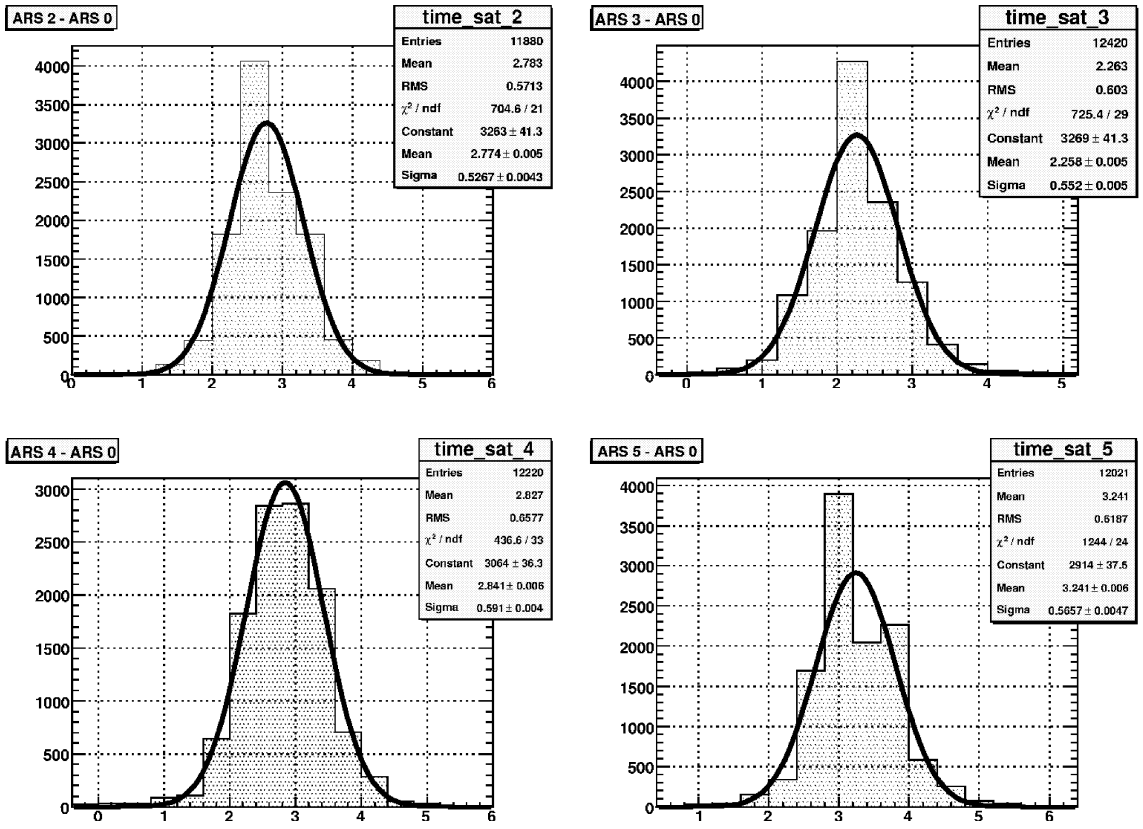


**Figure 2:** Figura amb les diferencies temporals entre OMs (ARSs) del mateix pis quan són iluminats per la Balisa LED. La resolucio temporal de cada OM individualment es $\sim 0.4$ ns.

El resultats més significatius obtinguts amb la MILOM són:

- Les primeres senyals del PMT intern (balisa de LEDs) i del fotodiode intern (Balisa Laser) foren enregistrades en el ARS de la balisa.
- Les distribucions de càrrega, temps i temps de pujada de les senyals de les balises eren similars en l'aigua i en el laboratori.
- Les distribucions de càrrega i temps mesurades per l'ARS dels OMs es veren modificades quan les balises il.luminaven.
- Les diferències temporals entre els OMs mostren un bon acord amb els paràmetres de calibració mesurats prèviament en el laboratori.
- La balisa de LEDs ha mostrat gran fiabilitat durant el seu primer any de funcionament, com s'ha vist dels estudis d'estabilitat.

- Les mesures fetes en la MILOM amb les balises òptiques, mostren una resolució temporal de $\sim 0.4$ ns per als OMs. Açò, junt a la precisió de $\sim 10$ cm que ens dóna el sistema acústic de posicionament, permet aconseguir una resolució de $< 0.3^o$ amb el detector ANTARES. Aquesta resolució ens permetrà, amb el detector completament desplegat, la detecció de fonts extraterrestres amb una precisió sense precedents en un telescopi de neutrins.

# Preface

Many advances has been made in the last decades in High Energy Physics. In particular, Neutrino Physics has been one of the fields with more development with the discovery of the neutrino oscillations by Kamiokande and the posterior confirmation by SNO. Neutrino Physics applied to astronomy is the aim of the ANTARES Neutrino Telescope.

The main motivation to construct a neutrino telescope comes from the studies of cosmic rays (non-photon particles) as a complement to photon studies in classical telescopes. These studies try to explain the origin of cosmic rays and the acceleration mechanisms that take place on astrophysical objects as radio galaxies, active galactic nuclei (AGN), gamma-ray bursts (GRB),etc. Cosmic rays also can provide a hint about one of the most interesting mysteries of astrophysics, dark matter. Calculations about the rate of capture of WIMP particles in big bodies (the Sun, the Earth, ...) and the neutrino spectrum produced in their annihilations can be tested. Neutrino oscillations might be also studied in neutrino telescopes.

The use of neutrinos has several advantages in the study of very far away cosmic sources comparing with traditional photon astronomy. Neutrinos are electrically neutral, so they are not deflected by magnetic fields. Due to their low cross-section, they can reach us from very far away sources and we can "see inside" of the estellar objects, where photons are not able to pass through their dense opaque regions. In addition, high energy photons interact with the CMBR producing $e^+e^-$ pairs so photons with energy greater than 10 TeV are not expected to reach us if they are produced at distances of the order of 100 Mpc. Neutrinos are also stable particles and do not decay as free neutrons do. In conclusion, Neutrino Telescopes detecting TeV (or greater) cosmic neutrinos are a challenging way to improve our knowledge of the extraterrestrial objects.

However, not all are advantages. Their low cross-section entails a big problem to detect them. The experiments devised to work as neutrino telescopes use a huge volume of matter to enhance neutrino interaction. For the time being, ice or water seems to be the best environment.

The ANTARES collaboration, integrated by scientists and engineers from France, Germany, Italy, the Netherlands, Russia and Spain is constructing a neutrino telescope in the Mediterranean sea. The principle of detection is based on the Cherenkov light induced by the charged particles produced in a neutrino interaction with the surrounding matter. The detector is a 3D array and consists of 12 strings with 900 photomultipliers

distributed on triplets along the lines. It is located at 2500 m depth under the sea on the coast close to Toulon (France).

Great advances were made in the spring of 2005 with the deployment of the Line 0 (mechanical test line) and the MILOM (Mini Instrumentation Line with Optical Modules), but the major step was done very recently in March 2006 with the achievement of the Line 1 connection, the first complete line of the ANTARES neutrino telescope. These successes, together with the experience of other neutrino telescopes like BAIKAL and AMANDA, give good expectations to do neutrino astronomy in the near future.

The aim of this research work is the analysis of the data obtained in the tests performed with the Optical Beacon system for the MILOM and the Line 1, before and after to be deployed in the sea. The Optical Beacon system is one of the ANTARES calibration systems, which is crucial in order to achieve a good relative timing resolution. The pointing accurancy of the detector depens critically of this relative timing resolution.

This research work is composed by the following structure. In Chapter 1 a brief overview of cosmic rays and neutrino astronomy is given. A description of the ANTARES telescope and his current status is presented in Chapter 2. Chapter 3 is devoted completely to the time calibration systems implemented in the ANTARES detector, making special emphasis on the Optical Beacon calibration system. The results of the integration of the Optical Beacons for the MILOM line and the Line 1 are summarized in Chapter 4, and finally, in Chapter 5 data analysis from the MILOM line showing results on time calibration with the Optical Beacons system are presented.

# Chapter 1

# High-energy Neutrino Astronomy

Neutrino astronomy is a very recent and promising field of research. The main motivations to do neutrino astronomy are related to the still open questions about the origin of cosmic rays and the nature of dark matter. In this chapter, an overview on cosmic rays will be given, in particular we will focus on the neutrino case and how neutrino astronomy can help us to solve these unclear questions.

## 1.1 Cosmic rays

Cosmic rays were discovered by V. Hess in 1912 [1] when he observed that the flux of this unknown radiation increased as he ascended in a balloon flight. This was in disagreemnet with the current idea believed at the moment of being emitted by the Earth's crust, and demonstrated its extraterrestrial origin.

Cosmic rays are non-photon particles like protons, pions, neutrinos, etc. They fall continuously over us isotropically. We can distinguish between primary cosmic rays and secondary cosmic rays. Primary cosmic rays are basically protons (89%), but we can find also helium (10%) and heavier nuclei (1%) [2]. Secondary cosmic rays are the products of protons (mainly) colliding with nitrogen and oxigen nuclei in the atmosphere. These products can collide again or decay into new particles that give rise to atmospheric cascades through pair production, bremsstrahlung, and other reactions producing muons, electrons, photons and neutrinos to a large extent.

Almost all these secondary particles are absorbed by the atmosphere, which shields the Earth by roughly 20 radiation lengths. However, muons (due to the relativistic time expansion) and neutrinos (due to their low cross-section), can reach the Earth's surface with an important flux.

Cosmic rays have a very wide energy spectrum which follows a power law as it is showed in the Figure 1.1.

$$\frac{dN}{dE} \propto E^{-\gamma} \tag{1.1}$$

where $\gamma$ is the so-called spectral index.

This picture covers over ten decades on energy and thirty decades on flux. In this spectrum we can distinguish three important points: the knee, which is around $\sim 10^{16}$ eV, the ankle at $\sim 3 \times 10^{18}$ eV and the Greisen-Zatsepin-Kuzmin (GZK) cut-off [3] at $\sim 6 \times 10^{19}$ eV. The knee and the ankle represent slope changes in the cosmic ray energy spectrum, i.e., the spectral index is 2.7 before the knee, then changes to $\sim$ 3.0 up to the ankle, and after the ankle it goes to $\sim$ 2.7 again.

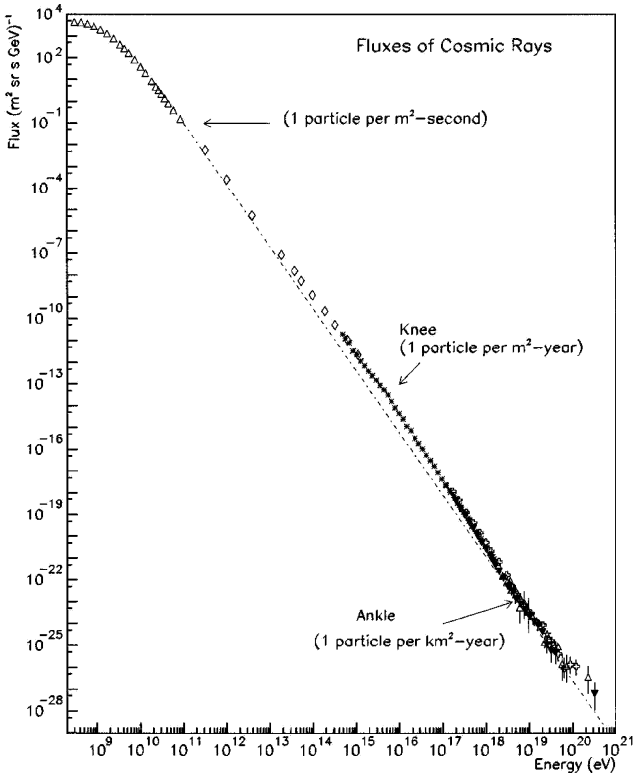


**Figure 1.1:** The cosmic ray energy spectrum plot covering 12 decades in energy. The knee and the ankle points can be seen in the picture.

### 1.1.1 Cosmic rays origin

A mechanism to explain the acceleration of the charged cosmic rays (neutral particles as neutrinos or photons appear as decays of charged particles) is the diffusive shock acceleration mechanism, which fits good with the energy spectrum law seen in the Figure 1.1. The main idea for stochastic particle acceleration is the transfer of macroscopic kinetic energy from moving magnetized plasma to individual charged particles. Assuming that after each encounter with the magnetic plasma, the particle's

kinetic energy increases by $\Delta E = \xi E$, the number of particles with energy above a given value $E$ (the integral energyso spectrum) is given by:

$$N(>E) \propto \frac{1}{P_{esc}} \left( \frac{E}{E_0} \right)^{-\gamma}$$

where $E_0$ is the particle's initial energy, $P_{esc}$ is the probability of escaping from the acceleration region and $\gamma$ is given by:

$$\gamma = \ln \left( \frac{1}{1 - P_{esc}} \right) / \ln(1 + \xi)$$

We will mention under this context the 2nd order Fermi acceleration mechanism, which was the original theory proposed by Fermi in 1949 [4]; and the 1st order Fermi acceleration mechanism, where the previous theory is modified into a more efficient mechanism.

**Second order Fermi acceleration mechanism**

In the 2nd order Fermi acceleration mechanism an ultra-relativistic cosmic ray with energy $E_1$ and momentum $p_1$, enters a cloud with angle $\theta_1$ with the cloud's direction. It is also assumed that the cosmic ray suffers elastic scattering with the magnetic irregularities of the gas cloud, so that there is no energy change on the cloud frame ($E'_1 = E'_2$). These clouds have typically random velocities of ∼15 km/s superimposed on their regular motion around the galaxy. After scattering inside the cloud, the particle emerges with energy $E_2$, momentum $p_2$, and an angle of $\theta_2$ (Figure 1.2 left side). A Lorentz transformation between the laboratory frame (unprimed) and the cloud frame (primed), provides an energy change given by:

$$\frac{\Delta E}{E} = \frac{1 - \beta cos\theta_1 + cos\theta'_2 - \beta^2 cos\theta_1 cos\theta'_2}{1 - \beta^2} - 1 \tag{1.2}$$

where $\Delta E$ has been computed as $\frac{(E_2 - E_1)}{E_1}$, and the energies in both frames are related to each other by:

$$E'_1 = \gamma E_1 (1 - \beta \cos\theta) \; ; \; \mathrm{E}_2 = \gamma \mathrm{E}'_2 (1 + \beta \cos\theta'_2)$$

being $\beta = V/c$ with $V$ the cloud velocity.

When averaging over many encounters, $\langle \cos\theta'_2 \rangle = 0$, since the particle direction is randomized inside the cloud due to many collisions. The average value of $\langle \cos\theta_1 \rangle$ depends on the rate at which cosmic rays collide with clouds at different angles, which is proportional to the relative velocity between the cloud and the particle. With these conditions, the average growth in energy using Equation 1.2 , is given by:

$$\frac{\langle \Delta E \rangle}{E} \simeq \frac{4}{3} \beta^2$$

Because of the quadratic dependence on $\beta$, this method is called the 2nd order Fermi acceleration mechanism. Since $\beta \ll 1$[1], the average energy gain per collision with the cloud, is very small.

### First order Fermi acceleration mechanism

In this model a supernovae non-relativistic shock is considered but is applicable to any astrophysical object able to produce strong shock-waves. During a supernovae explosion several solar masses of material are ejected at a speed of $\sim 10^4$ km/s, that is faster than the sound speed in the ISM which is $\sim$10 km/s. A strong shock wave is so that produced with speed $V_s$. The particles are now accelerated when crossing the shock (Figure 1.2 right side). In this new scheme, $\langle \cos\theta_1 \rangle \approx$ -2/3 and $\langle \cos\theta'_2 \rangle \approx$ 2/3 [5], and now the average energy given by Equation 1.2 is:

$$\frac{\langle \Delta E \rangle}{E} \simeq \frac{4}{3}\beta \qquad \text{with} \qquad \beta = \frac{V_p}{c}$$

where $V_p$ is the supernovae ejection speed. In this case the dependence on $\beta$ is lineal (1st order mechanism), so the energy change per collision is higher than in the 2nd order mechanism model.

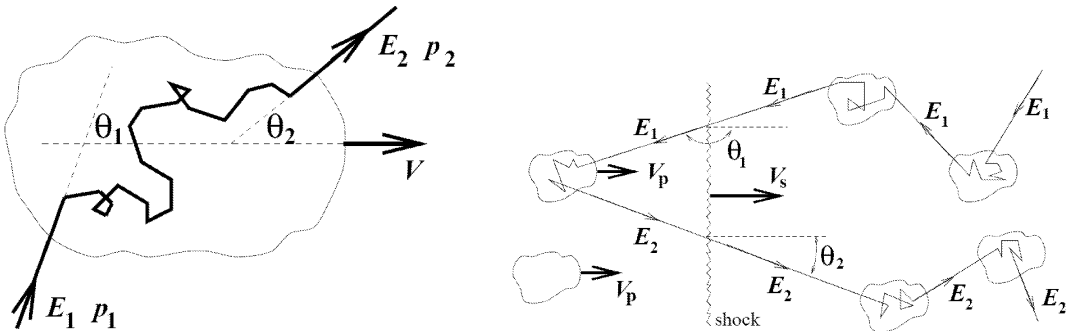


**Figure 1.2:** Schematic view of the 2nd (left side) and 1st (right side) Fermi acceleration mechanisms where the incoming and the outgoing cosmic ray are represented.

There is a general agreement that the main contribution to the cosmic ray energy spectrum below the knee is caused by supernova remnants (SNR) following the Fermi acceleration mechanism. In this frame the maximum energy reachable, for the most favourable scheme of supernova expansion, is $\sim$100 TeV [6]. So the knee appears as an energy acceleration limit of these SNR sources. However, as we saw in the Figure 1.1, energies beyond the knee are possible. Cosmic ray origin in the region between the knee and the ankle is not so clear, and several explanations have been proposed. In [7], Bednarek and Protheroe consider the galactic population of gamma-ray pulsars

[1] $\beta = \frac{V}{c} \simeq \frac{15\text{km/s}}{3\times10^5\text{km/s}} \ll 1$

as possible sources. Biermann proposes Supernova shocks that travel down the density gradient of stellar wind [8]. Supernovae explosions coming from very massive and hot stars have also been proposed as responsibles of the production of cosmic rays with energies above the knee [9]. These explosions give an irregular spectrum but this irregularity can be reduced with the existence of a Giant Galactic Halo.

Concerning the ankle, is well accepted that it is an evidence of the transition from galactic to extragalactic origin. The energy spectrum beyond the ankle can be seen as the sum of two components. One galactic, which falls with energy because of the lack of sufficiently energetic sources and enough magnetic trapping to retain the cosmic ray flux, and another extragalactic, which follows a power law due to the Fermi acceleration mechanism until the GZK cut-off.

According to the GZK cut-off, protons above the threshold energy of $10^{20}$ eV interact with the 2.7 K cosmic microwave background radiation (CMBR) and lose their energy via photo-pion production:

$$p + \gamma_{CMB} \longrightarrow \pi^0 + p \quad \text{or} \quad \pi^+ + \text{n}$$

The mean free path of these particles is reduced by more than two orders of magnitude, therefore, the cosmic rays expected from more than 100 Mpc far away sources are essentially zero. Events above the GZK cut-off has been observed by telescope array experiments like AGASA, HiRes and the still in development AUGER. However, only AGASA has detected higher fluxes than what is expected from the GZK cut-off.

Some theories have been developed to explain the origin of the very high energetic events. "New physics" models are commonly postulated. For instance, they can be seen as the products of topological defects [10] or decaying superheavy relic particles [11] which have to be close to us in cosmological distance terms. Another hypothesis are focussed on finding a way to evade the GZK effect, or directly to state its non existence [12] but, in any case, there is still a lot of open questions about the origin of this kind of events. It seems like we have to wait until the final Pierre Auger Observatory deployment with 3000 km$^2$ where around 450 events/year are expected. Neutrino telescopes can contribute with some clues to solve this puzzled question.

## 1.2 High energy photon astronomy

Photon astronomy has been done traditionally using visible light of the electromagnetic spectrum. However, in order to go deeply into the Universe phenomenons, astronomy has required to explore all the wavelengths. In our particular case, we will focus on the high energy photons. Two mechanisms are possible to understand the acceleration of neutral particles. In the "leptonic models", photons appear in positron and electron acceleration by synchrotron radiation, bremsstrahlung and inverse Compton scattering. In this frame no neutrinos are predicted. On the other hand, in the "hadronic models", neutrinos and photons are predicted via meson decays. There are

two types of processes that lead to the production of these mesons and, therefore, neutrinos in the hadronic models: inelastic hadronic interaction ($pp$) and photoproduction interactions on photon fields ($p\gamma$). In principle, both models (leptonic and hadronic) can live together. In any case, high energy photon sources are serious candidates to be also high energy neutrino emitters. Neutrino telescopes will provide cross-checks of the sources already confirmed by the high-energy gamma-ray detectors.

Many experiments have been devised to explore these high-energy photon sources. Depending on the detection energy range we can distinguish between spatial-satellite and ground-based detectors. The satellite instruments operate at MeV-GeV energies and can detect directly the incident photon. The Figure 1.3 shows the third Energetic $\gamma$-ray Telescope (EGRET) Catalog [13], which contains 271 sources being around 170 still unidentified due to poor angular resolution. This task will be followed by future spatial experiments like GLAST and Agile.

When we try to detect more energetic $\gamma$-rays ($> 100$ GeV), the spatial detectors are not large enough to detect them and the flux is extremely low. The best way to detect higher energy $\gamma$-rays is to use Imaging Air Cherenkov Telescopes (IACT) which are designed to detect the Cherenkov light emitted in the cascades produced by high-energy photon interactions with the atmosphere. Amazing results were achieved with the pioneering telescopes Whipple and HEGRA in the nineties. Currently, a new generation of IACT telescopes as MAGIC, HESS, VERITAS, etc. is providing many interesting results about the acceleration mechanisms in the high energy gamma-ray sources. For instance, the HESS IACT located at Namibia, has detected a set of about thirty sources above 100 GeV, as AGNs Markarian 421 and 501, Galactic Centre and Crab pulsar. Some of the sources detected by HESS have also been confirmed by Whipple and MAGIC.

With this new detection technique, high-energy $\gamma$-rays have been detected from very far away sources (900 Mpc) [14]. Hypothetical neutrinos coming from these sources will provide more information about the origin of the high energy photons and the models previously commented.

## 1.3 The case of neutrino

The neutrino hypothesis, proposed by Pauli in 1930, was the only way to save the energy and angular momentum conservation in the $\beta$-decay. It was supposed that there was a neutral particle with small mass emitted simultaneously with the electron. In fact, it was originally named "neutron", but this neutral particle was discovered in 1932 by Chadwick. The main problem with the neutrino was its difficult detection. They can penetrate several light years depth of ordinary matter before they would be stopped. Due to this fact, we had to wait more than 20 years for the detection of the first neutrino (in fact anti-neutrino) in the inverse beta decay reaction by Cowan and Reines.

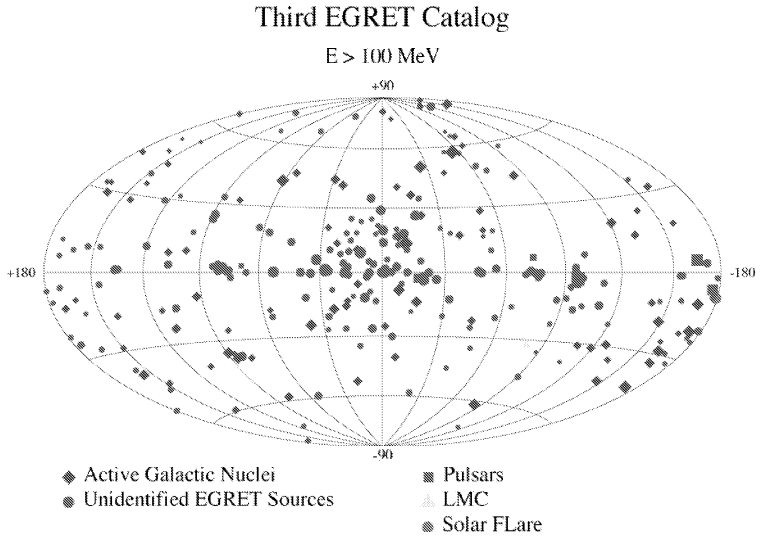


**Figure 1.3:** Third EGRET catalog with detected $\gamma$-ray sources of E > 100 MeV. The size of the symbol represents the highest intensity seen for this source by EGRET.

$$\bar{\nu_e} + p \longrightarrow e^+ + n$$

The first neutrino detection took place in the Hanford nuclear reactor (1953) with a very high background rate, mainly due to reactor neutrons and $\gamma$-rays. After that, it was detected with better shielding in Savannah River Plant (1955). They used as target water with cadmium chloride dissolved. The expected signal was a sequence of two consecutives light flashes separated by few microseconds, one flash coming from the positron annihilation and the other one coming from $\gamma$ radiation of Cd* after neutron capture. They were able to observe a signal 5 times greater when the reactor was on than off.

## 1.4 Neutrino sources

There are a lot of neutrino sources that can be classified according to their energies and/or origin (see Figure 1.4). Among them, we will concentrate on high-energy neutrino sources which are foreseen to be detected in neutrino telescopes. We will not mention neutrinos from artificial sources like reactor or accelerator neutrinos which are conceived to specific physics goals. We will start with a brief review on solar neutrinos and will follow with an overview on atmospherical and astrophysical neutrinos. Finally, other exotic sources will be mentioned.

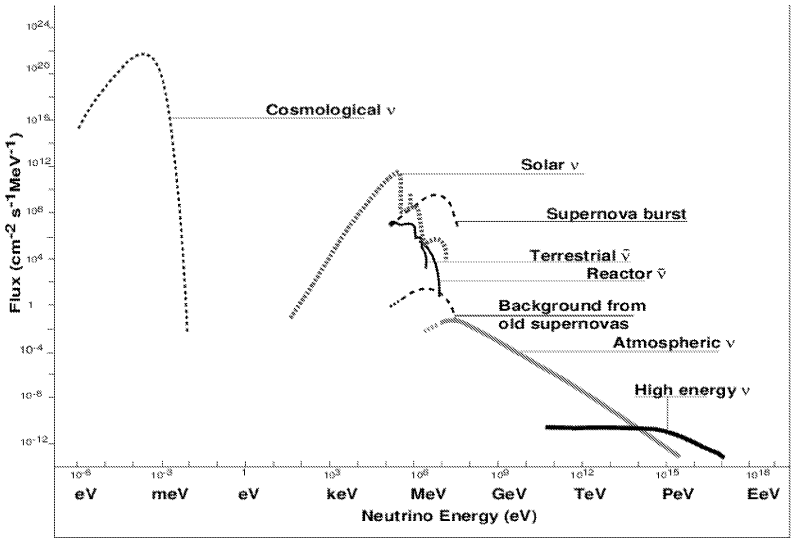


**Figure 1.4:** Indicative neutrino fluxes from astrophysical and terrestrial sources.

### 1.4.1 Solar neutrinos

The Sun has been the most studied neutrino source due to the fact that is the closest radiating neutrino object. Another important reason to study the Sun is the unavoidable link with neutrino oscillations, which are reflected in a solar neutrino flux deficit.

The standar solar model provides precise estimations about how these neutrinos appear. Produced in the hidrogen fussion cycle, they cover an energy range from 0.1 to 20 MeV [15]. As we can see in the Figure 1.5, the higher neutrino flux ($\sim 6{\times}10^{10}$ $s^{-1}cm^{-2}$ ) comes from the *pp* reaction:

$$p + \bar{p} \longrightarrow d + e^{+} + \nu_e \qquad \text{with} \quad E \leq 0.423 \text{ MeV}$$

However, higher energy reactions are preferable in order to detect them, even though the fluxes are reduced by several orders of magnitude:

$$^{8}B \longrightarrow ^{8} Be^{*} + e^{+} + \nu_e \qquad \text{with} \quad E < 15 \text{ MeV}$$

or

$$^{3}He + p \longrightarrow ^{4} He^{*} + e^{+} + \nu_e \qquad \text{with} \quad E < 18.8 \text{ MeV}$$

### 1.4.2 Atmospheric neutrinos

Atmospheric neutrinos appear as secondary particles in hadronic showers after collisions of primary cosmic protons (mostly) with nuclei in the atmosphere. In these

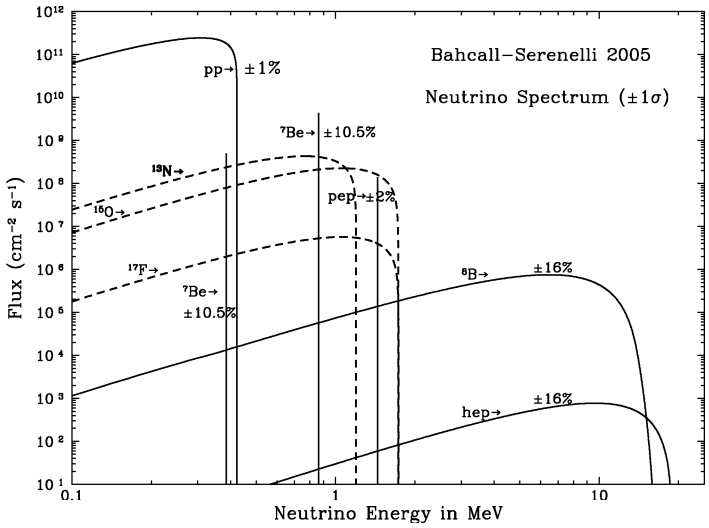


**Figure 1.5:** Neutrino flux versus neutrino energy for different reactions in the sun.

hadronic showers, charged mesons decay into $\mu$ and $\nu_\mu$, and subsequently muons decay and give $\nu_\mu$ and $\nu_e$, so that there is an expected average of 2 muon-neutrinos for each electronic-neutrino.

$$\begin{aligned} p, n \longrightarrow \pi^{\pm}(K^{\pm}\dots) &\longrightarrow \mu^{\pm} + \nu_\mu(\bar{\nu_\mu}) \\ &\downarrow \\ &e^{\pm} + \bar{\nu_\mu}(\nu_\mu) + \bar{\nu_e}(\nu_e) \end{aligned}$$

The atmospheric neutrino energies extend from a few MeVs to the energies of the most energetic cosmic rays. The differential flux for $E_\nu \gg 1$ GeV, for $\nu_\mu + \bar{\nu_\mu}$ coming from meson decay can be written as:

$$\frac{dN_\nu(E_\nu,\theta)}{dE_\nu} = \frac{\phi_N(E_\nu)}{(1-Z_{NN})(\gamma+1)} \left\{ \left[ \frac{Z_{N\pi}(1-r_\pi)^\gamma}{1+B_{\pi\nu} cos\theta E_\nu/\epsilon_\pi} \right] + 0.635 \left[ \frac{Z_{NK}(1-r_K)^\gamma}{1+B_{K\nu} cos\theta E_\nu/\epsilon_K} \right] \right\}$$

where $r_i = m_\mu^2/m_i^2$ for $i = (\pi,K)$, and the constants $B_i$ depend on hadron attenuation lengths as well as decay kinematics. The $Z$ values contain the physics of production of the parent pions and kaons. The values for these constants can be found in [16].

The atmospheric neutrinos represent a background signal for neutrino telescopes. These neutrinos, due to the density of the atmosphere, show an energy spectrum which falls with a spectral index of $\gamma \sim 3.7$, which is greater than the $\sim 2.2$ expected from the neutrinos produced in cosmic accelerators.

### 1.4.3 Astrophysical neutrinos

Astrophysical neutrinos are the most interesting kind of neutrinos to be detected in a neutrino telescope. Neutrino sources are still hypothetical but, the increasing number of gamma-ray sources that have been detected by IACT experiments in the recent years, makes very probable the existence of a neutrino counterpart. They are supposed to be produced in galactic and extragalactic objects simultaneously with other high energy cosmic rays, so energies from 1 TeV ($10^{12}$ eV) to $10^{21}$ eV, following distributions similar to primary cosmic rays are expected (see Figure 1.1). According to their provenance, they can be classified as galactic or extragalactic sources:

#### Galactic neutrinos

There are a lot of galactic objects that, being less powerful than the extragalatic sources, represent promising candidates for neutrino sources. Among them, it is worth mentioning: supernovae, binary systems, microquasars and the Galactic Centre.

- **Supernovae:**

  Supernovae are the products of star explosions after their death. These explosions are relatively rare events in our own galaxy and they happen once a century in average. They are very energetic and emit big amounts of energy in form of gamma rays and neutrinos. However, these neutrinos are not enough energetic (typically E $\sim$ 10 MeV) to be detected by neutrino telescopes. Nevertheless, high-energy neutrinos can be produced during the relatively short period after the explosion. Depending on its mass, a supernova can create a neutron star, a pulsar, a binary system, etc. or even a black hole if its mass is greater than 3 $M_{\odot}$. The remains of exploded stars are called supernova remnants (SNR). They are made of hot gases that have been hurtled into space by the force of the supernova explosion. These remnants can be thousands of years old and many hundreds of light years wide. All these components provide different scenarios for particle acceleration. Supernovae coming from massive stars (Type II supernovae) can create shock waves that are able to accelerate protons above 10 TeV. Some models predict [17] up to 100 events in a $km^2$ detector coming from a $\sim$10 kpc far away supernova source.

  Gamma rays with energies above $\sim$1 TeV have been observed from spherical supernova remnants such as SN1006, Cas A and SNR RX J1713.7-3946. Recently, the HESS collaboration has reported a TeV $\gamma$-ray image of the SNR RX J1713.7-3946 [18], placed on the Galactic plane, in the Scorpius constellation. This SNR is hitting a molecular cloud of density higher than 100 $cm^{-3}$, and gamma-rays up to energies of 10 TeV has been observed. This requires an extremely effective accelerator boosting particles up to energies of at least 100 TeV. In this frame, TeV emission can originate from different processes. In particular, neutral pion decays after *pp* interaction can contribute significantly on the high density regions. A flux of neutrinos from charged pions should be also produced in this case.

More different scenarios to accelerate particles are possible. For instance, the pulsar wind nebulae or Plerions. In this case, the radio, optical and X-ray emission observed is likely due to synchroton emission (Figure 1.6). The most important example of Plerion is the Crab nebula in the Taurus constellation, which is the result of a supernova explosion in 1054. It contains a rapid pulsar inside which rotates with a 33 milliseconds period and a spin-down luminosity of $5 \times 10^{38}$ erg $s^{-1}$. Crab nebula emits in a wide electromagnetic spectrum up to TeV gamma-rays, as it has been showed by HESS [19] and MAGIC [20]. For this kind of young nebulae, assuming *pp* collisions, from 1 to 12 events are expected in a $km^2$ neutrino detector in the energy range $E_\nu \sim$ 1-100 TeV [21].

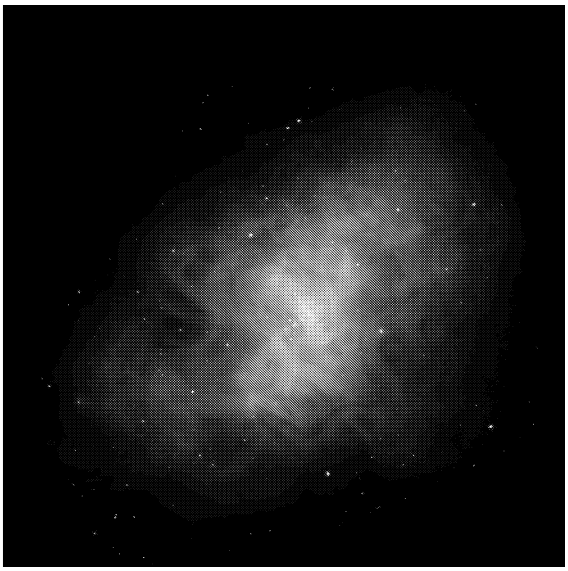

**Figure 1.6:** A composite image of the Crab Nebula showing X-ray in blue, optical in green, and radio in red.

Another special case are neutron stars whose magnetic field is so huge ($\sim 10^{15}$ G) that radically alter the material within them. These objects are called magnetars. In this scenario, magnetic stresses are slowly building up. At some point the solid crust is strained beyond its limit and it fractures. This "starquake" creates a surging electric current which decays and leaves behind a hot fireball. The fireball cools by releasing X-rays from its surface. It evaporates in minutes or less [22]. These objects are repeating flashes of soft (low energy) gamma-rays (SGR), and have been proposed as TeV neutrino sources through photomeson interactions [23].

- **Binary systems:**

  Binary systems are two stelar objects orbiting around a common center of mass. The most powerful case is when one of them is a collapsed object such as a white

dwarf, a neutron star, or a black hole. The separation between the stars is small enough so that matter is transferred from the normal star to the compact object through an accretion disk. These objects mainly emits X-ray in the process (X-ray binaries). Neutron stars are known to have very strong surface magnetic fields ($10^{12}$ G) and sometimes millisecond periods. Both, the accretion and the magnetic dipole radiation are possible energy sources. The existence of high magnetic fields and plasma flows creates the environment necessary for the formation of strong shocks, and the corresponding particle acceleration. Calculations of the neutrino flux expected from Cygnus X-3 give a total upward going muon events between 50 and 100 per year for a 0.1 km$^2$ fully efficient detector [24].

- **Microquasars:**

  These objects have the same nature than the AGNs (see section 1.4.3). The main difference is that they are less powerful, but closer to us. These systems consist of a compact object (a neutron star or a black hole) and a companion star. In principle, they are like binary systems but with the characteristic of having radio jets. The compact object accretes matter from the companion star with resulting ejection of plasma into the jets. The neutrino production in these objects should follow the behaviour of AGNs that will be showed in the next section. Esentially, if hadronic processes are present, neutrinos should be emitted from microquasars.

  The expected number of events coming from microquasars depends on the source properties as distance, angle of sight, luminosity, etc. The flux values expected for >1 TeV neutrinos are showed in the Figure 1.7 left [25]. A plot with the convolution between the predictions and the ANTARES effective area is showed in the Figure 1.7 right [26]. The largest expected fluxes are from the persistent sources SS433 and GX339-4.

- **Galactic Centre:**

  Placed in the Sagittarius constellation, the Galactic Centre is the most interesting hypothetical source of neutrinos in the galaxy. There, we can find hundreds of white dwarf stars, neutron stars, and a supermassive black hole in the centre. All these potential sources have been already confirmed in gamma-ray emission by EGRET in the GeV range, and more recently by the HESS collaboration for TeV scale [27]. The Galactic Centre especially has a great interest for ANTARES telescope since its location allows it to be observed.

### Extragalactic neutrinos

Extragalactic objects are the most energetic sources in the Universe. We will mention AGNs and GRBs which are nowadays confirmed emitters of energetic gamma-rays and potential neutrino sources. Neutrinos have the advantage of being the only particles which could escape from the dense core of these sources (black hole typically). Photons are not able to scape because of the very high optical depth inside.

TABLE 2
>1 TeV NEUTRINO FLUX AT EARTH FROM IDENTIFIED GALACTIC MICROQUASARS

| Source Name | $f_{\pi,\mathrm{peak}}$ | $\eta_{p,-1}^{-1}\eta_{e,-1}^{1/2} f_\nu$ (ergs cm$^{-2}$ s$^{-1}$) |
|---|---|---|
| Cl Cam | 0.07 | $2.23 \times 10^{-10}$ |
| XTE J1748−288 | 0.20 | $3.07 \times 10^{-10}$ |
| Cyg X-3 | 0.12 | $4.02 \times 10^{-9}$ |
| LS 5039 | 0.02 | $1.69 \times 10^{-12}$ |
| GRO J1655−40 | 0.19 | $7.37 \times 10^{-10}$ |
| GRS 1915+105 | 0.24 | $2.10 \times 10^{-10}$ |
| Cir X-1 | 0.27 | $1.22 \times 10^{-10}$ |
| LS I 61°303 | 0.03 | $4.49 \times 10^{-11}$ |
| LS I 61°303 | 0.02 | $9.06 \times 10^{-12}$ |
| XTE J1550−564 | 0.04 | $2.00 \times 10^{-11}$ |
| V4641 Sgr | 0.02 | $2.25 \times 10^{-10}$ |
| V4641 Sgr | 0.002 | $3.25 \times 10^{-8}$ |
| Sco X-1 | 0.01 | $6.48 \times 10^{-12}$ |
| SS 433 | 0.29 | $1.72 \times 10^{-9}$ |

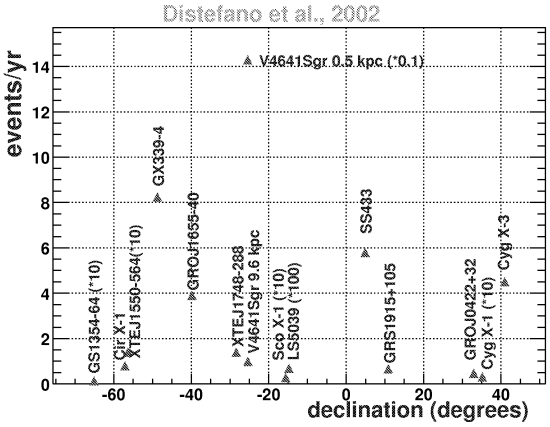


**Figure 1.7:** Expected flux for some galactic microquasars (left side). Event rates in the ANTARES detector for some microquasars assuming hadronic origin (right side).

- **Active Galactic Nuclei:** Basically, the AGNs are galaxies where enormous amounts of energy are emitted. The accepted AGN standard model consists of an internal supermassive black hole ($10^6$ - $10^{10}$ $M_\odot$) with an accretion disk, where dust and gas are accumulated. The black hole accretes matter and produces the jet emission from their centre. There are several types of AGNs according to their emission properties, like luminosity or main wavelength emission (Seyfert Galaxies, Quasars, LINERs, Blazars, etc.). However, it is thought that all of them are the same phenomenon seen from different relative angles and in different ages (see Figure 1.8 right). A huge emission is produced in X-rays and $\gamma$-rays as has been confirmed by EGRET. Apart from photons, neutrinos are also expected to be produced if the acceleration mechanism is based on hadronic models. In [28] G.C.Hill presents some models for the expected flux. Typically, the number of muon events per year in a detector with an effective collecting area of $2 \times 10^4$ m$^2$(0.02 km$^2$) would be according to Stecker et.al [29]: ∼60 events above 1 TeV, and ∼40 above 10 TeV. However, according to Protheroe model [30] ∼10 events above 1 TeV, and ∼6 above 10 TeV are expected. This should be compared with an atmospheric neutrino background of 225 (1 TeV) and 5 (10 TeV) per year.

  However, because of the last AMANDA observations, these fluxes have been reconsidered. In fact, a lower expected flux is presented by Stecker in [31].

- **Gamma-Ray Bursts:**

  Discovered accidentally by US military satellites in 1967, GRBs are extremely luminous events. They have luminosities ranging from $\sim 10^{51}$ erg s$^{-1}$ to $10^{54}$ erg s$^{-1}$

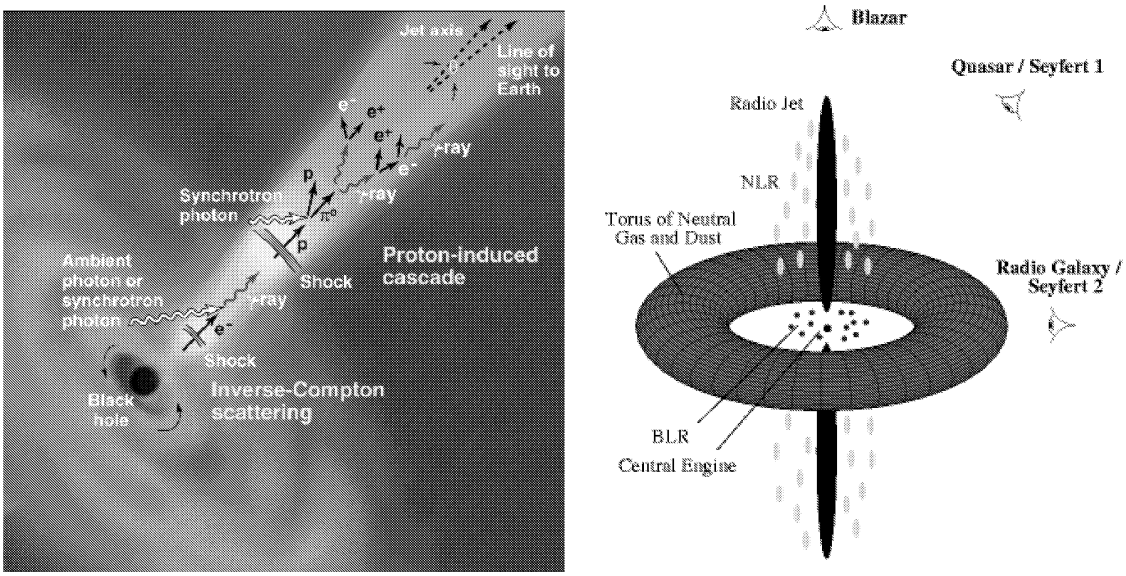


**Figure 1.8:** Sketch of a AGN (left side). Different types of AGN depending on the sight angle (right side).

assuming isotropic emission. However, if the burst is beamed in a particular direction, as is nowadays presumed, the outflow is lower. They emit very fast (from milliseconds to several minutes of duration) flashes of $\gamma$-rays, followed typically by several days of X-ray, optical and radio emission afterglow. Unlike the AGNs, they occur at apparently random positions in the sky several times per day, so it is not possible to predict when or where they will occur. GRBs can be divided in short hard-spectrum bursts (SHB) with a duration shorter than two seconds, and long soft bursts with more than two seconds of duration. Althought our knowledge has increased meaningfully in the last years thanks to Swift (NASA's multi-wavelength observatory dedicated to the study of GRBs), the origin of the GRBs is still unclear. Suggestions going from the collapse of a super-massive star to the merging of two compact objects as neutron stars have been proposed. There are two models which try to explain the GRB behaviour. In the leading model, a *fireball* expanding at relativistic energies and powered by radiation is produced from the central engine [32]. The GRB takes place as the result of internal shock waves produced when faster shells in the expanding material overtakes early and slower shells. In the *cannonball* model [33], a collapsar scenario is assumed where an accretion disk is created. Each time part of this accretion disk falls into the compact object, a relativistic cannonball is ejected and collides with the surrounding expanding shell originating the GRB. The Swift's observations for SHB fit well with the *fireball model*. However, X-ray flares in some afterglows observed by Chandra are not well understood in this scheme. On the contrary,

this effect can be better explained with the *cannonball model*.

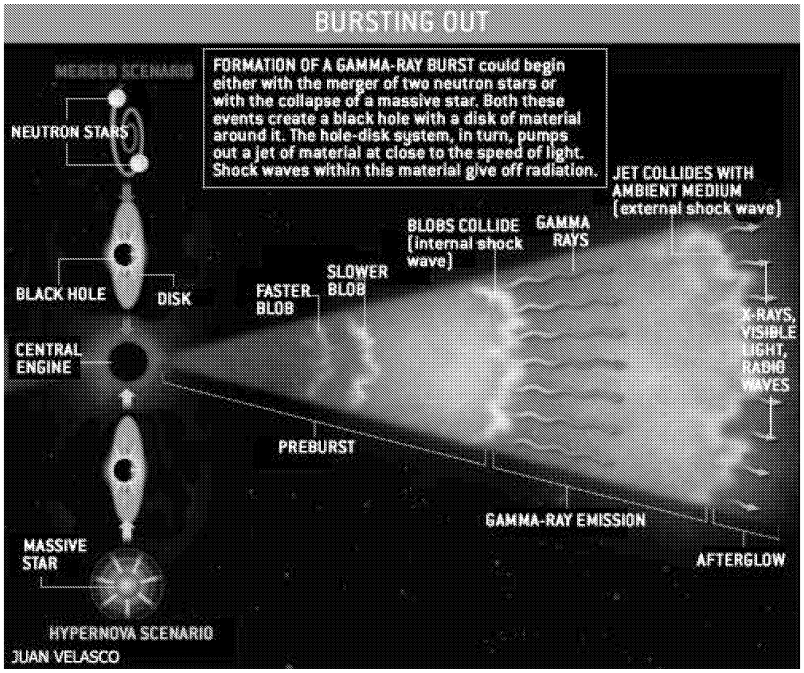


**Figure 1.9:** Sketch of a GRB explosion.

In the *fireball model*, a significant fraction of the fireball energy is converted into an accompanying burst of $10^{14}$ eV neutrinos [35] created by photomeson production of pions in interactions between the fireball $\gamma$-rays and accelerated protons. The neutrino burst is produced by the interaction of protons with energies much lower than $\sim 10^{20}$ eV (the maximum energy that protons may be Fermi accelerated in GRBs). Although the rate of GRB neutrinos is comparable to the atmospheric neutrino background, we should be able to distinguish them because of their correlation in time and angle with GRB $\gamma$-rays. The expectations, depending on models, are from 10 to 100 neutrino events reaching the Earth correlated with GRB emission in a km$^2$ neutrino detector [34].

### 1.4.4 Diffuse neutrinos fluxes and bounds in extragalactic sources

With neutrino telescopes smaller than a km$^3$ is not trivial to find clusters of detected events pointing to individual neutrino sources. However, one possibility to prove the existence of high energy extragalactic neutrinos, is to detect the neutrino flux of unresolved cosmic sources. Depending on the model, the expected rate for this diffuse flux in a 0.1 km$^2$ (e.g. ANTARES) is from 1 to 100 events per year [39]. This signal can be identified as an excess above the atmospheric neutrino background of high energy events. The main candidates to produce this diffuse flux are GRBs and AGNs.

Several constraints to the diffuse flux has been analyzed in the literature. E.Waxman and J.Bahcall gives an upper limit from the cosmic ray observations of $E \sim 10^{19}$eV (WB bound). In this upper bound, the decay of charged pions produced by photo-meson interactions, is considered the neutrino production mechanism. According to the authors, this upper bound is model independent and can not be avoided by cosmological evolutionary effects or invoking magnetic fields [40]. In the calculation it is also considered that the mean free path of high-energy cosmic rays for pion production is not much larger than the source size (AGN jets, and GRBs). The sources are transparent to high-energy neutrinos and have a generic $E^{-2}$ energy spectrum typical of schock acceleration. The value for this upper bound is:

$$E_\nu^2 \Phi_\nu < 1.5 \times 10^{-8} \xi_z \qquad \text{GeVcm}^{-2}\text{s}^{-1}\text{sr}^{-1}$$

where $\xi_z$ is a dimensionless parameter which depends on the cosmological evolution of the source. Evolution of star formation rate yields $\xi_z \approx 3$, on the contrary $\xi_z \approx 0.6$ for no evolution.

Recently A.Loeb and E.Waxman have proposed a lower bound from observations of starburst galaxies (galaxies experiencing a period of intense star forming activity, e.g. M82) [41]. According to them, the cumulative background of GeV neutrinos is:

$$E_\nu^2 \Phi_\nu \approx 10^{-7} \text{ GeV cm}^{-2} \text{ s}^{-1} \text{ sr}^{-1}$$

which can be extrapolated to higher energies as:

$$E_\nu^2 \Phi_\nu \propto E_\nu^{-0.15 \pm 0.1} \text{ up to } E_\nu \sim 0.3 \text{ PeV}.$$

This neutrino flux, comparable to the WB upper bound (Figure 1.10), is not in principle unexpected because it comes from sources optically thick. For a 1 km$^2$ detector, between 10 and 100 events with $E_\nu > 100$ TeV are expected per year.

### 1.4.5 Dark Matter

Dark matter is the generic name to refer to the matter particles of unknown composition which have the property of do not emit or reflect enough electromagnetic radiation to be detected. We know about their presence indirectly from gravitational effects on visible matter such as rotational speeds of galaxies. Moreover, recent Chandra observations have given direct evidences of dark matter existence via optical means in a collision of two large clusters of galaxies.

Dark matter can not be explained with nowadays known particles. Even considering the mass of the neutrinos, the matter is not enough to explain the gravitational effects seen. The models proposed to explain its origin assume that most of the dark matter is primarily non-baryonic, which includes new elementary particles such as WIMPs (weakly interactive massive particles) and axions.

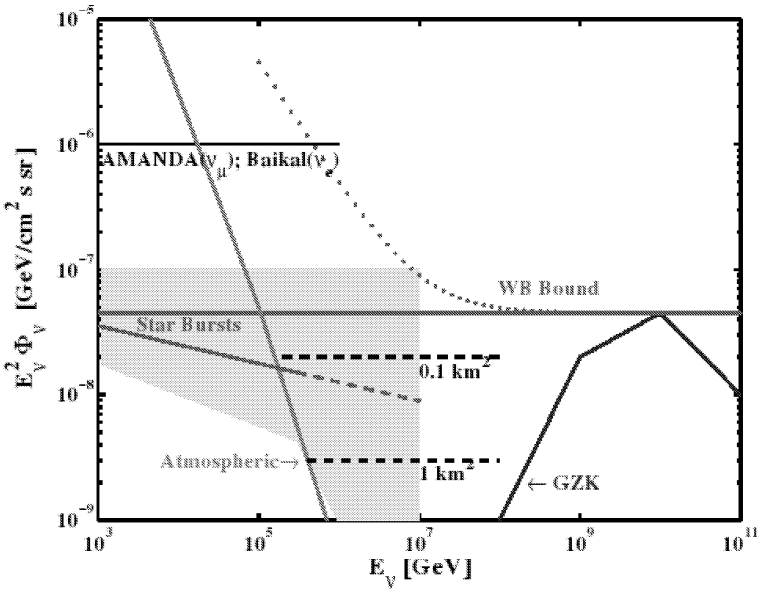


**Figure 1.10:** The shaded region brackets the range of plausible choices for the spectrum of the neutrino flux expected from observations of starburst galaxies. WB bound is also plotted, as well as the experimental upper bound of optical Cherenkov detectors (dashed lines) and atmospheric neutrino background.

In this sense, the lighest supersymmetrical particle (LSP) is one of the best WIMP candidates to explain the dark matter origin. This LSP, which is the neutralino in most supersymmetric models, would be stable if R-parity is conserved. They should be captured by massive bodies as the Earth, the Sun or the Galactic Centre due to scattering, and accumulate in their centres. Once the density increases enough, annihilation into fermion-antifermion would give rise to an observable neutrino flux at a given energy. The detection of this flux would provide an enourmous step in the determination of the nature of dark matter.

### 1.4.6 Other neutrino sources

The neutrino sources described in the previous sections are clear examples of the bottom-up acceleration mechanisms. Apart from that, there are the so-called top-down models. In these top-down models, the highest-energy cosmic rays are asssumed to be the decay products of cosmological remnants or topological defects associated to superheavy particles with GUT-scale masses. Most of these models have been proposed in order to explain the origin of the events above the GZK cut-off detected by experiments like AGASA. For the time being, there is no any evidence in the $\gamma$-ray detectors of their existence.

For instance, in the Z-burst model, UHE neutrinos annihilate with relic neutrinos

from the cosmic neutrino background. A Z boson resonance is produced which decays into high-energy protons as primary products and neutrinos as secondary products. They can be created close enough (< 100 Mpc) to avoid the GZK cut-off. Resonance energy, boson mass and neutrino rest mass, are connected by:

$$E_{res} = \frac{M_Z^2}{2m_\nu}$$

Calculations with an energy of 4 $\times 10^{22}$ eV for the primary neutrino, implies that the relic neutrino mass should be $\sim 0.1$ eV, which is compatible with the cosmological upper bounds on the neutrino mass. However, serious constraints concerning primary proton acceleration and neutrino luminosity at the sources, disfavour the Z-bursts models [36].

In other models, a combination of Z-bursts and superheavy dark matter (SHDM) decaying exclusively to neutrinos can avoid this problem and provide the theoretical expected fluxes [38].

## 1.5 Neutrino oscillation

One important neutrino intrinsic property to take into account when doing neutrino astronomy is neutrino oscillation. Neutrino oscillation is the clear evidence of the neutrino mass. Oscillations from one flavour to another are due to the fact that the states produced by the weak interaction are not eigenstates of the mass matrix but a linear combination of them.

$$|\nu_\alpha\rangle = \sum_{i=1}^{3} U_{\alpha i} |\nu_i\rangle$$

where $\alpha = e$, $\mu$, $\tau$ and i = 1, 2, 3.

Adding the time evolution to the state:

$$|\nu_\alpha(t)\rangle = \sum_{i=1}^{3} U_{\alpha i}\, |\nu_i(t)\rangle = \sum_{i=1}^{3} U_{\alpha i}\; e^{-iE_i t} |\nu_i\rangle$$

If we consider only two neutrino states, the oscillation probability between these two states as a function of the source distance is given by:

$$P_{\alpha\beta} = \sin^2(2\theta)\, \sin^2\left(1.27 \frac{L}{E} \Delta m^2\right)$$

where $\Delta m^2 = (m_\alpha^2 - m_\beta^2)$ in eV$^2$, $L$ is the distance between the neutrino source and our detector in meters and $E$ is the neutrino energy in MeV. As it is showed in the previous formula, oscillations takes place if $m_\nu \neq 0$ and also $\Delta \mathrm{m}^2 \neq 0$.

Neutrino oscillations have to be considered when computing neutrino fluxes from extraterrestrial sources. For instance, in pion decay the ratio for electron, muon and tau at the source is $\nu_e$:$\nu_\mu$:$\nu_\tau \sim$ 1:2:0. Taking into account oscillations, it is expected

that the rate turns out to be $\nu_e$:$\nu_\mu$:$\nu_\tau$ $\sim$ 1:1:1 due to the large distances from the sources.

### 1.5.1 Experimental evidences

The strongest evidence of neutrino oscillation was showed by the SNO (Sudbury Neutrino Observatory) collaboration [42] in 2001. The experiment measured the $^8$B solar neutrino flux using a water Cherenkov detector located at a depth of 6010 m of water equivalent in the Creighton mine. In this experiment, a non-$\nu_e$ component was detected with 5.3 $\sigma$ greater than zero, providing a strong evidence for solar $\nu_e$ transformation.

More recently, the K2K collaboration has presented data where no neutrino oscillations are excluded within $4\sigma$ (0.005 %) [43]. This experiment uses a $\nu_\mu$ (at 98%) beam produced in KEK neutrino accelerator. This beam, which has a mean energy of 1.3 GeV, is sent to Super-Kamiokande which is located 250 km from KEK. The aim is to detect the disappearance of $\nu_\mu$ (presumed to have oscillated to $\nu_\tau$) depending on the energy. For this purpose two detectors are used, one of 1 kiloton water Cherenkov placed 300 m close to the beam source, and another one of 50 kiloton water Cherenkov (Super-Kamiokande). A distortion of the neutrino energy has been observed as well as a deficit in the total neutrino number. The data best fits provide values of $\sin^2 2\theta = 1.0$ and $\Delta m^2 = 2.8 \times 10^{-3}$ eV$^2$.

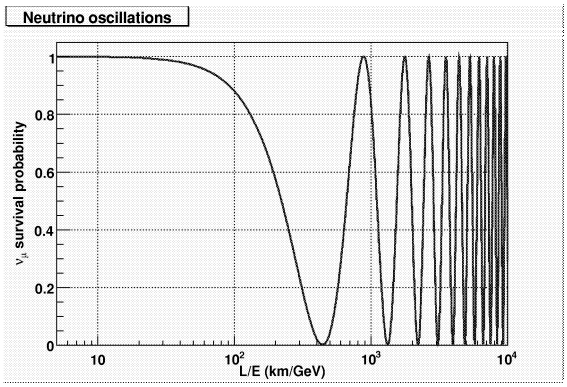


**Figure 1.11:** Variation of neutrino survival probability as a function of L/E with $\Delta m^2 = 2.8 \times 10^{-3}$ eV$^2$ and $\sin^2 2\theta = 1.0$

The neutrino telescopes can help in the oscillation parameter estimation, because they can detect the flux reduction occurring for muon neutrinos generated by cosmic ray interactions at the top of the Earth's atmosphere. That effect has already been confirmed by Super-Kamiokande. Therefore, neutrino telescopes will provide an independent measurement in the region $60 < L/E < 1250$ km/GeV, which would help in the neutrino oscillation interpretation.

# Chapter 2

# The ANTARES Neutrino Telescope

After a long period of development, research and test, the ANTARES collaboration has started the deployment of the neutrino telescope in early 2006 and it is foreseen to be completely installed by the end of 2007. In this chapter, a general description of the detector and its main features will be given.

## 2.1 Detection principle

The possibility to detect high-energy cosmic neutrinos with neutrino telescopes was conceived for the first time by Markov [44]. The aim of this kind of detectors is to detect the Cherenkov light induced by the muon produced after a charged current interaction of a cosmic neutrino with the matter surrounding the detector. To achieve light detection, a 3D-array of photomultipliers (PMT) placed in a suitable transparent medium like ice or water is devised.

The reactions involved are:

$$\nu_l(\bar{\nu}_l) + N \longrightarrow l^-(l^+) + X \qquad \text{charged current (CC)}$$
$$\nu_l(\bar{\nu}_l) + N \longrightarrow \nu_l(\bar{\nu}_l) + X \qquad \text{neutral current (NC)}$$

The differential cross-section for the charged current reaction, is given by [45]:

$$\frac{d^2\sigma}{dxdy} = \frac{2G_F^2 M E_\nu}{\pi}\left(\frac{M_W^2}{Q^2+M_W^2}\right)^2 [xq(x,Q^2) + x\bar{q}(x,Q^2)(1-y)^2] \tag{2.1}$$

where $G_F$ is the Fermi constant, $M$ is the nucleon mass, $M_W$ is the intermediate W-boson mass, the quantity $-Q^2$ is the invariant momentum transfer between the neutrino and the muon, $q$ and $\bar{q}$ are the quark and anti-quark distribution functions, and $x$ and $y$ are the Bjorken scaling variables:

$$x = Q^2/2M(E_\nu - E_l) \tag{2.2}$$

and

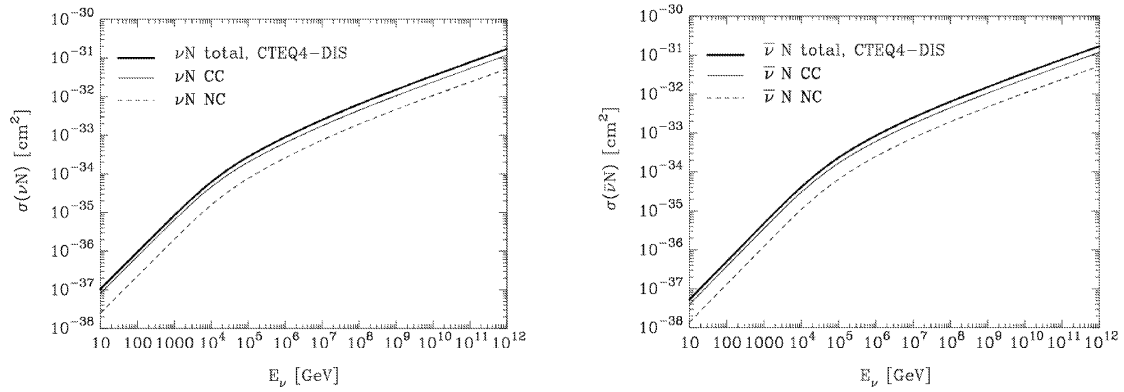


**Figure 2.1:** Cross section for $\nu_l N$ (left side) and $\bar{\nu}_l N$ (right side) interactions at high energies, according to the CTEQ4-DIS parton distributions.

$$y = (E_\nu - E_l)/E_\nu \tag{2.3}$$

Figure 2.1 shows the total cross section for energies from 10 to $10^{12}$ GeV according to the CTEQ4-DIS parton distribution. At low energies ($E_\nu \ll M_W^2/2m_N \approx 5$ TeV), there is a linear dependence with the energy:

$$\sigma_{CC}(\nu N) = (0.677 \pm 0.014) \times 10^{-38} \left(\frac{E_\nu}{1\ \text{GeV}}\right) \text{cm}^2 \tag{2.4}$$

$$\sigma_{CC}(\bar{\nu} N) = (0.334 \pm 0.008) \times 10^{-38} \left(\frac{E_\nu}{1\ \text{GeV}}\right) \text{cm}^2 \tag{2.5}$$

For higher energies ($E_\nu \gg M_W^2/2m_N \approx 5$ TeV) the CC cross section within 10% of uncertainty is given by:

$$\sigma_{CC}(\nu N) \simeq 5.53 \times 10^{-36} \left(\frac{E_\nu}{1\ \text{GeV}}\right)^{0.363} \text{cm}^2 \tag{2.6}$$

$$\sigma_{CC}(\bar{\nu} N) \simeq 5.52 \times 10^{-36} \left(\frac{E_\nu}{1\ \text{GeV}}\right)^{0.363} \text{cm}^2 \tag{2.7}$$

Even thought no $\nu_\tau$ are expected to be produced in cosmic sources, due to neutrino oscillations the ratio of the different neutrino flavours expected in the Earth is $\nu_e$:$\nu_\mu$:$\nu_\tau$ $\sim$ 1:1:1. Therefore, the three neutrino states can be detected. However, the ANTARES detector due to its size ($\sim$ 0.1 km$^2$), is optimized to detect high-energy muon events. This is because the muon energy losses are not very important up to $\sim$ 500 GeV (see section 2.1.2). In addition, they have a high life-time, therefore, the muons are able to travel very long distances before arriving to the detector (around several kilometers at $E \sim 1$ TeV). So good track reconstruction is expected for the muon case.

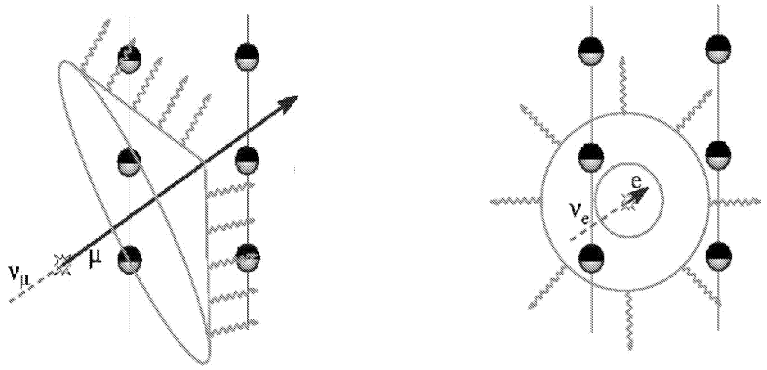


**Figure 2.2:** The track event (right side) and cascade event (left side), are the two possible event topologies that can appear in neutrino telescopes as ANTARES.

The electronic neutrino ($\nu_e$) events produce a hadronic cascade and an electron which provoke an electromagnetic shower at the interaction point. Because of the small dimensions of this cascade (few meters length) and the low PMT density on neutrino telescopes, this kind of events are seen as point-like events in the detector.

The $\nu_\tau$ events present a similar signature for energies below a few PeVs, where the tau track is too short to be separated from the shower, so these events will contribute to the shower rate. At higher energies, due to the Lorentz space expansion ($L = \beta c\tau\gamma$)[1], the tau track will extend beyond the initial shower, and will decay producing a second shower. This creates an identifiable double-bang pattern which would be background free.

Considering all these properties, two main event topologies can appear in a neutrino telescope (Figure 2.2): track events, which is the case for muons and taus with $E >$ 2 PeV; and cascade events, which is the case for electrons, taus with $E < 2$ PeV and products of neutral current interactions. In a real event, a combination of both topologies is expected.

Knowing Cherenkov emission properties and the lepton's propagation in water, it is posible to reconstruct the track with the position and arrival time recorded for the event in our 3D-array, as well as an estimation of the event energy from the charge collected in the PMTs. In fact, the reconstructed track is not the neutrino track but the muon one. However, this muon is aligned with the incident neutrino to within a degree for neutrino energies greater than 1 TeV. This angular accuracy allows neutrino astronomy and depends approximately as $1/\sqrt{E}$. This relation can be parameterized for $E_\nu > 10$ TeV as:

$$\langle\theta_{\mu\nu}\rangle = \frac{0.64^o}{(E_\nu/TeV)^{0.56}} \tag{2.8}$$

[1]For instance, a $\tau$ with $E_\tau$=1 PeV and $\tau_\tau$=290.610$^{-15}$s travels ~50 m.

### 2.1.1 Cherenkov emission

Cherenkov emission was detected for the first time in 1934, when P. A. Cherenkov observed the emission of blue light from a bottle of water exposed to radioactive bombardment. This radiation appears when a charged particle travels through a medium at a speed greater than the speed of light in the medium, so the condition for a particle to produce Cherenkov light is $\beta{>}1/n$, where $n$ is the refractive index of the medium. Thus, a fraction of the particle energy is emitted as an electromagnetic shock wave with low intensity. In fact, the energy losses due to ionization are 2 or 3 orders of magnitude greater than the energy losses due to Cherenkov emission.

The Cherenkov radiation propagates as a cone whose opening angle depends on the particle velocity as:

$$\cos\theta_C = \frac{1}{\beta n} \tag{2.9}$$

For ANTARES, which is placed underwater the refraction index is $\simeq 1.35$ for a wavelength of 450 nm, so $\theta_C \simeq 42\ ^o$.

The number of photons ($N$) emitted per unit length ($x$) and wavelength ($\lambda$), induced by a particle with charge $Z$ and speed $\beta$, in a medium of refractive index $n$ is given by:

$$\frac{d^2N_\gamma}{dxd\lambda} = \frac{2\pi\alpha Z^2}{\lambda^2}\left(1 - \frac{1}{\beta^2 n(\lambda)^2}\right) \tag{2.10}$$

As it is shown in the previous formula, the number of emitted photons increases with the frequency (shorter wavelength). Therefore, the major part of photons emitted in Cherenkov radiation are produced in the ultraviolet region of the electromagnetic spectrum. This is why visible Cherenkov radiation is observed to be brilliant blue.

Integrating the expresion 2.10, it can be shown that there is an emission of $\sim$100 photons within 1 cm of flight path in the range from 400 to 500 nm, where the efficiency of the ANTARES PMTs and the transparency of the water are maximum.

### 2.1.2 Muon propagation in matter

As we saw previously, muons produced after $\nu_\mu$ charged current interaction are the best candidates to do neutrino astronomy. Therefore, a good knowledge of the muon propagation through the detector media (i.e. rock and water) is crucial.

Muon energy losses in matter come from ionization and radiative processes, where radiative includes pair production, bremsstrahlung and photonuclear reactions. These energy losses can be written as [46]:

$$\frac{-dE}{dx} = a(E) + b(E)E \tag{2.11}$$

where $a(E)$ accounts for the ionization contribution and it is given by the Bethe-Bloch equation. On the other hand, $b(E)$ describes the radiative contributions. When ionization and radiation losses are equal on average the critical energy is defined as

$E_{\mu c} = a(E_{\mu c})/b(E_{\mu c})$. For muons, this critical energy occurs at $\sim$ 600 GeV and $\sim$ 500 GeV for water and "standard rock" respectively.

### 2.1.3 Physical background

The light induced by extraterrestrial neutrinos is not the only light that can be recorded in the ANTARES PMTs. Optical background (section 2.2.1) and physical background, which is caused by atmospheric muons and the muons induced by atmospheric neutrinos, can also produce recordable light in the PMTs. This latter physical background is produced as secondary products by the interaction of primary cosmic rays in the Earth atmosphere. Figure 2.3 shows the atmospherical muon flux and neutrino induced muon flux as a function of the zenith angle expected for a 2300 m water depth location.

To avoid the atmospheric muon background, neutrino telescopes like ANTARES, are constructed at large depths. In fact, this muon background can be completely avoided at 10 km water depth, but such a depth is logistically impossible to attain. ANTARES will be deployed at 2500 m depth, therefore atmospheric muons will be detected and a criteria to reject them will be needed. The way conceived by the ANTARES collaboration is to use $45^o$ downward oriented PMTs, and consider only upgoing muon tracks. Since the Earth acts as a shield for no-neutrino particles, the upgoing muon events have to be caused by neutrinos. Consequently, ANTARES will cover the opposite sight of the sky that would be seen with a conventional photon telescope in the same location.

However, there will be still an unavoidable background due to muons induced by atmospheric neutrinos. The rejection in this case is based on different appoaches depending on the sources. For point-like sources, the clustering of events makes this background negligible due to its isotropic distribution. For diffuse fluxes, the rejection is based on the different spectral indexes of atmospherical neutrinos and cosmic neutrinos, being greater for the atmospheric case (see section 1.4.2). Therefore, the atmospheric neutrino flux decreasses faster with energy than the cosmic neutrino flux. At $\sim$ 100 TeV, cosmic neutrino flux is higher than the atmospheric flux (see Figure 1.4).

## 2.2 The ANTARES project

Created in 1996, the ANTARES project (Astronomy with a Neutrino Telescope and Abyss environmental RESearch) [47] is an european collaboration with more than 200 physicists and engineers from 6 countries, which aim is to build a neutrino telescope in the Mediterranean sea at 2500 m depth, and separated 40 km from the Toulon coast ($42^o$50'N $6^o$ 10'E) (Figure 2.4). This detector will be made up of 12 lines with 25 storeys each, and 3 PMTs per storey that means 900 PMT in the whole detector. These PMTs are protected by a high-pressure resistant glass container which, together

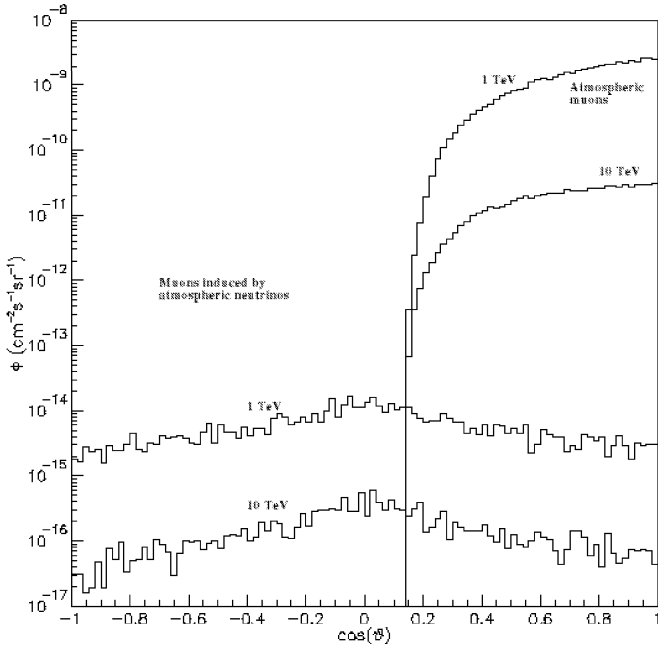


**Figure 2.3:** Muon and neutrino induced muon flux at 2300 depth plotted as a zenith angle function. Two energies are considered.

with the base and the associated electronics, form the so-called optical module (OM).

The connection with the shore is performed with a 40 km electro-optical cable which links the shore station with the junction box where the power supply, clock signals and commands are splitted and distributed to the 12 lines. On each line, the distance between the anchor and the first storey is of $\sim$ 90 m. The remaining storeys of the line are $\sim$ 14.5 m separated each other. A sketch of the detector and its horizontal layout is shown in the Figure 2.5. The criteria to select this detector configuration is a compromise between the cost and the effective area achievable for 1-100 TeV neutrinos.

The ANTARES location has been chosen after the site evaluation period, where several studies were done with autonomous instrumentation lines in order to evaluate the feasibility of the project in this hostile environment.

### 2.2.1 Optical background

The ANTARES underwater location provides an unavoidable optical background caused by $^{40}$K decays (because of the diluted salt in water) and biological activity. This background rate can be described by two main components [48].

One continuous baseline component which has two sources: the Cherenkov light emitted by the electrons produced in the $^{40}$K $\beta$-decays and the biological activity due to bacteria colonies. This biological contribution can produce variations in the baseline

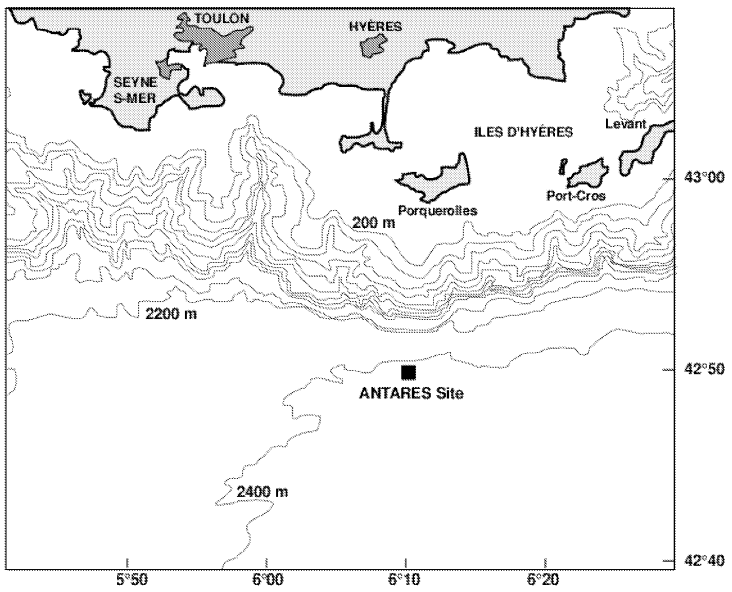


**Figure 2.4:** ANTARES site map. ANTARES is located 20 km far away from Porquerolles island and 40 km from La Seyne.

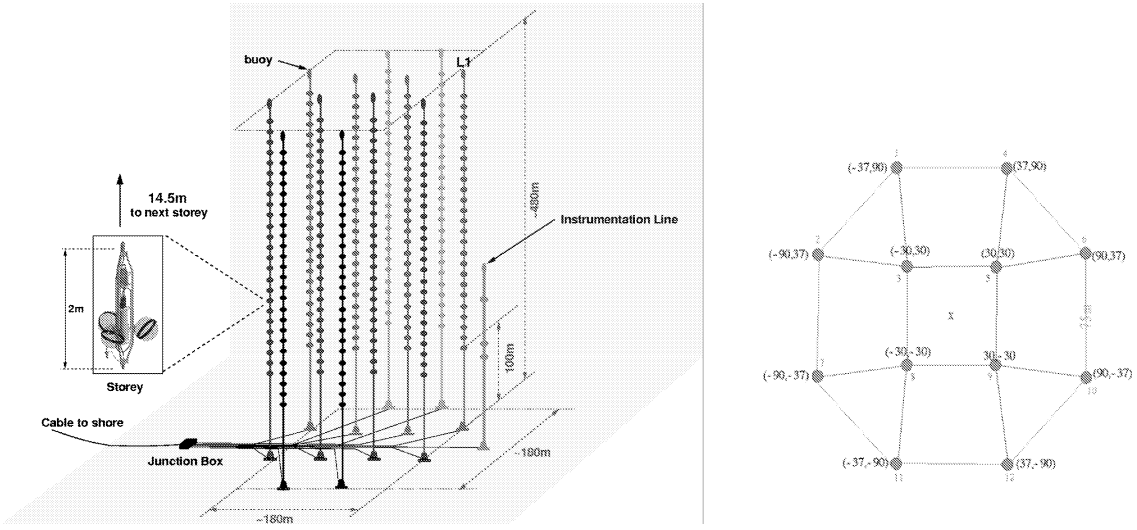


**Figure 2.5:** A general view of the ANTARES detector placed at the sea bed. It is composed by 900 PMTs distributed in 12 lines (left side). Horizontal view showing how the lines are distributed (right side).

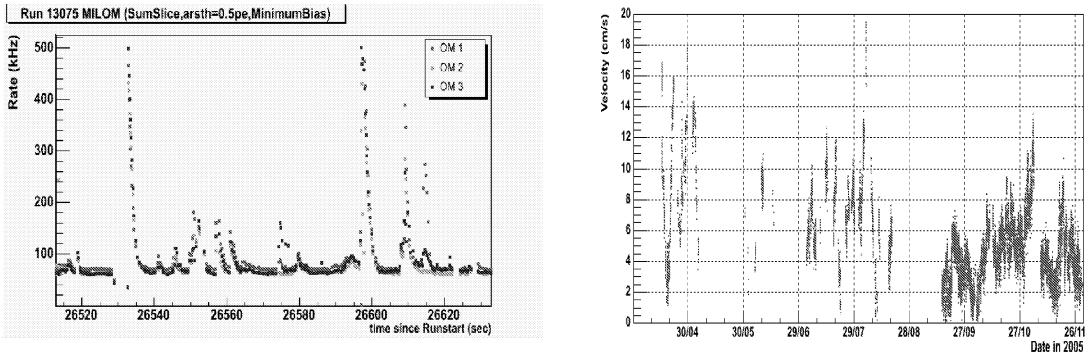


**Figure 2.6:** Optical background measured at 0.5 p.e. threshold (left side). Current velocity (right side). Both measured with the instrumentation line (MILOM) at the ANTARES site.

rate in a long time period. The continuous rate has a typical value of $\sim$ 35 kHz[2] which can fluctuate as much as 14 kHz on a time scale of a few hours, simultaneously in all the OMs, even 40 m separated.

The second component in the optical background is formed by short bursts (generally lasting for hundred of micro-seconds to seconds) which are only simultaneously recorded in nearby OMs, and are observed overimposed on the constant baseline due to their high rates (20% over the baseline). These bursts are attributed to the light-emitting organisms which cross accidentally the detector and, in principle, are not correlated with the continuous component caused by the bacteria colonies. The burst rates achieve values $>$ 200 kHz and, therefore, can lead the acquisition system to an appreciable dead time. Rate dependence on the site, season and undersea current velocity has also been observed (Figure 2.6).

### 2.2.2 Biofouling and sedimentation

An important effect to take into account in underwater neutrino telescopes is the biofouling. This is a natural process caused by bacteria adhesion or by sedimentation in the OM surfaces spoiling its transparency. That feature was tested for the ANTARES site using a mooring line equipped with suitable devices [49].

As it is seen in the figure 2.7, the light transmission shows a general tendency to decrease with time. Some recoverings which are correlated with water current velocity are observed, showing that surfaces are fouled by sediments more than by microbial adhesion and growth. As it is shown, light transmission is maximun at $\theta = 90^o$ (equatorial) zenith angle, where a global loss of $\sim$ 2 % is expected after one year of operation.

[2]This rate depends on the photocathode diameter. In this case, a 8" photocathode is considered instead of the 10" ANTARES final photocathode.

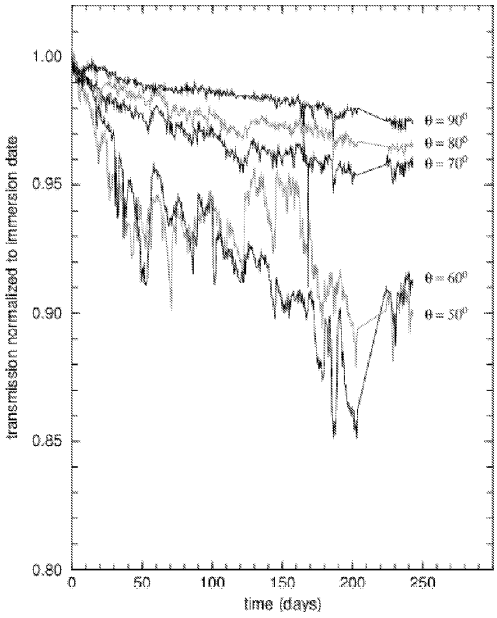


**Figure 2.7:** Light transmission decreasing as a function of time. Five angles for OM orientation are considered.

Average loss sensitivity for the ANTARES OMs is expected to be smaller, because they are downward oriented with a zenith angle of $135^o$. Therefore, it is foreseen that during the years of ANTARES data taking, fouling will not involve a considerable problem.

### 2.2.3 Optical properties of water

The most important properties which governs the light attenuation in water are the scattering[3], which affects to the angular resolution, and the absorption length[4], which affects to the optimization of the line separation distances. These parameters depend on the wavelength, and are correlated by the equation:

$$\frac{1}{\lambda_{att}^{(eff)}} = \frac{1}{\lambda_{abs}} + \frac{1}{\lambda_{sct}^{(eff)}} \tag{2.12}$$

In this equation, magnitudes are written as more frequently used "effective" magnitudes, where the average cosine angle for single scattering is taken into account:

$$\lambda_{sct}^{eff} \equiv \frac{\lambda_{sct}}{1 - \langle \cos\theta \rangle} \tag{2.13}$$

[3]defined as travel length where the probability of no-suffering any scattering has decayed in a factor $e$.

[4]defined as travel length where the no-absorption probability has decayed in a factor $e$.

| Epoch | Wavelength(color) | $\lambda_{att}^{eff}$ | $\lambda_{abs}$ | $\lambda_{sct}^{eff}$ |
|---|---|---|---|---|
| June 2000 | 466 nm (Blue) | $46.4 \pm 1.9 \pm 2$ | $49.3 \pm 0.3 \pm 2$ | $301 \pm 3 \pm 27$ |
| | 370 nm (UV) | $26.0 \pm 0.5 \pm 1$ | $28.9 \pm 0.1 \pm 1$ | $133 \pm 3 \pm 12$ |

**Table 2.1:** Results for the optical properties of the water taken during June 2000 campaign for blue an UV. The first is the statistical error and the second is the systematic one.

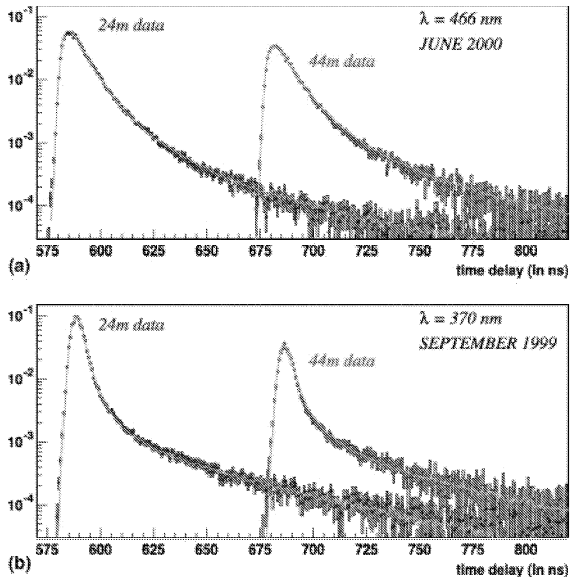


**Figure 2.8:** Distributions of the LED photon arrival times with the Monte Carlo fit superimposed for different wavelengths and distances.

In a neutrino telescope like ANTARES, the sea water where the PMTs will be distributed, constitutes itself part of the detector. Therefore, the knowledge of the optical properties of the water is crucial to optimize the design and the detector performance. The ANTARES collaboration has measured these optical properties in several sea campaigns using different experimental setups, and testing them at different sites [50]. The main setup used was an isotropic light source (pulsed LEDs) emitting in two different wavelengths (blue and UV). The light was collected in a small PMT of 1" diameter, and the relative separation between the source LED and the PMT could be changed.

Results of the June 2000 campaign are summarized in Table 2.1. The values were taken for blue and UV because these are the wavelength where ANTARES PMTs are more efficient. In the Figure 2.8, the distribution of the LED photon arrival times is plotted and compared with the expected Monte Carlo. A scattering tail is clearly shown.

## 2.3 The ANTARES devices

A detailed description of the more relevant ANTARES devices is given in this section.

- **The Optical Module:**

  The OM [51] (Figure 2.9) is the most relevant device of the ANTARES telescope, since it contains the PMT which will detect the muon induced Cherenkov light.

  The OM is composed by a glass sphere made up of borosilicate, with 432 mm of diameter and 15 mm of thickness. This sphere is devised to support high pressures of about 260 atm at normal operations and 700 atm on qualification tests. Its refractive index is 1.47 in 300 - 600 nm range, and light transmission is $> 95$ % above 350 nm.

  The PMT housed on the glass sphere must meet several requirements in order to provide the best performance for physics research. For this reason, some PMT models were put under test before the final selection of the Hamamatsu R7081-20 model [52]. This model have a 10" photocathode diameter, a gain $> 5 \times 10^7$ working at nominal high-voltage ($> 1000$V), a peak to valley ratio $> 2$, a transit time[5] spread (TTS) $< 3$ ns and a dark noise $< 10$ kHz for a 0.25 p.e. threshold.

  In order to reduce the influence of the Earth's magnetic field, which can degrade the TTS of the PMT, a $\mu$-metal cage with high magnetic permeability has been conceived. Fixing the $\mu$-metal, the PMT and the glass sphere, there is an optical glue which is highly transparent and has been devised with an appropriate refraction index to reduce reflection.

  Finally, an internal built-in LED, placed on the back of the PMT, is used for internal calibration and monitoring of the PMT transit time.

- **Storeys:**

  All the elements of the storey are held by a titanium frame used as mechanical support for the OMs, the Local Control Module (LCM), the hydrophones and the LED optical beacons (LOB).

  Each storey contains a triplet of OMs facing downward $45^o$ according to the ANTARES design. An LCM is placed in the center, as can be seen in the Figure 2.10.

  All the electronic commands as clock, slow control, HV supply or readout, arrive to the OMs via the electronic boards housed in the LCM container which is designed to protect them from high pressures thanks to its titanium frame. The most significant electronic board is the Analogue Ring Sampler (ARS) which is

[5]The transit time of the PMT is the time from the light arrival to the photocathode up to the output of the signal in the anode.

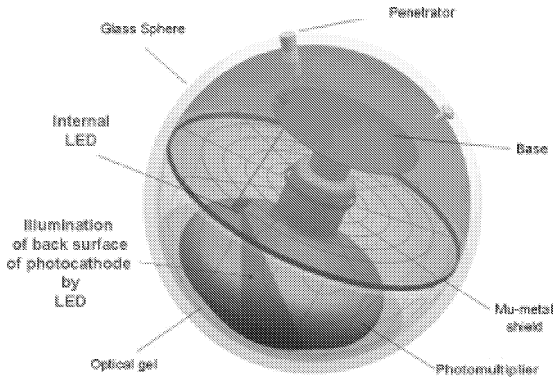


**Figure 2.9:** Schematic view of the ANTARES Optical Module with its components.

in charge of digitalize the signals coming from the OMs, giving information about the amplitude, time and shape of the signal (see section 2.4.1)

Other instruments that do not appear in all the storeys but can be part of it are: a receiving Rx hydrophone (5 per line), devised for the acoustic positioning system, and a LOB (4 per line), devised for timing calibration.

- **Lines:**

  As it has been said, ANTARES is composed by 12 lines. Each line contains 25 storeys and has a length of $\sim$ 450 m. Every five consecutive storeys define a sector. In each sector, one particular LCM is called the Master Local Control Module (MLCM) and contains the Ethernet switch which concentrates the data traffic coming from the other 4 LCMs and from itself. The lines are anchored to the sea bed by the Bottom String Socket (BSS), and a buoy at the top give it vertical support. The instruments that we can find in the BSS are: an acoustic RxTx hydrophone, a pressure sensor and a sound velocimeter. The BSS of the instrumentation line (MILOM) has, in addition, a Laser Beacon for timing calibration. The String Power Module (SPM), which provides the power supply to the BSS instruments and to all the LCMs in the string, is also placed on the BSS. There is also in the BSS the String Control Module (SCM), which contains the electronics required by the slow control system, the clock and the instruments of the BSS. The SCM also takes the control of the data traffic to the line MLCMs.

  Moreover, for positioning purposes and spatial calibration, the detector has an acoustic system as well as compasses and tiltmeter sensors. The acoustic system exchanges signals in the 40-60 kHz range, using RxTx (receiving and emitting) transponder hydrophones located in each BSS, and in 3 autonomous pyramids fixed at the sea bed. The acoustic system is completed by five receiving hydrophones distributed on each line. Every LCM houses a compass and a tiltmeter card. The tiltmeters provide the pitch and the roll angles of the storey

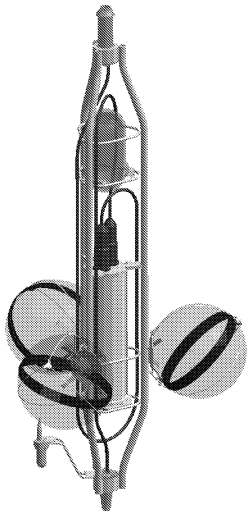

**Figure 2.10:** Schematic view of a storey. There are represented 3 OMs facing $45^o$ downward, one LCM in the center housing the readout electronic cards, one Rx hydrophone for positioning and one LED beacon for timing calibration purposes.

with respect to the horizontal plane. The compasses provide the magnetic field and the heading of OM 0 with respect to the North magnetic pole of the Earth. The Positioning System provides accuracies of $\sim$ 10 cm in the OM position.

Furthermore, 4 blue LOB are distributed along the line for timing calibration. These LOB, which will be described in Chapter 3 in more detail, represent a controllable pulsed light source to perform in situ calibration and monitoring of the time off-sets values measured previously in the laboratory.

- **Junction box and main electro-optical cable:**

  The connection between the shore station and the detector is made by the main electro-optical cable (MEOC) which is 40 km long. It has 58 mm of diameter and is composed of 48 monomode pure silica optical fibres. It is designed to provide all the electronic commands, clock, power supply, etc. This cable arrives up to the junction box, a kind of vessel made up of titanium (Figure 2.11) which splits the signals from the MEOC and links the lines by an electro-optical interconnecting link (IL) cable. The signals from the junction box are received in the BSS of each line which is in charge of distribute them to the whole line.

## 2.4 The DAQ system and readout electronics

The data acquisition system takes care of the PMT signal digitization, as well as the data transport, filtering and storage. An schematic view of the ANTARES DAQ

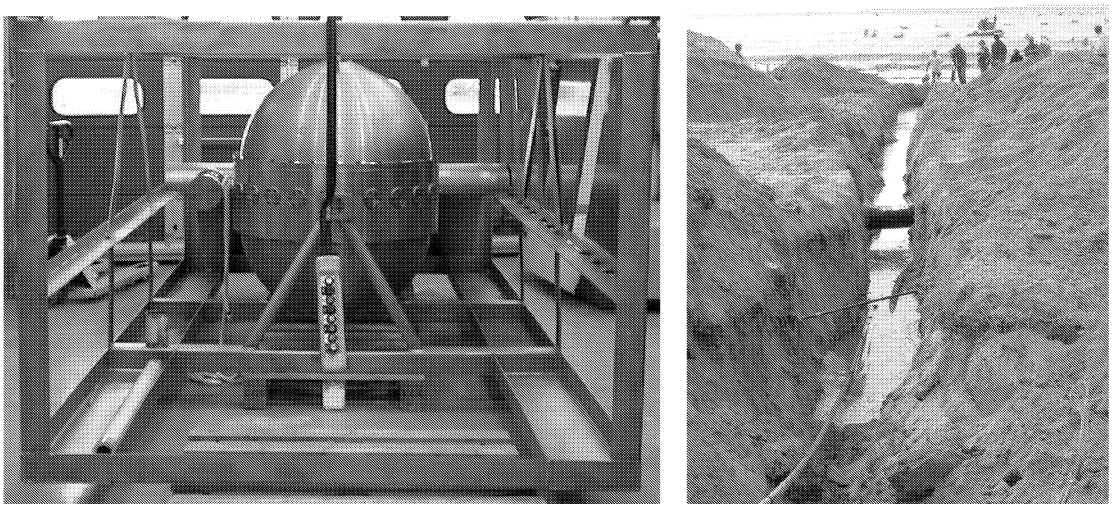

**Figure 2.11:** A photo of the junction box (left side), and of the main electro-optical cable deployment (right side).

is shown in the Figure 2.12. This system has been optimized according to the requirements that such underwater location needs. In particular, the PMT signals are digitized off-shore since the analogical transmission can produce losses in the information due to the long distance between the shore station and the detector.

On every storey, the Local Control Module (LCM) contains the electronics needed for the readout of the 3 photo-multipliers. Each LCM houses several Analogue Ring Sampler (ARS) ASIC[6] chips [83], where the signals coming from the PMTs are digitised. Basically, the ARS digitization provides the time and charge of each PMT signal. This combined information defines a Single Photo Electron (SPE) hit. The readout of every PMT is done with 2 ARS to reduce the dead-time (about 200 ns). The LCM of the storeys where there is also a LED beacon, has in addition another ARS for the readout of the internal PMT[7].

The information registered by the LCMs is sent by sectors (group of 5 storeys) to the MLCM. The MLCM data goes to the SCM placed at the line anchor. After that, the data from the whole detector (12 lines + instrumentation line) goes to the JB and subsequently to the shore station.

The sketch of the data transmission is shown in the Figure 2.17.

The volume of raw data expected for the whole detector is around 0.4 GB/s assuming a data rate of 70 kHz. Most of this data are originated from the high background rates caused by bioluminiscense and $^{40}$K decay. Because of this very high volume of

[6]Application Specific Integrated Circuit.

[7]For the laser beacon placed in the instrumentation line, there is also a specific ARS in the SCM, for its photodiode readout.

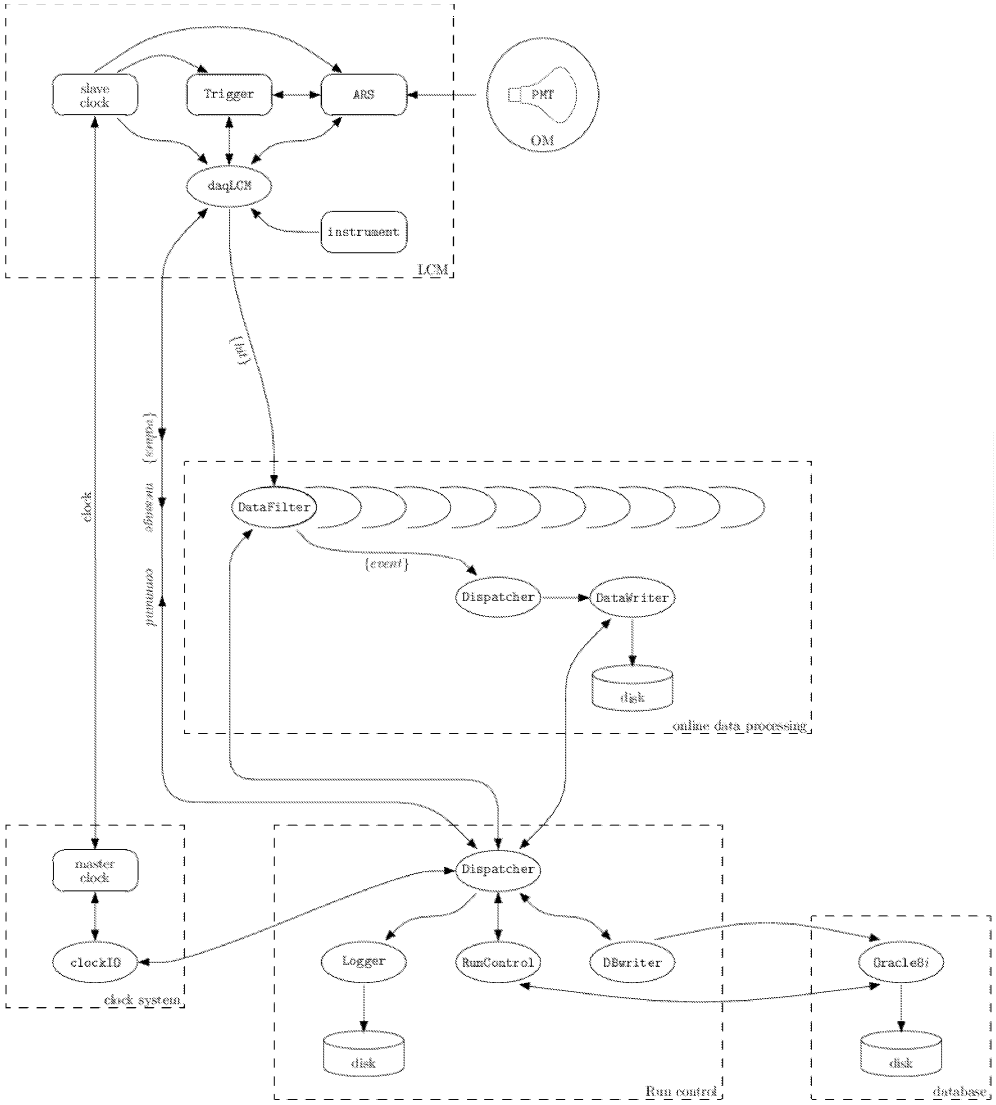


**Figure 2.12:** Sketch of the ANTARES data acquisition system. The ellipses correspond to processes and the boxes to hardware devices.

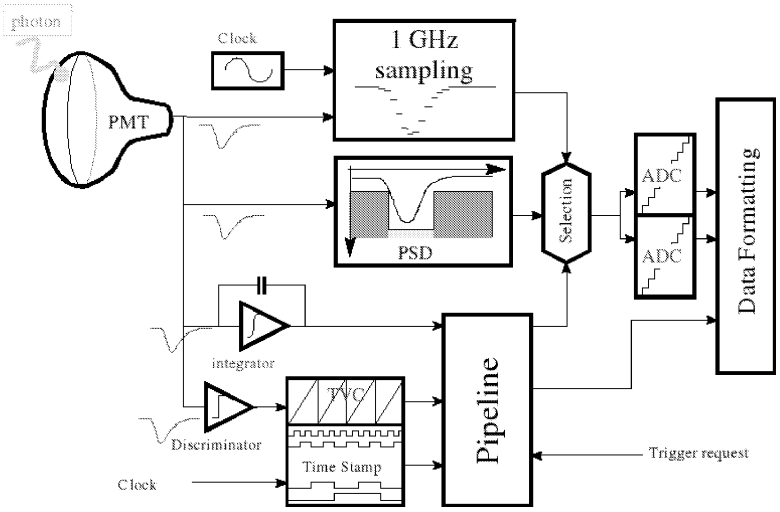


**Figure 2.13:** Sketch of the internal ARS processes that take place when a signal PMT arrives.

data, a filtering system is necessary to reduce it.

Once the data is on-shore and has been processed, it is written on disk and afterwards, sent to "Centre de Calcul de l'IN2P3" at Lyon.

The DAQ system and its associated electronics have been successfully tested in the MILOM and the Line 1.

### 2.4.1 The ARS

Figure 2.13 shows schematically the process followed by a PMT signal in the ARS. With the aim of reducing the dark-current noise of the PMT, the first step is to surpass the L0 threshold whose the typical value corresponds to 1/2 of photo-electron. When this threshold is crossed, a timestamp (TS) and a time to voltage converter (TVC) value are generated providing the time information. Symultaneously, the charge is integrated and a Pulse Shape Discriminator (PSD) analyses the pulse shape classifying the signal as single photo-electron (SPE) or waveform (WF). Both, WF and SPE modes, provide the charge and time values, however, the WF mode can gives a more detailed information because the analogue signal is divided in 128 samples of $\sim$ 1.5 ns of duration. This mode is very useful in order to do further analysis of the signals as calibration and timing parameter calculations. However, it produces a big amount of data and, for physics analysis SPE signals provide enough information.

In a second step, the information of the pulse (SPE or WF), charge and time, goes to a pipeline memory made up of 16 cells, which is able to handle 16 SPE hits or 4 WF hits. This process releases the ARS in order to acquire new hits without waiting for the precedent hit digitization. The hits in the pipeline memory are digitized by the

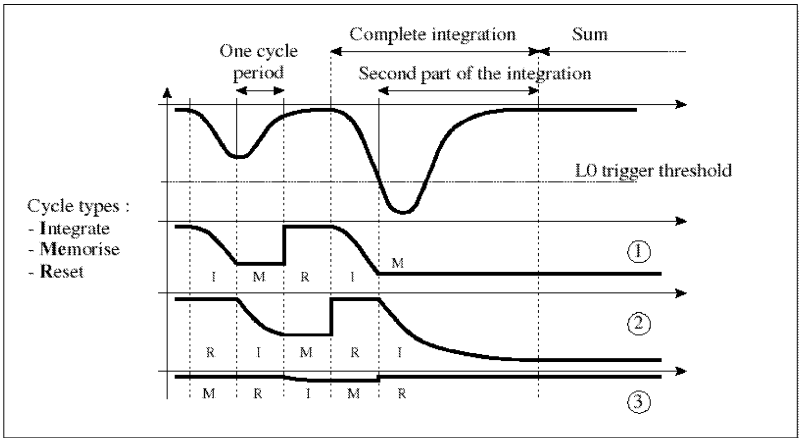


**Figure 2.14:** Charge signal integration with the 3 capacitors working in different phases. When the L0 is crossed, the phase remains fixed during the time integration period.

Analogue to Digital Converters (ADC). The digital values for the charge (AVC) and time (TS + TVC) are generated for the selected hits and sent to the shore station. Afterwards, the pipeline memory is released to repeat the process.

### Charge measurament

The PMTs have a nominal gain of 5 $\times 10^7$ which gives, for a single photo-electron collected in the PMT anode, a signal of about 45 mV (50 $\Omega$ load). The charge integration is carried out by parts in order to get all the charge. This is done by means of 3 capacitors (Figure 2.14) which are each one in a different phase: the integration phase (I), where the signal from the anode is integrated, the memorisation phase (M), where the charge integrated is recorded in memory, and the charge erasing phase (R), where a reset is done. These phases have a fixed but adjustable time cycle duration between 8 and 30 ns, which is slightly longer than the PMT rise time[8] ($\sim$ 5 ns) on purpose. When a hit crosses the L0 threshold, the time integration is increased in order to cover all the signal pulse shape. Then the duration is fixed between 17 to 50 ns. Finally, the charge integrated value is obtained as the sum of the two capacitors in the integration and memorisation phase.

After this process, the integrated charge is digitised by an 8-bit ADC called analog to voltage converter (AVC) which provides values from 0 to 255. The conversion from AVC units to charge units (in photo-electrons) has been computed in the laboratory for each specific ARS. The results show that the relation AVC-charge can be considered lineal following the relation:

[8]rise time is defined has the elapsed time between the 90% and the 10% of the amplitud signal.

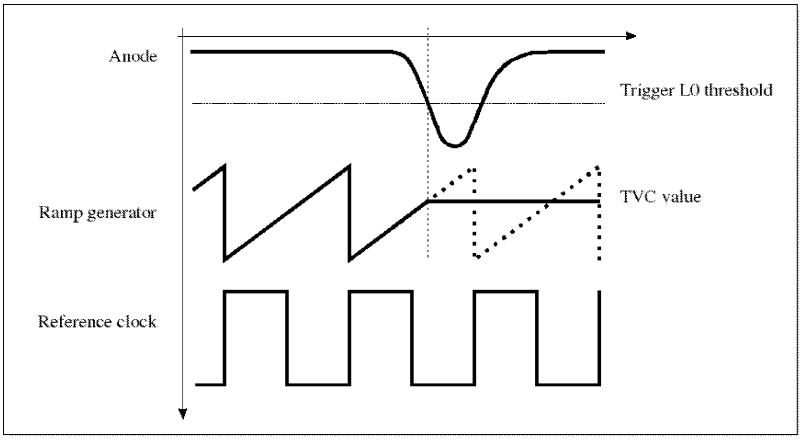


**Figure 2.15:** Time measurement done in the ARS. A time stamp and a TVC value are generated when the signal cross the L0 threshold.

$$Q_{pe} = \frac{AVC - AVC\_0}{AVC\_1 - AVC\_0} \tag{2.14}$$

where $AVC\_0$ is the peak of the pedestal [84] and $AVC\_1$ is the photo-electron peak. The $AVC\_1$ and $AVC\_0$ values are calculated for each ARS, and stored in the ANTARES database. The values obtained show important differences among ARSs.

The ANTARES detector expects hit charge measurements with a relative error smaller than 10%.

### Time measurament

The time information of every hit is provided by the TS and the TVC values. The timestamp (TS) gives the number of half clock cycles (25 ns) from the last reset time stamp (RTS). The TS is referred to the last RTS because the ARS has an internal clock which is reset every RTS. With the last RTS and the TS, we can know the time from the beginning of the run of every hit recorded with 50 ns accuracy. The absolute time can be obtained in this way, because of the clock system is synchronized with the Universal Time by assigning the GPS time to the data.

Moreover, a higher precision can be reached with the time to voltage converter (TVC) given by an 8-bit internal ADC in the ARS. This ADC provides a subdivision of the clock cycle in 256 parts, therefore, a precision of about 200 ps is attainable. The Figure 2.15 shows how the TVC works. There is a ramp generator which provides a voltage proportional to the time within a clock cycle duration. When a PMT signal crosses the L0 threshold, the ramp voltage is frozen and memorized providing the TVC value. Because of the dead time in the ramp generator spent on recover the ramp shape, a flip-flop system based on two TVC ramps is used.

In the ideal case, we would have the start of the TVC ramps synchronised with the

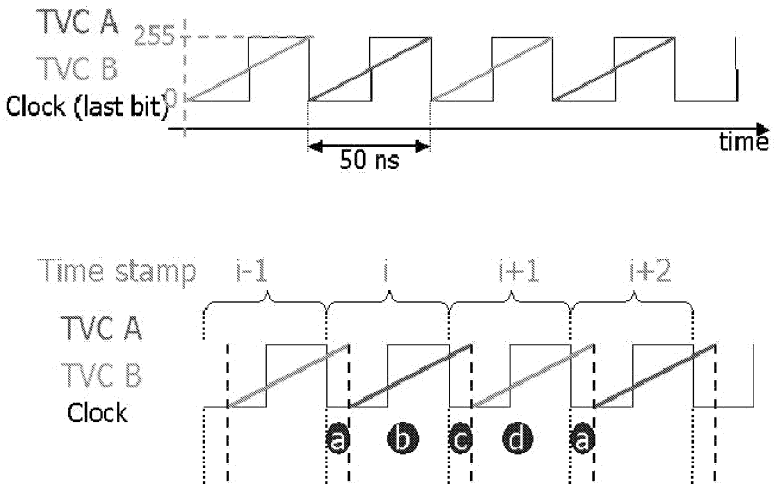


**Figure 2.16:** The ideal case (top) and the real case (bottom) of the TVC with respect to clock cycles (TS).

clock cycles. However, a shift between them appears in the real case (Figure 2.16). This effect has to be considered when computing the hit time and the TS value has to be corrected to match with the real time value.

### 2.4.2 The DAQ software

The software programs which controls the DAQ are interconnected as it is shown in the Figure 2.17. The RunControl is the main program used to operate the detector. A view of its graphical user interface can be seen in the Figure 2.18. It controls all the system processes, which are called clients. On every LCM, the *DaqHarness* process organizes the raw data coming from the ARS chips, in packets of 13107200 ns of duration called *Frames*. All the frames belonging to the same time window are sent to a specific PC on shore, and merged in a so-called *TimeSlice*. The *DataFilter* program running on each PC processes the TimeSlices looking for *PhysicsEvents* data corresponding to a group of correlated hits in different parts of the detector. The required calibration parameters are obtained from a dedicated database based on the Oracle database management system [82]. Finally, the data is written on disk by the *Datawriter* process. Subsequently, these files are ready for physics analysis and are copied regularly to the computer centre at Lyon, where can be downloaded by the authorized users.

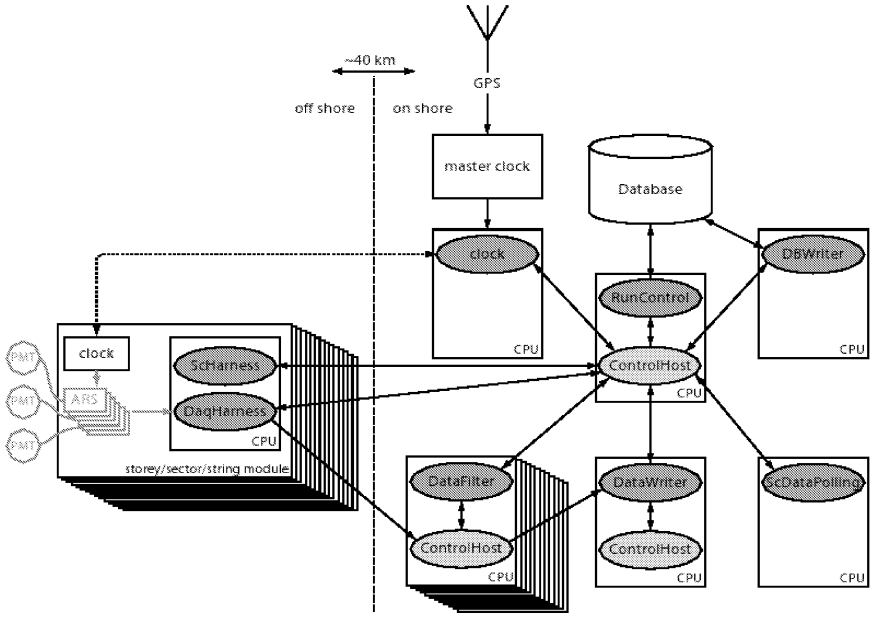


**Figure 2.17:** Schematic view of the main processes in the DAQ system. The processes are separated in on-shore and off-shore processes.

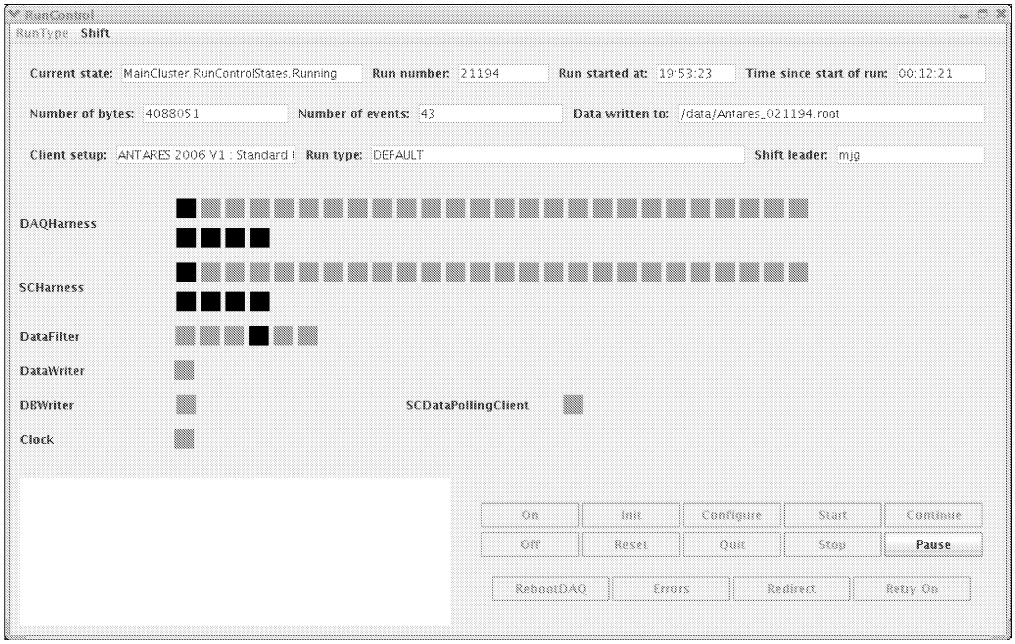


**Figure 2.18:** View of RunControl running in the shore station pc. Icons of the clients associated can be seen. Each square represents one LCM (storey), where green color means ON state. Either Line 1 and MILOM are both represented.

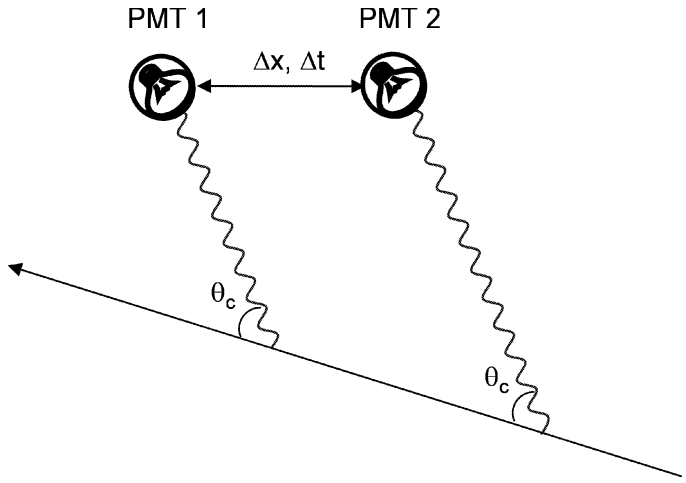


**Figure 2.19:** Sketch of two OM where the light from direct Cherenkov photons arrives causally connected.

### The software filtering system

Because of the high rate of bioluminiscense and $^{40}$K decays (70 kHz per PMT[9]), the volume of data produced in ANTARES is too large. Therefore, a filtering system based on space-time correlations is needed in order to reject the background from the ANTARES physics signals.

Although some trigger requirements can be implemented on-line, for the time being all raw data is processed on shore by the software algorithm, which is called the datafilter program, and works as a standard hardware trigger system.

The filtering is done following the next trigger levels:

Hits crossing the mandatory L0 threshold in the ARS are tagged as accepted L1 hits if they satisfy any of the following requirements: they are hits with high charge, i.e., 2 photoelectrons or more, or they have been detected by more than 1 PMT in the same storey within a time window of 20 ns (local coincidences). The next trigger level (called L2) searches for hits on different storeys which are causally connected (see Figure 2.19). The causality requires that two hits recorded with a time difference of $|\Delta t|$ in two different OMs separated a distance $|\Delta x|$ satisfy the relation:

$$|\Delta t| < \frac{1}{c_0/n} |\Delta x| \tag{2.15}$$

where $c_0$ is the speed of light in the vacuum, and $n$ is the refractive index of the water. This is because the muon induces Cherenkov light, and therefore, its velocity has to be greater than $c_0/n$.

[9]the rate depends on the L0 threshold, for instance L0 = 0.3 p.e. gives 60 kHz rate, and L0 = 1 p.e. gives 30 KHz rate.

After L2 trigger is performed, a *cluster* with all the causally connected hits from one root hit is formed. If this cluster satisfies some requirements as a minimun number of hits or a minimun number of storeys involved, it is considered as an *event*.

The aim of the following trigger level (L3) is to find more hits produced by physics signals that were not included previously in the cluster. To this end, a wider time window called *snapshot* is considered. This snapshot takes the time limits from the actual cluster, and expands the time window to a value about 2.2 $\mu$s, since this is the maximum casual time of an event inside the detector diameter ($\sim$ 500 m).

This process is done for all the events. The L3 trigger also takes care of merging overlapping events. Two events overlaps if the cluster of one event falls in time with the snapshot of another event. The result of two or more merged events is a single cluster with a redefined snapshot. In the L4 trigger level, all the hits within the snapshot of every event, are saved forming a PhysicsEvent following the ANTARES data format.

## 2.5 The ANTARES Monte Carlo simulation

In all the experiments, simulation data by Monte Carlo is necessary in order to understand the performance of the detector and the physics processes involved. The ANTARES event simulation chain is done mainly in three steps:

- **Generation of physics signals:**

  Two kind of possible physical signals can be recorded in ANTARES. On the one hand, the down-going events produced by atmospheric muons and, on the other hand, the up-going events produced by either atmospheric or cosmic neutrinos. The **atmospheric muons** appear as products of hadronic showers produced after a primary cosmic ray interaction in the atmosphere. These events are simulated by the CORSIKA [53] and HEMAS [54] software packages in the 1 TeV up to 100 PeV energy range of the primary cosmic rays. The threshold of 1 TeV is necessary in order to produce muons sufficiently energetic to reach the detector at 2000 meters depth. The hadronic shower development is calculate with QGSJET [55] and DPMJET [56] for CORSIKA and HEMAS respectively. For the secondary muons produced above 500 GeV (with lower energies they can not reach the detector) the propagation is simulated using the MUSIC [57] and MUM [58] packages, where the main energy loss processes are considered.

  Recently, a package called MUPAGE [59] has been developed by the collaboration with the aim of generating single and multiple atmospheric muons in the range of vertical depths from 1.5 to 5 km water equivalent and zenith angles $\theta < 85^o$.

  The volume used to simulate Cherenkov light emission is a cylindrical "can" where the detector is embedded and with an extension of three attenuation lengths.

  The **neutrino events**, including all the flavours and charged and neutral current reactions, are simulated by the software package GENHEN [60]. The zenith

angle and the neutrino energy are selected from a given spectrum. Afterwards, the interaction vertex and the target nucleon are chosen. For a cascade event ($\nu_e$, $\nu_\tau$ in CC, or NC events), these vertices are only considered when they are placed inside the "can". However, some features are not taken into account as macroscopic ranges reachables from PeV $\tau$, or likely muonic decay in a $\nu_\tau$ CC interaction where a subsequent long range muon is emitted. Instead, for $\nu_\mu$ of a certain energy (track events), the volume considered is the one which is defined by the maximal muon range. With the vertex position and the target nucleon chosen, is LEPTO [61] the tool to reproduce the neutrino interaction, where CTEQ6 [62] structure functions are included in it. PHYTIA/JETSET [63] are the software for the hadronisation. Other packages used in generation are RSQ [64], used for quasi-elastic resonant events at energies below 100 GeV, and TAUOLA [65] which considers the $\tau$ polarization.

Finally, the propagation of the muon induced after the neutrino interaction is simulated using the MUSIC and MUM packages, as in the atmospheric muon case.

- **Tracking and Cherenkov light emission:**

  In this step, the tracking of the muons resulting from the physics generators, and which are able to arrive to the "can", are simulated by KM3 [66] and GEASIM [67]. For this purpose, water properties of the ANTARES site as absorption or scattering, are taken into account. Moreover, physics processes: energy losses, multiple scattering, radiative processes, hadronic interactions and Cherenkov emission are also included.

- **PMT response:**

  The Cherenkov photons produce "hits" in the PMTs. The number of photoelectrons produced is estimated following Poisson statistics. In order to compute the hit probability the factors considered are: wavelength dependent absorption length, quantum efficiency, transmission coefficient of the glass sphere and the angular response. The angular acceptance and the transit time spread (TTS) of the PMT, as well as the electronics involved are also considered in the Monte Carlo.

## 2.6 Event reconstruction

In a neutrino telescope the direction and energy of the cosmic neutrinos are the crucial parameters to be measured. These can be estimated since they are strongly correlated to the ones coming from the induced muon. The aim of the reconstruction methods is to compute the track and the muon energy. In this sense, the ANTARES collaboration has developed several reconstruction strategies.

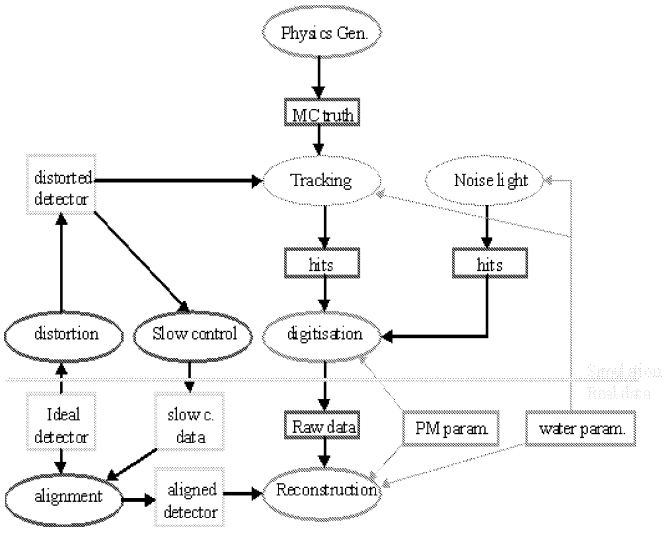


**Figure 2.20:** Scheme of the software programs involved in the ANTARES Monte Carlo simulation.

### 2.6.1 Track reconstruction

The ANTARES software package for track reconstruction is RECO [68] which includes the following reconstruction strategies.

- **Standard strategy:**

  This strategy uses the arrival time of the direct (non scattered) Cherenkov photons given by:

$$\tilde{t_i} = t_0 + \frac{1}{c}(L_i + r_i tan\theta_c) \tag{2.16}$$

  where the parameters defined are: $\tilde{t_i}$ which is the expected time of the direct Cherenkov photon coming from the track, $t_0$ is the time when the muon is in the reference position (arbitrary). This point has $(x_0, y_0)$ coordinates in the plane which is perpendicular to the muon track and contains the detector centre (see Figure 2.21). $L_i$ is the distance from the reference position to the closest point of the muon track to the OM, $r_i$ is the minimum distance between the muon track and the OM, and $\theta_C$ is the Cherenkov angle. The scattered photons, which arrive later than the direct ones, and the optical background, which arrive randomly, do not fit equation 2.16. Time differences between the expected time of the Cherenkov photon ($\tilde{t_i}$) and the actual time recorded in the OM, can be simulated by Monte Carlo. That provides a *pdf* which is useful to estimate the probability of

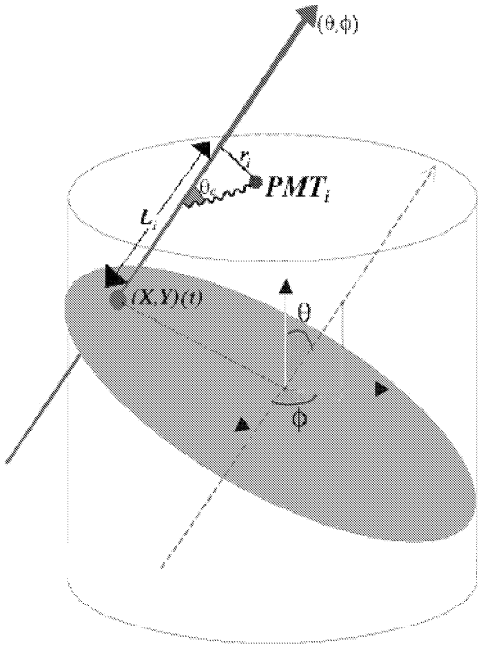


**Figure 2.21:** Schematic view of an event in the ANTARES neutrino telescope, where parameters for reconstruction are shown.

being direct Cherenkov photon for each hit. The maximization of the likelihood function built from the Monte Carlo *pdf* and the hit arrival times give the best muon track estimation.

- **Carmona strategy:** [85]

  The Carmona strategy as the first step a pre-fit based on the geometrical relation between the muon track and the direct hits, due to the fixed Cherenkov angle. Combining different hits in different OMs, the dependence on $t_0$ can be eliminated:

$$\Delta r_{ij} = \frac{c\Delta t_{ij} - \Delta L_{ij}}{tan\theta_c} \tag{2.17}$$

  Trying different combinations of three hits, an estimation of the track projection parameters ($x$,$y$) is obtained and afterwards, the whole track information reconstructed. This strategy improves the result of the fit by an iterative method.

- **Aart strategy:** [86]

  The Aart strategy uses a sequence of different fitting procedures in order to maximize the likelihood (as Standard strategy do). These fitting procedures are

linked together in such a way that each fit represents the input for the following fit. Except the first one which is a linear pre-fit.

Both Carmona and Aart strategies have meant an important improvement with respect to the Standard strategy.

- **Single line strategy:**

  This strategy is conceived to work with only one line. The aim is to deal with vertical or low energy events that only illuminates one line.

### 2.6.2 Energy reconstruction

The neutrino energy reconstruction in ANTARES is based on the energy reconstruction of the induced muon. The muon energy is estimated from the muon energy losses when crosses the matter surrounding the detector (see section 2.1.2). However, due to the detector finite volume, events not completely contained are frequent, which makes difficult a good energy estimation. For ANTARES, the $\log_{10} E^{\mu}_{rec}/E^{\mu}_{gen}$ distribution gives a mean value around 0, and a sigma value about 0.3 in the energy range from 500 GeV to 1 PeV. That implies a knowledge of the muon energy within a factor 2-3 [87].

## 2.7 The ANTARES performances

- **Angular resolution:**

  One of the most important features of a neutrino telescope is its angular resolution. In ANTARES, the angular resolution of the event is defined as the deviation between the actual muon track and the reconstructed track. A good angular resolution is very important in order to point-back to the cosmic neutrino sources. However, we have also to take into account the angle between the neutrino and the induced muon, as well as the deviation of the direction due to multiple scattering. The excellent water properties of the ANTARES site, together with the expected detector resolution (timing calibration, positioning, electronics, etc.), provide an angular resolution better than $0.3^o$ for neutrino events with $E_\nu > 10$ TeV, as can be seen in the Figure 2.22.

- **Effective area:**

  The effective area is defined as the equivalent surface, perpendicular to the incident particle beam, which is is 100 % efficient and is crossed by the same number of particles (muons or neutrinos) than in the detector. This effective area depends on the energy and the direction of the incident neutrino.

  The effective area for neutrinos is much smaller than the muon effective area due to the small neutrino cross-section. This cross-section increases with the energy

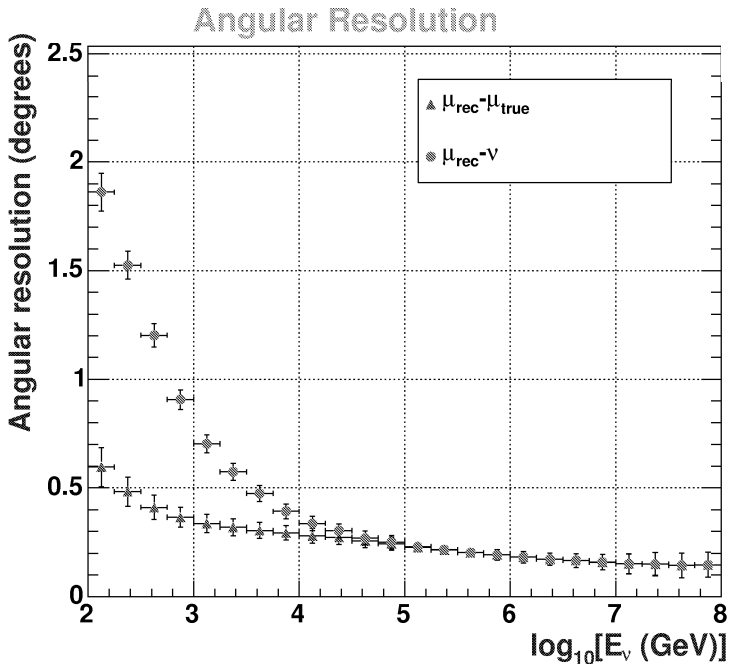


**Figure 2.22:** Angular resolution of the ANTARES neutrino telescope for simulated events after strict reconstruction quality cuts. Below 10 TeV, the angular resolution is dominated by kinematic angle ($\theta_{\nu\mu}$). Above 10 TeV, is dominated by reconstruction (calibration, electronics, etc.).

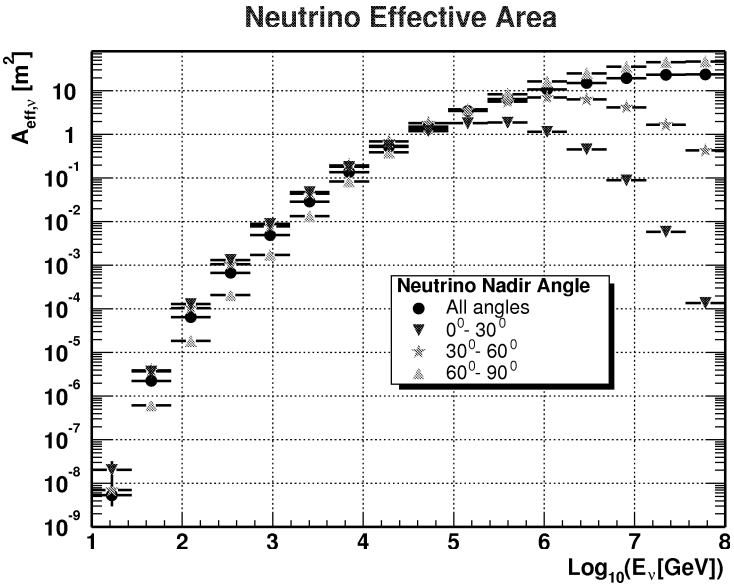


**Figure 2.23:** Neutrino effective area as a function of the neutrino energy, using the Carmona strategy. The Earth opacity effect can be noticed.

and becomes important for energies greater than 10 PeV. Above this energy, neutrinos crossing the Earth at a nadir angle of $0^o$ will probably interact during its travel, because of the long path through the Earth. Obviously, this path becomes shorter when the incident angle is close to the horizon. Therefore, an effect of opacity appears depending on the angle. Neutrino events with very high energies are thus expected for angles close to the horizon.

In the Figure 2.23, the neutrino effective area is shown. A distinction is made on the basis of the angle between the reconstructed neutrino with respect to the incident neutrino.

- **Source detection:**

  The main aim of neutrino telescopes is to point-back to extraterrestrial sources. In this sense, ANTARES will observe $3\pi$ sr of the sky, with the Galactic Centre 2/3 of the time being observable. ANTARES will complement the observations of AMANDA and the future IceCube which are devoted to cover the northern sky. Both experiments will overlap in a 0.6 $\pi$ sr region of the sky (1.5 $\pi$ sr without time constraint). However, as it has been commented in the previous chapter, in a detector with the ANTARES dimensions, it is not expected to find clusters from point-like sources. Therefore, the detection of unresolved cosmic sources (diffuse fluxes) will be also a test to prove the existence of high energy extragalactic neutrinos. The sensitivity of ANTARES to diffuse fluxes and point-like sources is shown in the Figure 2.24

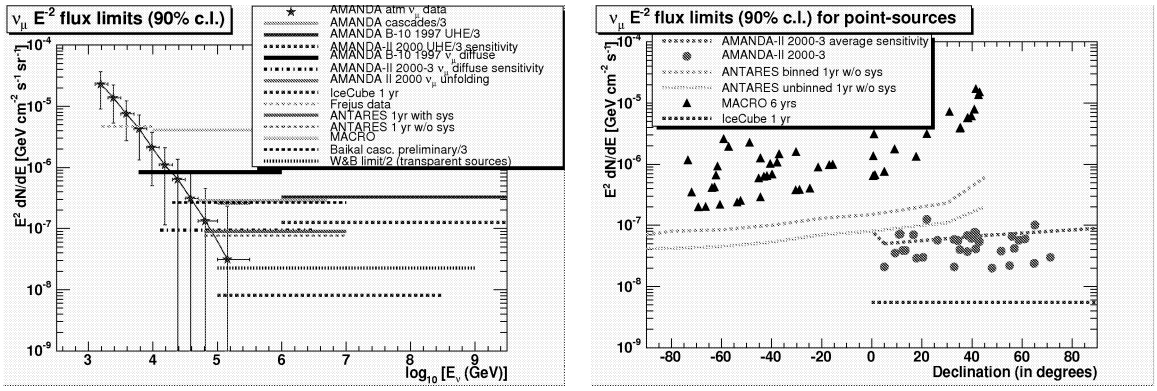


**Figure 2.24:** Sensitivity for diffuse fluxes in different experiments(left side), and sensitivity for point-like sources (right side).

## 2.8 Status of the project

The ANTARES collaboration has recently achieved one of the major steps with the "Line 1" deployment and connection, on March 2006. That means the starting point of the construction and deployment of the final detector that will be completely installed by the end of 2007, and will be followed by several years of operation for science. This is the result of many efforts carried out during the time period of site exploration, research and development tasks between 1996 and 1999.

After this period, different prototype lines as the PSL (Prototype Sector Line, December 2002), the MIL (Mini Instrumentation Line, February 2003), the Line 0 (mechanical test line, March 2005), the MILOM (Mini Instrumentation Line with Optical Modules, April 2005), and finally the Line 1 have showed and proved the feasibility of a neutrino telescope in the ANTARES site. Apart from Line 1, another line (Line 2) is already deployed an ready for the connection with the junction box. The time schedule of the experiment foresees that 2 more lines will be deployed and connected during 2006. This research work will focus on the results of the integration and the analysis of real data taken with the MILOM line (Figure 2.25).

## 2.9 Overview of other neutrino telescopes

Apart from ANTARES, several projects are nowadays (or have been) working in the development of neutrino astronomy. In this section, a summary of their current status will be exposed.

- **DUMAND:**

  The DUMAND (Deep Underwater Muon and Neutrino Detection) [69] collaboration was the pioneering project in neutrino telescopes. They aimed for the

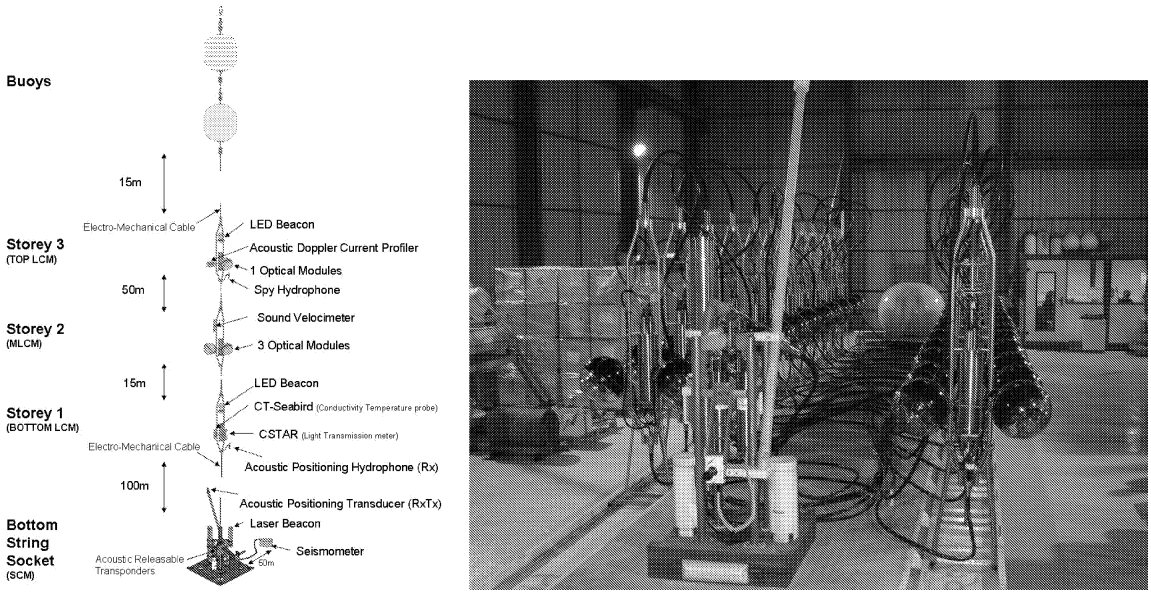


**Figure 2.25:** Schematic view of the MILOM line which is composed by 3 storeys with several instruments (left side). Picture of the ANTARES Line 1 ready for deployment (right side).

deployment of a neutrino detector close to Hawai coast. This project lasted from 1976 until 1995 when the US department of energy cancelled its support. In its active time period, many studies developing appropriate technology, were carried out.

- **BAIKAL:**

  The Baikal collaboration [70] has been the first neutrino telescope actually working. Constructed under lake Baikal (Rusia) at 1100 meters depth, has had several stages in its construction. Since April 1993 to March 1995, a first stage (NT 36) with 36 optical modules were operating. Afterwards, its infrastructure was increased to 192 optical modules (NT 200) and was operating 5 years (1998-2003). Finally, in the most recent stage, 3 additional outer strings, has been deployed (NT 200+) in spring 2005. With its detector, the Baikal collaboration has reconstructed upward muons coming from atmospherical neutrinos, and has put limits on the neutrino diffuse fluxes.

- **AMANDA:**

  The Antarctic Muon and Neutrino Detector Array (AMANDA) [71] collaboration has constructed a neutrino telescope in the South Pole. In this detector, the propagation medium for the muon induced in the neutrino interaction is ice. The main advantages of ice comparing to water are that the ice has lower levels

of background radiation (there is neither bioluminiscense nor $K^{40}$) and a longer attenuation length, which gives better shower events reconstruction. However, the light is more scattered than in water, therefore, a poorer angular resolution is expected.

AMANDA started in 1993 with its first test modules deployment and is still in steady operation, although the collaboration is nowadays focussed on data analysis and the construction of the future IceCube detector.

The detector has had several stages, the last one (AMANDA-II) was composed by 677 optical modules distributed on 19 strings at a depth between 1500 and 2000 meters inside the ice.

They have presented results about limits on neutrino fluxes [72]. The more recent (still preliminary) give limits on diffuse $\nu_\mu$ fluxes of:

$$E_\nu^2 dN_\nu/dE_\nu = 8.9 \times 10^{-8}\ \mathrm{GeVcm^{-2}s^{-1}sr^{-1}} \quad \text{for } 16\ \mathrm{TeV} < E_\nu < 2 \times 10^3\ \mathrm{TeV} \tag{2.18}$$

And considering all flavours:

$$E_\nu^2 dN_\nu/dE_\nu = 3.8{\times}10^{-7}\ \mathrm{GeVcm^{-2}s^{-1}sr^{-1}} \quad \text{for } 1.8{\times}10^2\ \mathrm{TeV} < E_\nu < 1.8{\times}10^6\ \mathrm{TeV} \tag{2.19}$$

where a $E^{-2}$ energy spectrum due to schock acceleration and a 1:1:1 flavour ratio due to neutrino oscillations, were assumed.

In their results (Figure 2.26), no clear point-like sources have been seen in 807 days of data taking. All the source candidates give events compatibles with the background. The most significant excess is from the Crab nebulae where 10 events has been detected comparing with and expected background of 5.4 events.

The flux limit obtained in point like sources is:

$$E_\nu^2 dN_\nu/dE_\nu = 6 \times 10^{-8}\ \mathrm{GeVcm^{-2}s^{-1}sr^{-1}} \tag{2.20}$$

- **IceCube:**

  The IceCube detector [73] means the natural enhancement of the AMANDA detector up to 1 $km^2$ scale (Figure 2.25).

  Nowadays, the collaboration has deployed a total of 9 strings out of 80 of the schedule. Each string contains 60 modules with a 17 meters separation containing 10" PMTs, so 4800 PMTs will compose the whole detector which is expected to be finished by 2011. The first results have been alreday presented [74].

  The sensitivity expected for diffuse fluxes is:

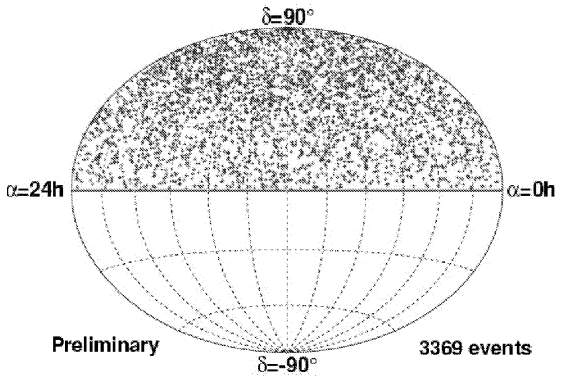


**Figure 2.26:** Sky map in equatorial coordinates, with 3369 up-going events recorded by AMANDA during 2000-2003 operation.

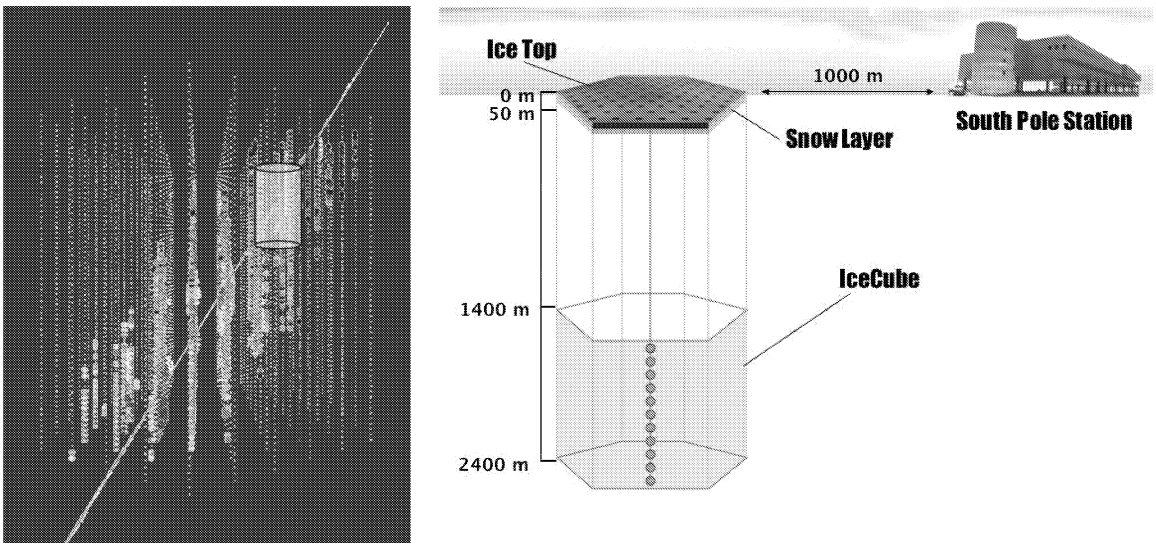


**Figure 2.27:** Event simulation in IceCube detector. AMANDA is drawn as a yellow cylinder (left side). Sketch of the IceCube detector (right side)

$$E_\nu^2 dN_\nu/dE_\nu = 3 - 12 \times 10^{-9}\ \mathrm{GeVcm^{-2}s^{-1}sr^{-1}} \tag{2.21}$$

and for point-like sources:

$$E_\nu^2 dN_\nu/dE_\nu = 5 \times 10^{-9}\ \mathrm{GeVcm^{-2}s^{-1}sr^{-1}} \tag{2.22}$$

- **NESTOR:**

  The NESTOR (Neutrino Extended Submarine Telescope with Oceanographic Research) [75] collaboration is constructing a neutrino telescope at 3800 m depth, in the Ionian Sea, off the coast of Pylos (Southwestern Greece). The basic element of the NESTOR detector is a hexagonal star-like floor with 32 m of nominal diameter. Two optical modules are attached at the end of each arm, one facing upward and the other downwards. A full NESTOR tower would consist of 12 of such floors stacked vertically with a spacing of 30 m between floors. Site evaluation has been done with studies about bioluminescence and water quality. Transmission lengths of $55 \pm 10$ m at a wavelength of 460 nm, stable temperatures of 14.2 ℃ and water current velocities well below 10 cm/s has been obtained. Finally, the feasibility of the project has been showed with the deployment in 2003 of a reduced size single floor [76].

- **NEMO:**

  The NEMO (NEutrino Mediterranean Observatory) [77] aims to construct a $\mathrm{km}^3$ detector in the Mediterranean sea. After an extended research of several promising sites, an optimal location was selected at about 80 km off in the Ionian sea close to Catania coast (East of Sicily) at a depth of 3500 m. The current design foresees 81 towers, spaced so that the whole apparatus covers a surface larger than 1 $\mathrm{km}^2$, and connected by means of 10 junction boxes. The total number of photomultipliers will not exceed 6000. Each tower will have a tetrahedral structure, sustaining succesive arms orthogonally to each other, separated vertically by 40 m and carrying 2 pairs of PMTs looking upward and downward. Recently, the collaboration has deployed a prototype at 2000 m depth, in order to implement a reduced-scale demonstrator of the apparatus.

- **KM3NeT:**

  KM3NeT [78] is devised to be a $\mathrm{km}^3$ neutrino telescope, in the Northern hemisphere, in order to complement IceCube in the task of covering all the sky. This collaboration will be formed mainly by the institutes nowadays working in NEMO, NESTOR and ANTARES. KM3NeT is currently at the Design Study stage which will be finished by January 2009. According to the schedule, the installation is foreseen between 2010 and 2012, with the data taking beginning

by 2011. The most important performance goals for this detector are the achievement of an angular resolution for muon events better than $0.1^o$ for neutrino energies exceeding 10 TeV, an energy threshold of a few 100 GeV and a sensitivity to neutrinos of all flavours and to neutral-current reactions. These features would provide a great step towards the understanding of the Universe and would allow us to solve questions that currently 0.1 $km^2$-scale telescopes are not foreseen to do.

# Chapter 3

# The ANTARES time calibration and the Optical Beacon System.

## 3.1 Introduction

Track reconstruction in ANTARES relies basically on the arrival times of Cherenkov photons to the optical modules, therefore, the time calibration of the detector is of the utmost importance. The relative timing resolution between OMs is closely related to the pointing accuracy of the telescope. An angular resolution for muon tracks of $0.3^{\circ}$($E_{\nu}$>10 TeV) would require a high level of precision in the timing resolution.

The main contributions to the uncertainties in the relative timing comes from the transit time spread (TTS) of the signal in the photomultipliers ($\sim$1.3 ns) and the optical properties of the sea water such as light scattering and chromatic dispersion ($\sim$1.5 ns for 40 m distances).

Therefore, all electronics and calibration systems are required to contribute less than 0.5 ns to the averall timing resolution to guarantee the expected angular resolution.

Considering the absolute timing calibration, the purpose is to fix an specific time for our neutrino event with respect to the universal time. An acuracy of 1 ms is enough in ANTARES for any conceivable physics goal as gamma ray bursts, flares or supernova explosions. In this way, the detector would be able to distinguish neutrinos coming from an object with a diameter of 300 km. The main uncertainties in the absolute timing comes from the cables of the system (cable interconnecting the lines with the JB, the 40 km electro-optical cable, etc).

## 3.2 Time calibration systems

Several calibration and monitoring systems are devised for ANTARES time calibration which according to the place where they will be finally performed, can be classified in: "in situ" calibration systems and on shore calibration systems.

### 3.2.1 In-situ calibration systems

These are the time calibration systems that will operate in the sea. Some of the measurements and tests performed by these systems will be redundant with respect to those performed on-shore. However, the different environmental conditions in water can change the expected values of the calibration parameters already measured in the laboratory.

The in situ systems and methods are: Clock calibration, the internal LED calibration, calibration with Optical Beacons and calibration with atmospheric muons.

- **The internal clock calibration:**

  The clock calibration system is based on an echo method where the 20 MHz clock is generated on-shore and distributed afterwards throughout the detector. This clock provides a common reference to all the LCMs. The idea is to get the round-trip time from the delay between the moment when the signal is sent and the moment when the answer arrives. The half of this round-trip time for each LCM, gives the clock-phase which allows the LCM to be synchronized with a time precision around 100 picoseconds. Another feature of this system is the synchronization with respect to the Universal Time by assigning the GPS time to the data.

- **Calibration with internal LEDs:**

  As we saw in the OM description, every OM has an internal blue LED ($\sim 470$ nm) for calibration purposes. This LED is glued on the back of the PMT to illuminate, pulsed by the clock, the photocathode from the inside (See Figure 2.9). The aim of this test is the monitoring of the transit time (TT) of the PMTs. This is done by flashing the internal LED at a rate of about 100 Hz and comparing the OM arrival time signal with respect to the LED flash time emission. Figure 3.1 shows the results of the internal LED runs from the instrumentation line, MILOM, with the line already in the sea for a time period of six months.

- **The Optical Beacons:**

  The Optical Beacons, LED and Laser (Figure 3.2), are devices which emit light pulses through the water and allow us to illuminate the OMs with a good knowledge of the reference light emission time. They provide a common light source to all the OMs, therefore the relative time off-sets among OMs can be estimated in the same way as has been done in the dark room with the laser system. In addition, spacial calibration cross-checks and studies of the light transmission in water can also be performed. A more detailed description of this calibration system will be given in section 3.3.

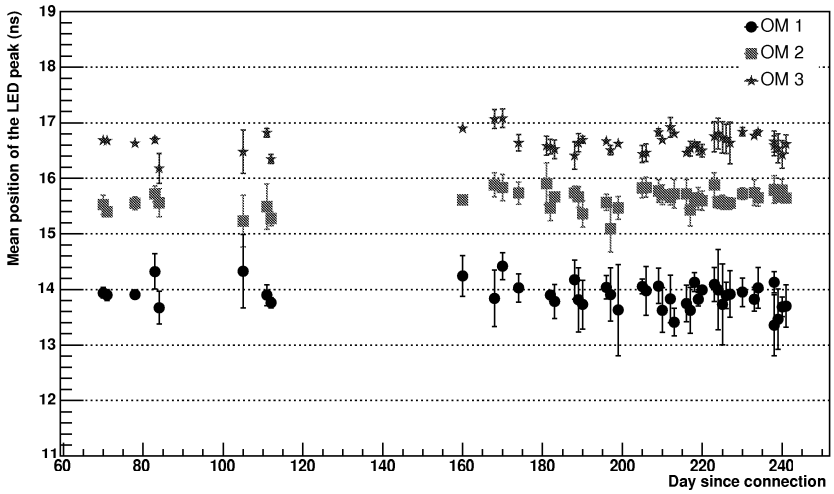


**Figure 3.1:** Arrival time of the OM signal induced by the internal LED flash with respect to the flash time emission. Results taken with the MILOM line once in the sea, during six months of data taking.

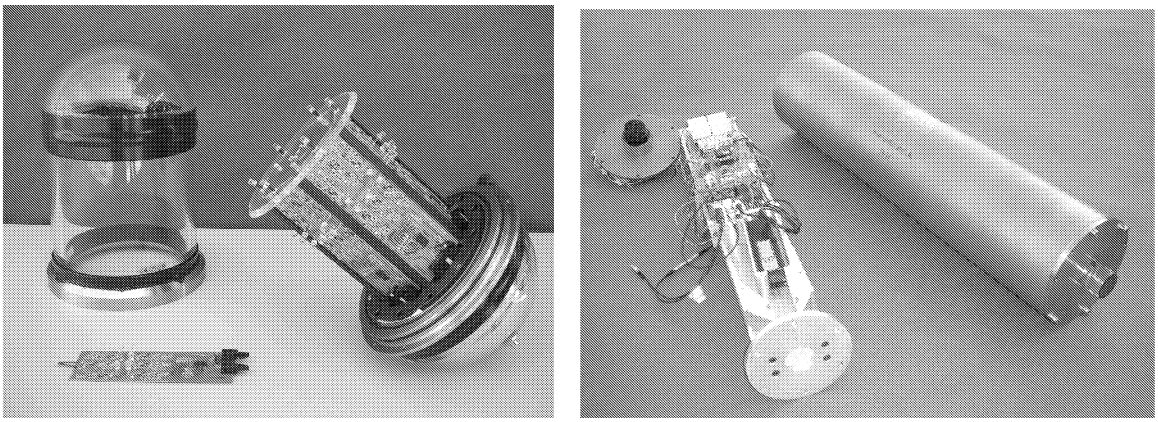

**Figure 3.2:** The ANTARES Optical Beacons with their containers. In the left side the LED Beacon, and in the right side the Laser Beacon.

- **Calibration with atmospheric muons:**

  The relative time off-sets can also been monitored using the ∼10000 down-ward atmospheric muons per day, expected in the ANTARES detector. The distributions of the time residuals[1] of the hits will be used as a monitorization system which will show whether the off-sets used in the reconstruction are accurate enough.

### 3.2.2 On-shore calibration system

The on-shore calibration systems are necessary in order to check that all the detector components work correctly before the line deployment under the sea. Moreover, they allow us to obtain the first set of calibration parameters which will be compared with the one obtained in-situ. Most of the these measurements are performed in a special dark room built on purpose for the ANTARES calibration and located at CPPM.

A laser system providing a common light signal by fibre optic to every OM is used in the dark room. The light, coming from the laser, is divided by a 1-to-16 optical splitter in order to illuminate the OMs of every sector (15 OMs). The end of the fibre is attached to a kind of flower pot which encloses the OM (Figure 3.3). Inside the flower pot, a diffuser spreads the light before illuminating the PMT photocathode. The laser is similar to the one used in the laser optical beacon (see section 3.3.2). It emits short and very intense (∼1 $\mu$J) pulses of green light ($\lambda = 532$ nm), so that it provides $\sim 10^{12}$ photoelectrons. Several tests and measurements are done with this system:

- **Time off-sets measurements:**

  The aim of this test is to compute the relative time off-sets among the OMs of the detector which appear when an external synchronous signal flashes them simultaneously. In other words, to assess the time differences resulting from differences in the transit time and the electronics of each OM.

  In order to measure the differences of the time response of each OM, a reference time synchronous with the laser light emission is needed. This reference signal is provided by a photodiode internal to the laser which is read by an independent LCM_ref exclusively built for the dark room calibration tests.

  The time off-set of the LED Beacon PMT is also calculated with this system. However, due to its small photocathode area, a dedicated fibre without passing through the splitter is used in order to avoid light attenuation. In addition, at the end of the fibre there is a focussing lens which avoid the light dispersion.

  The time difference between the OM signal and the LCM_ref signal gives the time off-sets between OMs, after removing the fibre length path and the clock-phase. The fibre length path introduces a delay that has to be taken into account. In addition, because the fibres have not exactly the same length, a specific correction

[1] difference in time between the measured time and the time expected from the track fit.

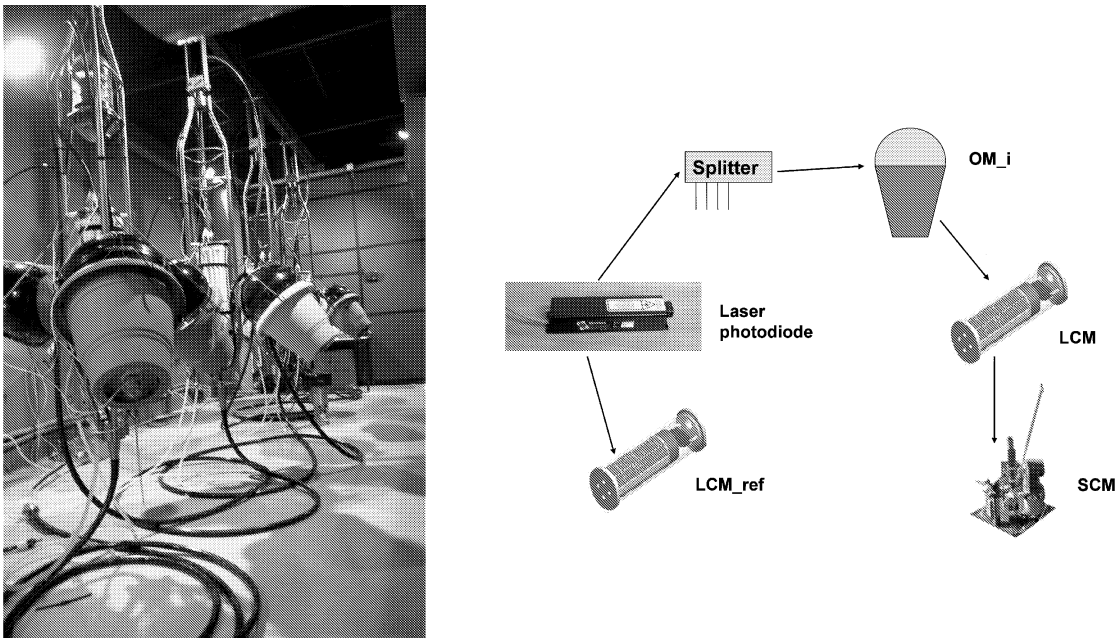


**Figure 3.3:** General view of the laser system at the dark room (left side) and the laser by fibre optics sketch (right side).

has to be done. This effect is computed taking one OM as reference and swapping its fibre with the rest of the OMs. The clock-phase is the time delay introduced when the information travels from a specific LCM to the SCM of the line. All the clock-phase delays are computed previously to the laser tests in the clock calibration test. In order to establish a common reference, this clock-phase is subtracted to the hit time. Therefore, the formula to compute the time off-set ($\Delta$t) for the ARS "i" is:

$$\Delta t = [\mathrm{t_{LCMref}} - (\mathrm{t_{ARS\_i}} + \mathrm{clockphase_{LCM}})] \tag{3.1}$$

where the different fibre lengths have been previously corrected. Usually, the values for a specific line are referred to an ARS of a certain OM (ARS_0 OM_0).

An important effect to consider in the $\Delta$t computation is the walk-effect, i.e., the effect of the different charged signals in time measurement. Two signals produced at the same time, are recorded at different times because the most charged one crosses the L0 threshold first and gives an earlier time (Figure 3.4). This effect is corrected before the final time off-set values are stored in the database.

- **TVC calibration:**

  Moreover, another calibration that it is made is the **TVC calibration**. This calibration is important because the TVC behaviour is not perfect and can affect the time resolution. In principle, the TVC has a dynamic range from 0 to 255

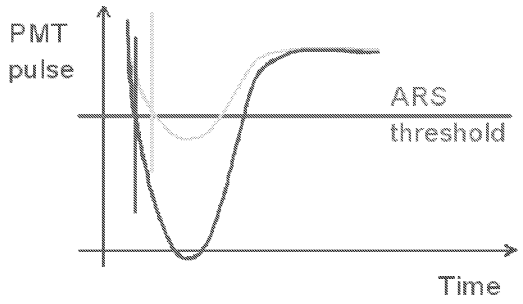


**Figure 3.4:** The walk-effect. Two signals arriving at the same time but with different charge, give different time measurements.

(see section 2.4.1), but in the real world this range is reduced. The range is redefined by a $TVC_{min}$ and a $TVC_{max}$ values, in principle different for both TVCs in each ARS. The laser signal is very useful to compute this new limits because its time jitter between the trigger and its actual light emission is about hundreds of nanoseconds. Therefore, the signals are seen as randomly distributed in the 50 ns range of the TVC, and a flat distribution is obtained. The values for $TVC_{min}$ and $TVC_{max}$ are defined, respectively, as the first bin and the last bin where the number of entries exceeds a 10% the average number of entries in the flat distribution. After this computation, the TVC is considered linear between these new limits.

Nevertheless, the TVC is not exactly linear in the $TVC_{min}$ and $TVC_{max}$ range due to the differential non linearities (DNL) of the ADC. That means different size among channels, and consequently, different ocupancy among channels, as can be seen in the TVC distribution obtained in a laser run at the dark room in the Figure 3.5. Analysis carried out about the influence of the DNL [79] show that improvements in the relative time accuracy up to 80 ps, can be attained if DNL are taken into account.

- **ARS threshold:**

  An **ARS threshold** test is also made in the dark room using the laser system. This test aims to measure the discriminator threshold (L0) response computing the efficiency curve (S-curve) for different levels of the input signal (0, 1, 1.5 p.e.). This allow us to know the equivalence between the L0 trigger units and mV (p.e.).

- **Charge calibration:**

  Another test done in the dark room is the **charge calibration** test, where the values of AVC_0 (pedestal) and AVC_1 (1 p.e.) are computed. These points are necessary to convert AVC values into mV (see section 2.4.1). The methodology

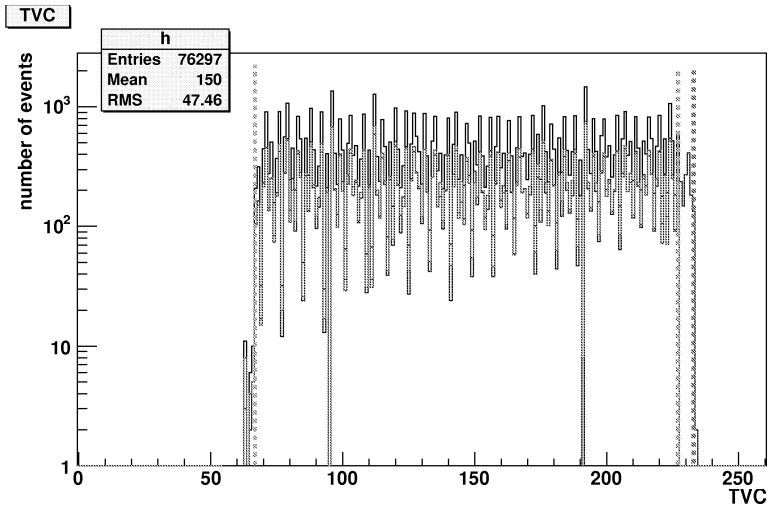


**Figure 3.5:** Example of a TVC flat distribution in logarithm scale for a particular ARS. Both TVCs can be studied separately (blue and red). The dashed lines show the $TVC_{min}$ and $TVC_{max}$ limits. The DNL effect produces the low occupancy channels.

of this test is similar to the one performed in the ARS threshold test, i.e., tunning the input laser signal.

Both the ARS threshold and the charge calibration tests, are redundant with the previous ARS qualification tests, and they will be repeated afterwards with the line in the sea, using background signals in dedicated runs.

## 3.3 The Optical Beacon system

Since this research work will be focussed on the tests performed with the Optical Beacon system for the instrumentation line (MILOM) and the Line 1, we present in this section a more detailed description of this time calibration system.

### 3.3.1 The LED Beacons

Each LED Beacon contains 36 individual LEDs arranged in groups of six on six vertical boards (*faces*) which are placed side by side forming an hexagonal cylinder. On each face, one LED points upward (*top* LED) to illuminate the higher storeys above in the same string and the other five radially outward to illuminate the nearby strings. One of the LEDs pointing outward is located in the middle of the face (*central LED*) and the remaining four surround it.

The pulser circuit is based on an original design from Kapustinsky et al. [80]. It is feeded with +48V which provides a variable DC power supply between 0 and +24 V in order to adjust the light intensity of the LED. This LED flashes in response to

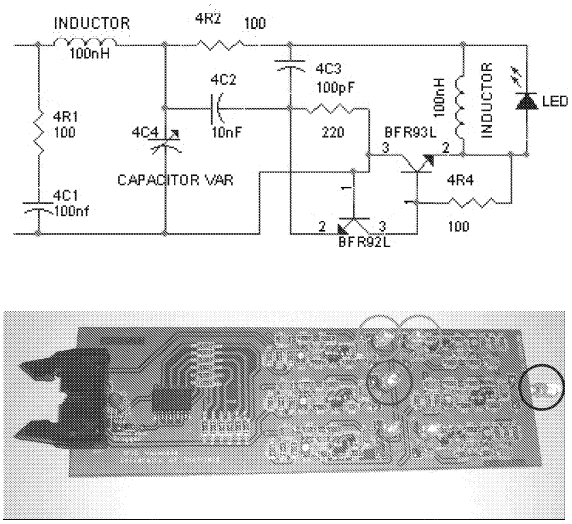


**Figure 3.6:** Diagram of the Kapustinsky pulser after the ANTARES modification (top). One face with the 3 LED groups highlighted. Blue *top*, red *central* and green *four* (bottom).

the positive-going edge of the trigger pulse provided by the internal ARS clock at a tipical frequency of 30 Hz. This design has been modified in ANTARES to include a variable capacitor that allows the synchronization of the emission time of the pulses of the different LEDs in the same or in different faces. A sketch of the pulser is showed in the Figure 3.6.

The LEDs used in the beacons has been selected among several models tested by the ANTARES collaboration in terms of amplitude and risetime of the emitted light pulses. Finally, the Agilent HLMP-CB15-RSC00 model was chosen for the final design.

These LEDs, emit blue light of 472 nm with a spectral half-width of 35 nm. Each flash gives an output of typically 158 pJ, working at maximum intensity (+24 V), which corresponds to $3.7 \times 10^8$ photons per pulse. The main feature of this light pulse is that its rising edge is very sharp ($\sim$ 2ns), as is required for relative timing calibration.

The 6 faces which constitute the beacon are mounted on a nylon structure which houses inside a small Hamamatsu H6780-03 photomultiplier (Figure 3.7). This PMT has a rise-time of 0.78 ns and a transit time of 5.4 ns, and its voltage feeding, which controls the gain, is tunable. A flat acrylic disc, that acts as a lightguide, is fixed to the upper part of the nylon mounting to increase the collection of light. The photomultiplier is mounted centrally on this disc under a polished conical indentation which directs light onto the photocathode. The aim of this small PMT is to provide the reference time emission of the light flash from the LED Beacon.

Once mounted, the whole beacon is housed inside a borosilicate glass container which protects their components from the sea high pressures. This is a cylindrical

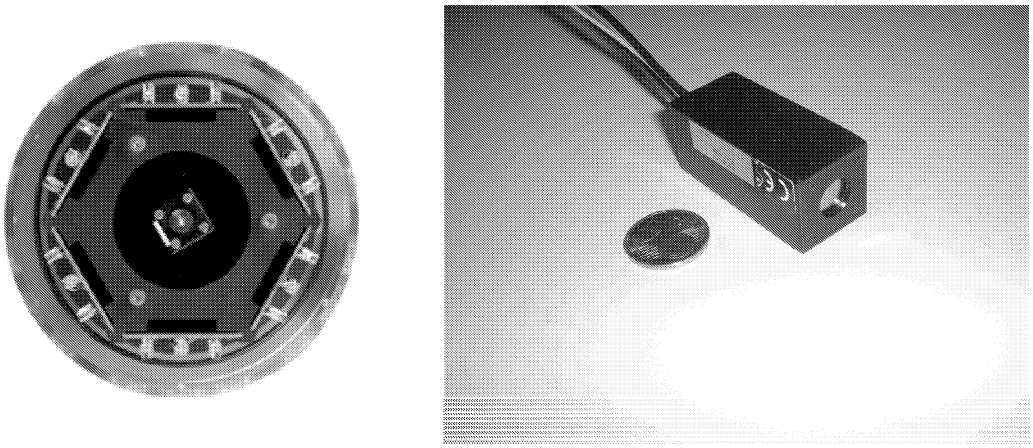

**Figure 3.7:** The LED Beacon seen in a front view. The transparent plastic with the small PMT is visible (left side). The H6780-03 Hamamatsu PMT (right side).

borosilicate glass container comercially available[2]. It consists of a cylinder and two endcaps, one of them detachable. All the parts are in transparent glass except the titanium flanges that enable to hold them together. The overall dimensions of the cylinder plus endcaps are 210 mm outer diameter and 443 mm in length. The endcap is supplied with a 22 mm diameter pre-drilled hole equipped with a penetrator on the outside of the cylinder and connecting cables in the inside. The LED Beacon is attached to the detector strings by a collar in the Optical Module Frame (OMF). It is held vertically at a dedicated location above the triplet of OMs and fixed to the structure combining the 6-fold symmetry of the beacon and the 3-fold symmetry of the OMF so as to minimize shielding (Figure 3.8).

Four LED Beacons are located along every line in storeys 2, 9, 15 and 21. With the LED Beacon features, we can illuminate at different intensities with known directions, for blue light which is the more efficient wavelength for the ANTARES PMTs. In order to enlarge the angle of light emission, the LED caps are clipped off before being mounted on the pulser circuits.

The LED Beacon is controlled by the motherboard located in the lower part of the beacon. The motherboar contains the electronics that provides the required operating voltages and enables the actual LED flashing according to externally supplied commands. The motherboard allows: 1) to set the DC level supplied to the LEDs and thus the intensity of the light pulses emitted, 2) to select the faces or group of faces requested to flash, 3) to select any of the three groups of LEDs or the combination thereof to flash in all faces, 4) to set the PMT feeding voltage and thus its gain and 5) to monitor the voltage applied to the LEDs and the temperature as measured by a sensor installed on it.

[2]Nautilus Marine Service GmbH, Blumenthalstrasse 15 D-28209 Bremen Germany

**Figure 3.8:** The Optical Module Frame with one LED Beacon (left side). The LED Beacon borosilicate glass container (right side).

Each of the six faces can be flash independently or in combination with the others. Within a face the top, central and group-of-four LEDs (see Figure 3.6 bottom) can be triggered independently or in combination. This layout allows a distribution close to uniform in the azimuth angle when all the faces are emitting. Therefore, this provides a lot of possible combinations to illuminate with the LED Beacon.

The configuration of all the LED Beacons in the detector is performed through the general RunControl program [88]. The configuration, i.e. the set of possible faces and group of LEDs requested to be flashed and the required PMT and LED voltages, are stored in a database. At the configuration stage of the start of a calibration run a given configuration (a *run set-up*) can then be selected. In addition, a graphical user interface, written in java, allows the expert user to communicate directly with the beacons and charge their configuration during the run generating the necessary ControlHost commands. This method is very rarely used during normal data taking, but is employed in the laboratory for test or debugging purposes.

The first results (obtained in the MILOM and the Line 1) have shown that the LED Beacons are crucial to do cross-checks of the time off-sets measurements made previously in the dark room. They will also allow us to study how the optical properties of the water (scattering, absorption, etc.) can affect our measurements.

### 3.3.2 The Laser Beacon

The second type of optical beacon is the Laser Beacon. Its main component is a diode pumped Q-switched Nd-YAG laser provided by Nanolase (NG-10120-120 model) which emits green light at a wavelength of $\lambda$=532 nm and provides intense ($\sim$ 1 $\mu$J)

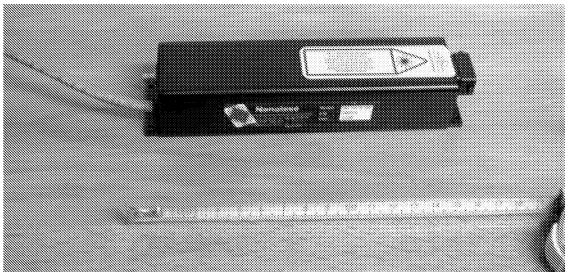

**Figure 3.9:** Picture of the Na-YAG laser provided by Nanolase.

and short (FWHM $\sim$ 0.8 ns) pulses (Figure 3.9).

The laser dimensions are 144 $\times$ 37.4 $\times$ 30 mm and within the laser head there is a fast built-in photodiode used to register the actual time of the laser light emission. The Laser Beacon is feeded with +48V which provides a fixed DC power of 12 V. For the flashing, it can be operated in a non-triggered mode at a fixed frequency (around 15 kHz) and in a triggered mode with a variable trigger frequency. In the triggered mode the laser flashes in response to the positive-going edge of the trigger pulse provided by the internal ARS clock. Since the laser is passively Q-switched, the time between the start signal and the light pulse emission is of the order of microseconds and the pulse to pulse fluctuation (jitter) is of the order of a few hundreds of nanoseconds.

Once the laser shot is produced, the built-in photodiode sends back a signal which is driven outside to the ARS located in the LCM. The built-in photodiode provides the laser time emission with an acurracy of $\sim$ 50 ps [81]. Since the time emission of the pulse can vary by a few hundreds of nanoseconds, we checked that the time recorded by the internal photodiode was accurate enough. Using a very fast external photodiode, the difference in the emission time given by the two photodiodes was measured. The standard deviation of the distribution of time difference was measured and the result was of the order of 50 ps, which is a precision far better than what is needed in our application.

A cylindrical titanium container protects the laser and the associated electronics from high pressures in the sea bed. The container have a length of 750 mm and 170 mm of diameter. Its bottom endcap holds the penetrator of the cable connectors. Inside the container, an aluminium inner frame holds the laser and its associated electronics.

For the time being, there is only one Laser Beacon placed at the BSS (anchor) of the instrumentation line (MILOM), however, is foreseen to deploy at least one more Laser Beacon in the future.

The laser is pointing upwards in order to illuminated as many as possible OMs. In order to minimize the effects of the fouling and sedimentation, the laser light emission takes place through the vertical walls of a quartz rod cylinder (Figure 3.10). Before going through the quartz rod, the light is spread out by an optical diffuser (ORIEL model 48010) disk 2.2 mm thick which provides a lambertian emission.

Due to the Snell's law, the cosine distribution is conserved when the light leaves

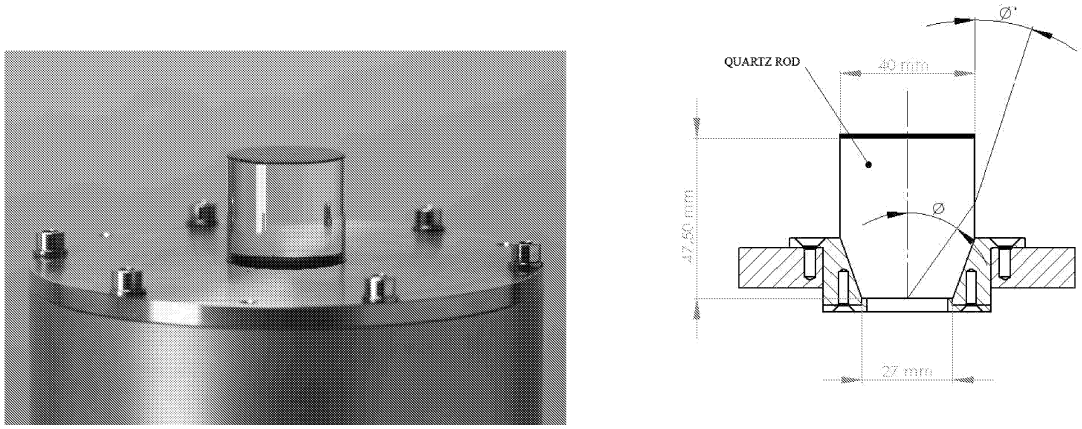


**Figure 3.10:** Picture of the borosilicate rod (left side). A design of the rod, where one posible output angle of the light ($\phi$') is represented (right side).

the cylinder through its vertical wall. The dimensions of the cylinder together with the refractive index of quartz ($n = 1.54$) determine the maximum and minimum angle of the outgoing light, which were chosen to be 40 mm in diameter and 47 mm in lenght (see Figure 3.10 right side). These dimensions were selected to so as to maximize the number of storeys illuminated in the closest strings, while taking into account the technical constraints of the cylinder fixing due to the high pressure.

The Laser Beacon light output, for the first beacon deployed, is not tunable. The Laser Beacon has the advantage of due to the narrow range of the wavelength involved, the chromatic dispersion effect is negligible. Moreover, because of its fixed and well-known position, the Laser Beacon can be also used to do cross-checks of the positioning system.

# Chapter 4

# Integration of the Optical Beacons

The ANTARES Optical Beacons have to pass a lot of strict and rigorous tests before being deployed in the sea bed. In this chapter, we will review the tests done, first in Valencia during the production phase and after, during the integration phase of the detector at CPPM. The experimental setups, the test benches and the procedures followed will be explained and some results will be presented.

## 4.1 Optical Beacon production tests at Valencia

The mounting and production of the Optical Beacons is done in the IFIC laboratory at Valencia. For each kind of Optical Beacons, a set of tests have been conceived in order to check its correct operation. In this section, we will describe these tests and analyze the results.

### 4.1.1 LED beacon tests

All the LED Beacon components described in Chapter 3 are assembled in Valencia. Once a LED Beacon is mounted, it has to overcome a series of tests before being introduced into its borosilicate glass container. The closing of the container is done following a special set of instructions to prevent possible damages due to the water pressure during the deployment of the line. Once the container is closed, a final functional test is done to check that the main operations of the beacon work properly. Only after this final check, the beacon is ready to be shipped to the integration site.

The LED Beacon tests performed at Valencia, in chronological order, are the following:

1. First of all, the LED beacon components: the motherboard card, the 6 faces, the 36 individual LEDs, the small Hamamatsu PMT and the mechanical support are visually inspected and properly checked, specially the motherboard card which is in charge of all the beacon operations, LED intensity, PMT gain, etc.

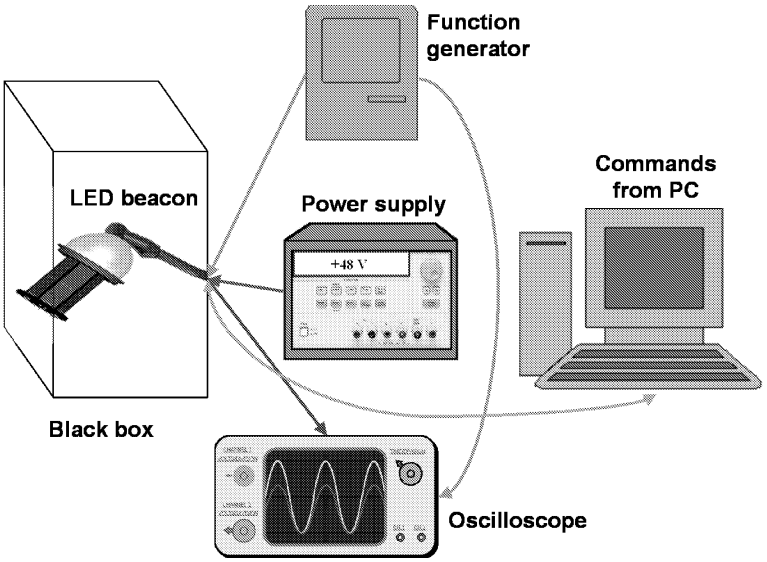


**Figure 4.1:** Schematical view of the setup used for the LED beacon test at Valencia.

2. Once all the components have been assembled in the nylon mechanical frame, we test the light emission of the faces and groups separately as well as the proper operation of the small PMT. The experimental setup conceived to do this test can be seen in Figure 4.1.

   As it is shown, the beacon is placed into a dark environment as the inside of a dedicated black box. A power supply feed the motherboard with 48V, and a pulse generator gives the trigger signal for the light emission. Finally, an oscilloscope displays the signals coming from the pulse generator and the small PMT.

3. All the LEDs can be illuminated after the pulse generator trigger signal arrival. The light is emitted simultaneously from all the LEDs within a range of $\sim$ 2 ns. However, the LED beacon is aimed to emit in a narrower range, in order to affect as less as possible the relative time resolution of $\sim$ 0.5 ns. Therefore, a synchronization procedure is needed in order to get all the LEDs flashing as synchronous as possible. This synchronization can be achieved tuning the adjustable capacitors placed in the pulser circuits of every face. With these capacitors, the time response of the LEDs can be moved in time to improve the synchronization.

   The first step of the synchronization process is to measure the attainable time range of the LED emission for all the beacon pulsers. This range is defined as the time difference between the fastest and the slowest LED emission after the trigger signal. In order to measure this range, a setup consisting of a small PMT[1] with a fibre optic attached on its photocathode has been devised. This fibre ends

[1]The PMT used in the synchronization process is identical to the one mounted in a LED beacon.

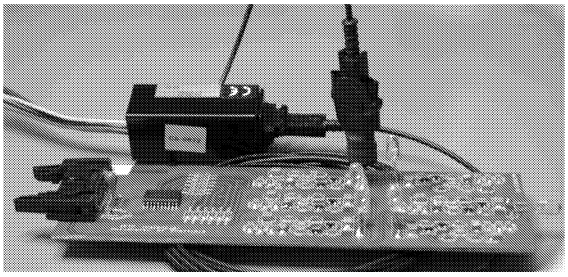

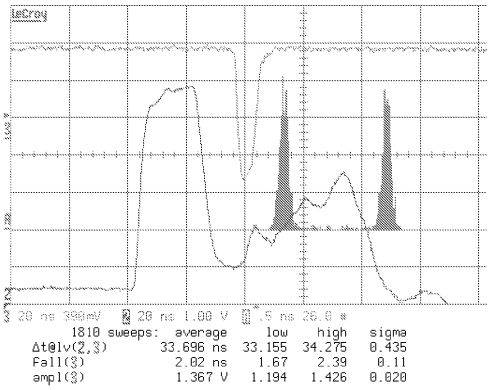


**Figure 4.2:** Picture of the hood system designed for the synchronization process (left side). Scope view of the attainable range of a single LED. In the same picture the blue line represents the PMT signal and the pink line represents the external pulse trigger signal (right side).

in a hood-shape plastic which fits perfectly into the LED cap as can be seen in the Figure 4.2.

The ranges are measured from the time difference distributions between the external trigger signal and the signal from the PMT attached to the optical fibre. This relative time difference is shown as an histogram on the scope. To compute the edge values of the range, we change the relative time difference trimming the adjustable capacitor. That produces a movement of the histograms on the scope. The mean values of the histograms for the limit cases, are taken as the range edge values (Figure 4.2).

When all the ranges are measured, the overlap among them has to be checked in order to set a common time emission. If there is no overlap, the cause of the problem is studied. Usually, a change in the adjustable capacitor is enough to solve the problem. Otherwise, if the problem remains, the whole face having the out-of-range pulser is replaced by a new one.

4. Once the overlap is guaranteed, a common time value of synchronization is chosen. This value is taken as the average between the minimum of all the maximum range values, and the maximum of all the minimum range values. An example of the 36 ranges of the pulsers from one LED beacon, and its final synchronization value is shown in the Figure 4.3.

   After the synchronization process, the LEDs emit within a $\pm$ 50 ps period on average. This fluctuation is expected not to affect the rising edge of the PMT signal when all the LEDs are flashed simultaneously. For time calibration, a sharp rising edge is crucial in the precise measurement of the actual time emission of

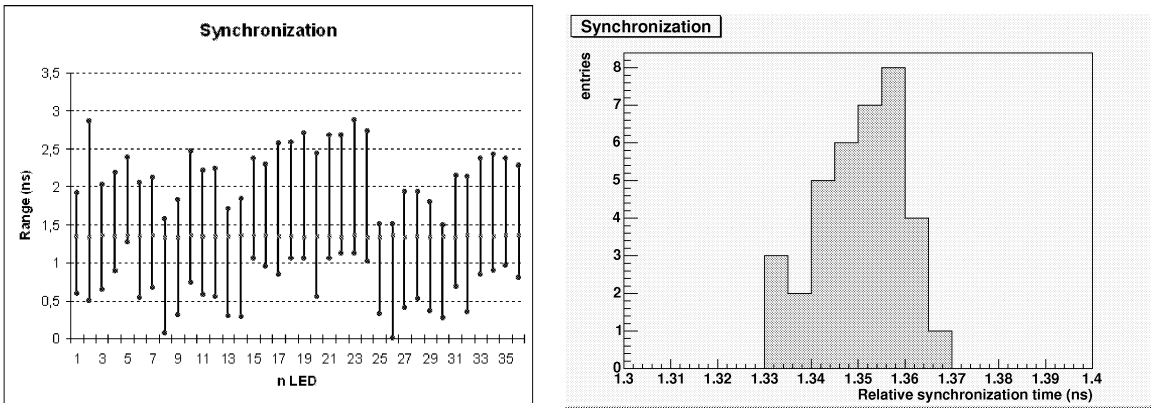


**Figure 4.3:** Plot showing the ranges of one beacon (left side). The red point means the final synchronization value for each single LED from this particular beacon. The histogram with the synchronization values of the 36 individual LEDs (right side).

the LED Beacon. The rising edge can be distorted due to a LED emission shifted in time with respect to the others. This effect has been simulated by Monte Carlo and will be presented in the next subsection.

5. In the following step, the synchronization face by face is checked. This synchronization is expected due to the previous pulser by pulser synchronization. The setup is the same than the one used in the point 2.

6. Afterwards, a thermal test is done. The optical beacon, once synchronized, is introduced into a test climate chamber where it is exposed to different thermal conditions. The test has a duration of 48 hours where the temperature varies between 10 and 40 degrees in 30 minutes cycles. That is usseful to check that the temperature does not affect the global synchronization.

7. A meticulous quality supervision test follows after the thermal test. The proper fixing of the different components: PMT, motherboard, plastic disc is checked. All the LED soldering are also revised one by one.

8. A more detailed study of the beacon is done aferwards. Correct operation of the LED intensity, PMT gain and a face by face synchronization better than 300 ps are required. A test of the beacon noise level is also performed.

9. Finally, the beacon is housed into the container and closed following the manufacturer specifications. Before the closing, the presure is reduced to 20000 - 60000 Pa pressure range, and nitogren gas is flowed into the container to avoid air condensation. Once the beacon is closed a last functional test is made to verify that nothing has been damaged during the closing procedure. Last of all, an scope snapshot of the beacon working at maximum intensity is recorded, as

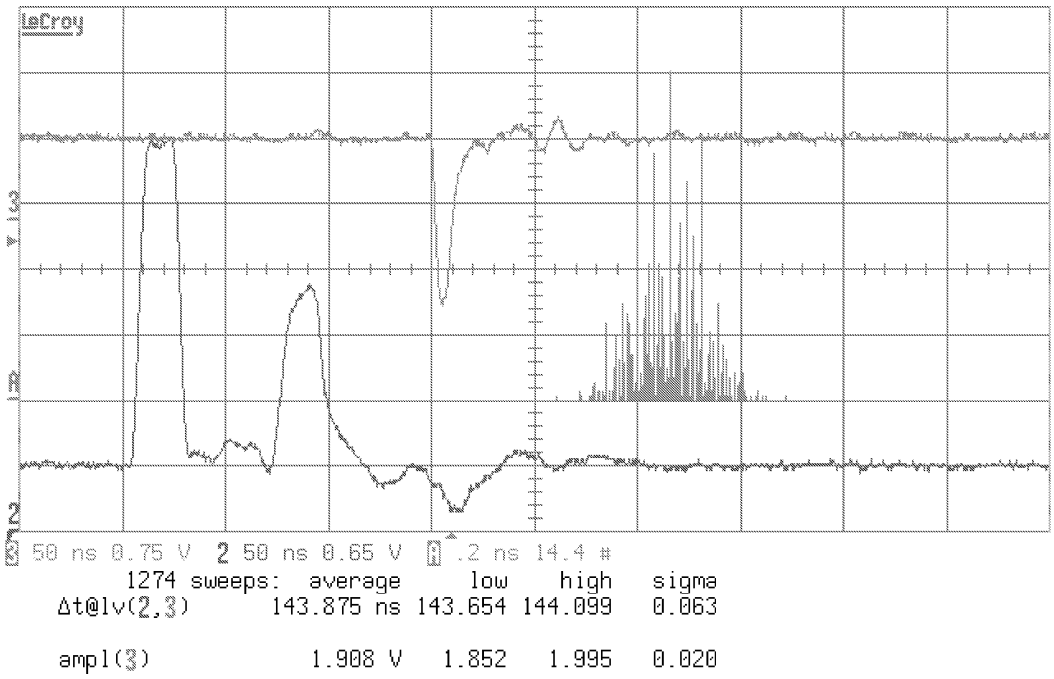


**Figure 4.4:** Example of a PMT signal recorded on scope (blue line), with the whole beacon (36 single LEDs) flashing simultaneously. The trigger signal is also ploted (pink line) as well as the histogram with the values obtained of the time difference between the LED and the trigger signal (orange).

a final proof of the correct beacon operation before being sent to the integration site (Figure 4.4).

### Rise time distortion effect due to a single LED desynchronization

In order to assess how can affect the desynchronization of one single LED to the synchronization of one whole face, a Monte Carlo simulation was performed. In this simulation, the parameter to consider was the rise time of the signals recorded in the PMT when a single LED is flashing. A small rise time gives a very precise time estimation of the LED light emission, and therefore, a growth in the rise time would cause a worse computation of the actual LED time emission and would reduce the relative time accuracy.

First of all, we considered the simplest case where the PMT signal is assumed to be a gaussian function with a rise time[2] of 2 ns. This rise time is directly related to the sigma ($\sigma$) of the gaussian distribution by the relation:

$$RT = \sigma \left| \sqrt{-2 \ln 0.9} - \sqrt{-2 \ln 0.1} \right| \simeq 1.69\sigma \tag{4.1}$$

as can be easily proven. The mean value of the distribution ($\mu$) was taken arbitrary as 0. With these values, 5 synchronous signals of equal rise time within a range of 100 ps were generated. A sixth signal was displaced on purpose. Afterwards, the sum of these six signals is fitted to the sum of two gaussian functions. For this new function, the rise time was computed. The process was repeated six times, adding a 0.5 ns displacement step to the moved signal every time.

In the Figure 4.5 left, the result of the rise time for each one of these 6 steps is presented. The increment of the rise time is greater than 1 ns for a displacement of 2.5 ns in a single LED.

Afterwards, a new simulation was performed but now, considering a perfect synchronization for the 5 LEDs signals, and a sixth signal displaced again by steps of 0.5 ns. The rise time computation was done in the same way than the previous Monte Carlo. The results are presented in the Figure 4.5 right. Comparing both cases, the conclusion is that the "desynchronization" within a range of 100 ps, is not important comparing to the one induced by a single LED shifted.

A further analysis was performed, now considering a more accurate fit for the single LED signal. After several attempts, the best fit function for the shape of the signal using the points provided by the scope turned out to be a double gaussian function. In the Figure 4.6, the results for a single and a double gaussian fit functions are presented. Clearly, the double gaussian fit is better than the single gaussian one, giving values for the rise time and the FWHM of 2.02 ns and 4.55 ns, respectively. These values are very close to the ones provided by the scope for the example signal of 1.96 ns and 4.76 ns.

[2]this is the typical rise time which is recorded on scope for a single LED signal.

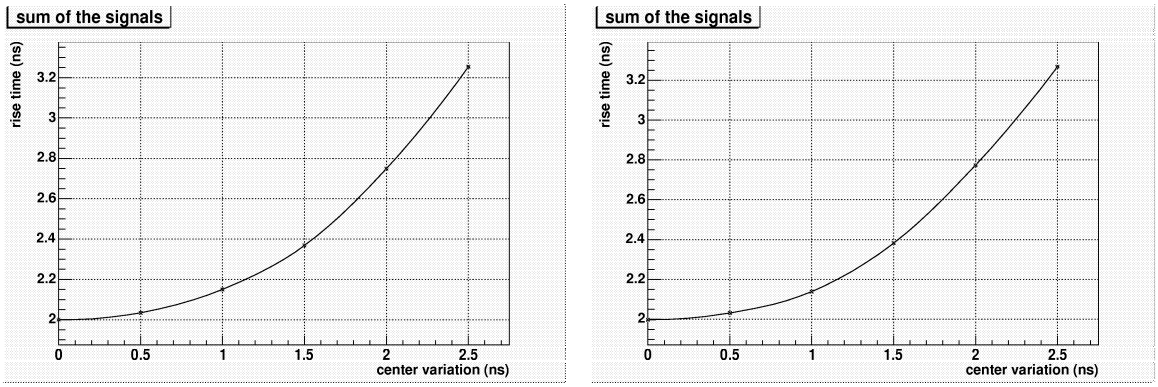


**Figure 4.5:** Rise time as a function of the center position of the moved gaussian. In the left side for signals synchronous within 100 ps, and in the right side for signals perfectly synchronized.

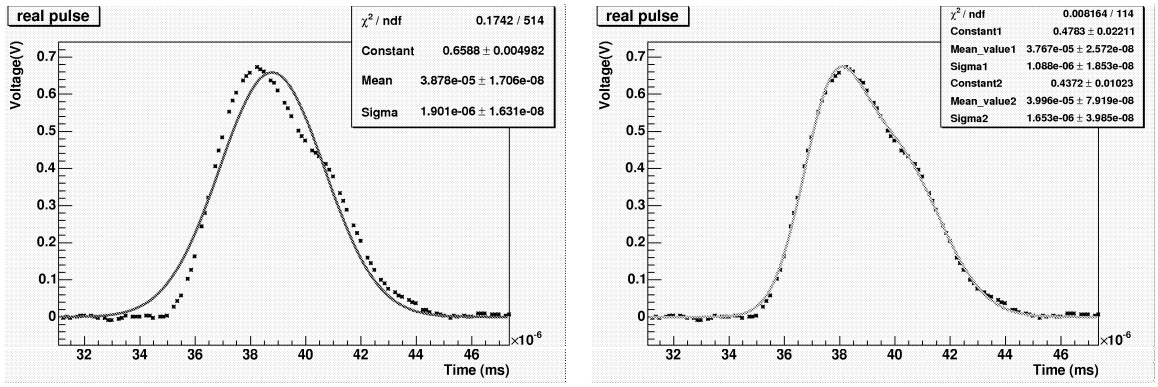


**Figure 4.6:** Fit of the single LED PMT signal provided by the scope, to one gaussian (left side) and two gaussians functions (right side).

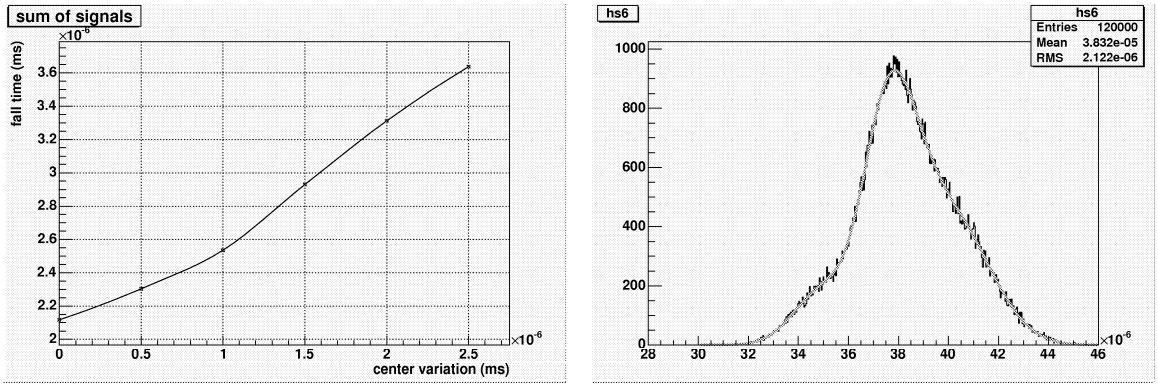


**Figure 4.7:** Rise time computation with respect to the center position of the moved signal for the case where the single LED signal is considered as a double gaussian (left side). An example of the 4-gaussian fit used in this simulation (right side).

Assuming this double gaussian shape behaviour, the simulation was performed again with 5 signals totally synchronized and one sixth signal displaced again by steps of 0.5 ns, as was done in the previous simulation. For the rise time computation, the fit function used was the sum of four gaussians. See Figure 4.7 for an example of the rise time fit.

The results, as can be seen also in the Figure 4.7 right side, show a slight increment of the rise time estimation, but the behaviour is similar to the one gaussian function case.

The conclusion of these simulation studies is that the effect of 1 displaced LED is important for a big single shift. However, for the synchronizations attained in Valencia, which are better than 300 ps face by face, this is a small effect which can be neglected.

### 4.1.2 Laser beacon tests

The Laser Beacon was fully tested in Valencia before being integrated in the MILOM line. A detailed description of the main features and tests carried out, can be found in [81]. The most important measurements done are summarized in:

1. A study of the time accuracy of the internal built-in photodiode was performed. A special setup with an additional external and very fast photodiode was devised to measure the arrival time of the laser signal. Results from the time difference between the two photodiode responses (Figure 4.8) show a jitter of $\sim 50$ ps. This jitter assures a precise time measurement necessary for time calibration with the laser beacon.

2. The energy per pulse emitted by the laser was measured using a calibrated pho-

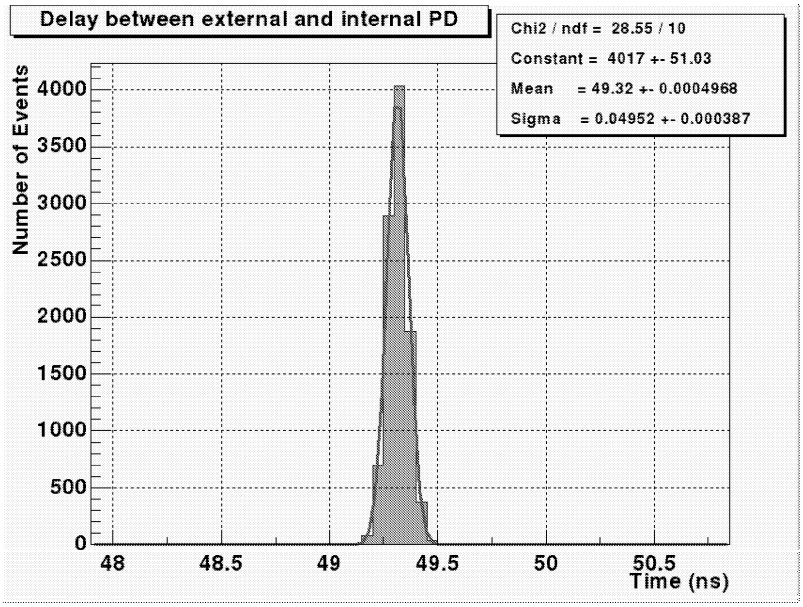


**Figure 4.8:** Time difference between the two photodiode responses. The 50 ps jitter obtained is far better the precision needed for our application.

todiode[3] able to measure energies with an accuracy better than 1 nJ. The Figure 4.9, shows the energy per pulse during the first 90 minutes after a switch-on at a fixed trigger frequency. This energy stability has also been tested using different trigger frequencies and longer time periods.

3. A preliminary study was done with the aim of achieving an adjustable intensity in the laser light emission. In this test a crystal liquid polarizator is placed between the laser and the quartz rod, acting as a filtre. The polarization depends on the voltage supply. Therefore, this polarizator allow us to select the laser intensity (Figure 4.10). This tunable filter was not implemented in the Laser Beacon placed in the MILOM line. However, it is foreseen for the following laser beacons.

## 4.2 Pre-Integration of the Optical Beacons at CPPM

Previously to the final test of the Optical Beacons in the line integration phase, a series of pre-intregration tests are carried out in order to check that the beacon operates properly before being integrated with its final ARS in the DAQ system. These tests are very important to optimize the Optical Beacon production in Valencia, and to reduce the time of the final integration tests.

[3]OPHIR PD10 with an OPHIR LaserStar readout.

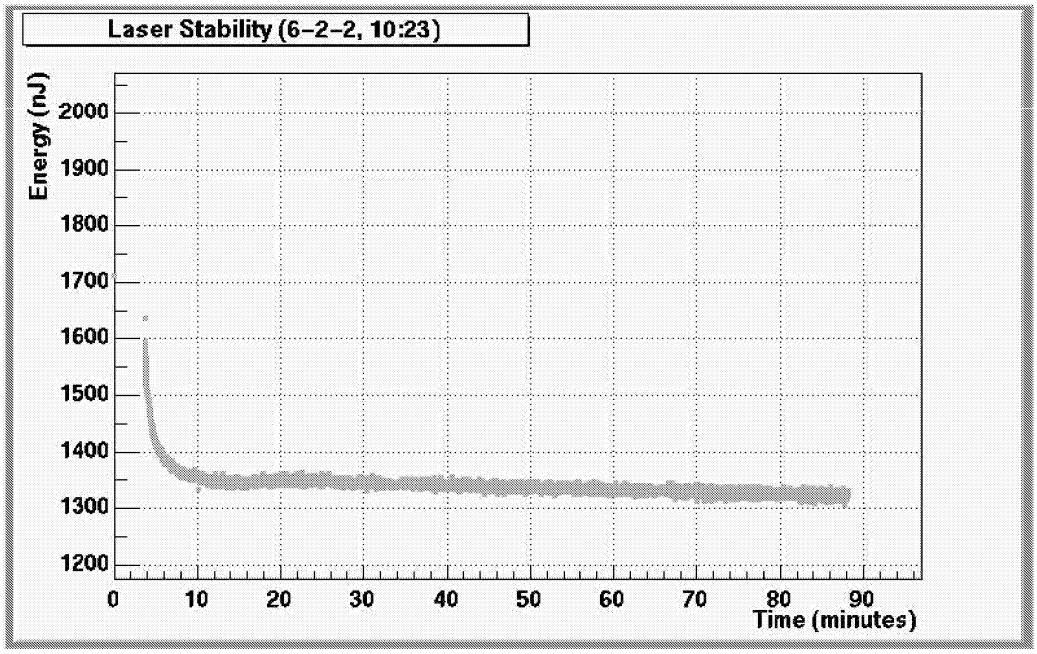


**Figure 4.9:** Measurement of the energy per laser pulse as a function of time.

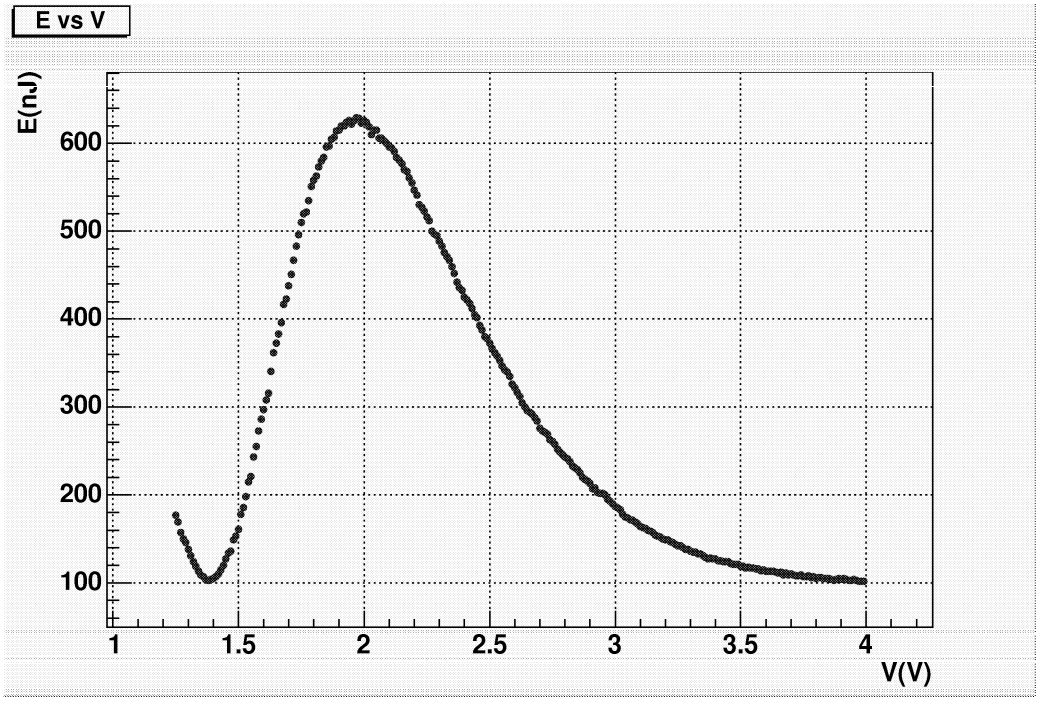


**Figure 4.10:** The laser intensity depending on the voltage applied to the polarizator.

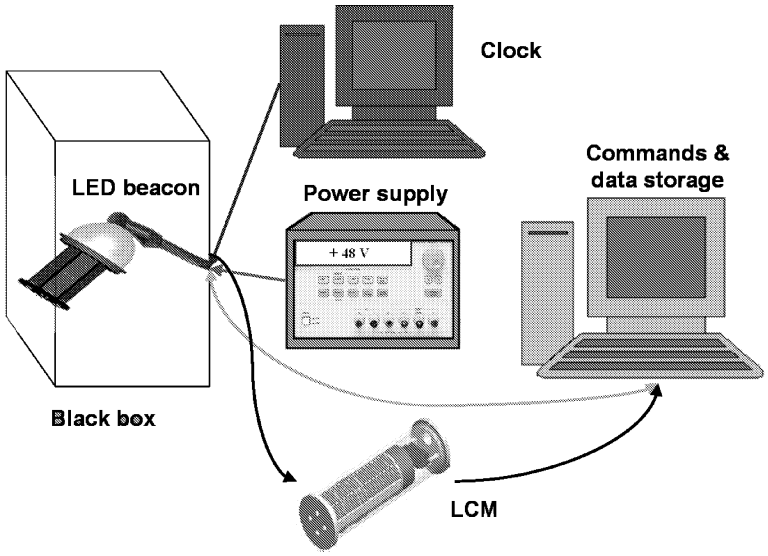


**Figure 4.11:** Schematical view of the setup used in the integration site for the pre-integration tests.

### 4.2.1 LED Beacon pre-integration tests

For the pre-integration tests, the Optical Beacon is connected to a reference LCM which is the same LCM for all the pre-integration tests. This LCM contains the ARS for the small beacon PMT readout in the same way as in the detector once deployed. An external power supply is used to feed up the LED beacon with 48 V. The LED Beacon is placed in a metal cylinder box covered by a black cloth which provides the desired dark environment. The slow control commands to communicate with the LED Beacon are sent from a dedicated PC. The RunControl controlling the DAQ program clients, is launched in the same PC. Finally, the external trigger to flash the LEDs, is given from another PC which is in charge of the clock system control. A sketch of the setup used is presented in the Figure 4.11.

With this setup, the first data runs are taken and the first LED Beacon signals are registered by its dedicated ARS in the reference LCM. The aim of these previous tests is to check the LED Beacon operation and the slow control communication. In this sense, different values of LED intensities and PMT gains are applied. Some examples of the signals taken at different run configurations are presented in the Figure 4.12.

The AVC and TVC distributions for a typical beacon run are presented in the Figure 4.13. The LED beacon presents a gaussian distribution in the AVC charge. Since the trigger signal is provided synchronous with the 20 MHz clock signal, the TVC distribution shows a very narrow peak.

It is important to remind that two TVCs are working on each ARS, even for the beacon ARS. Therefore, they have to be calibrated individually in order to get as better time resolution as possible. The two TVC distributions for the same ARS beacon can

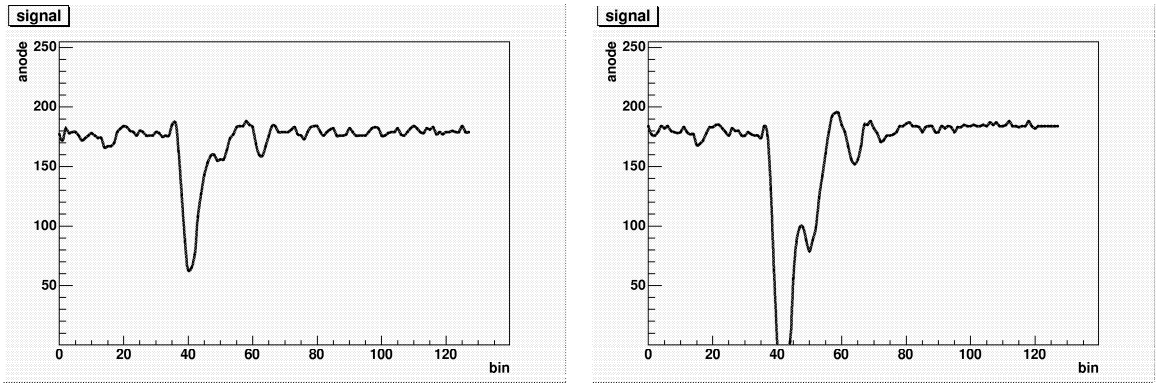


**Figure 4.12:** WF snapshot examples of signals recorded in the beacon ARS coming from the small internal PMT. These WF signals were taken for different PMT gains and LED intensities when all the 36 LEDs were flashing.

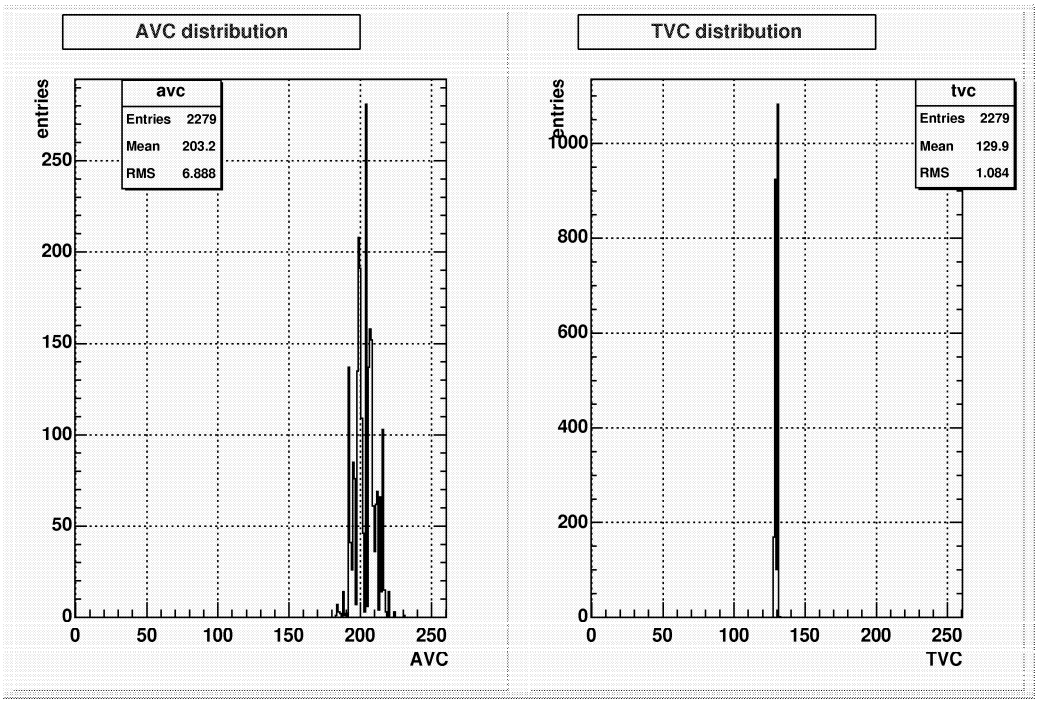


**Figure 4.13:** The AVC and TVC distributions for a run with all the 36 LEDs flashing simultaneously at high intensity and intermediate PMT gain.

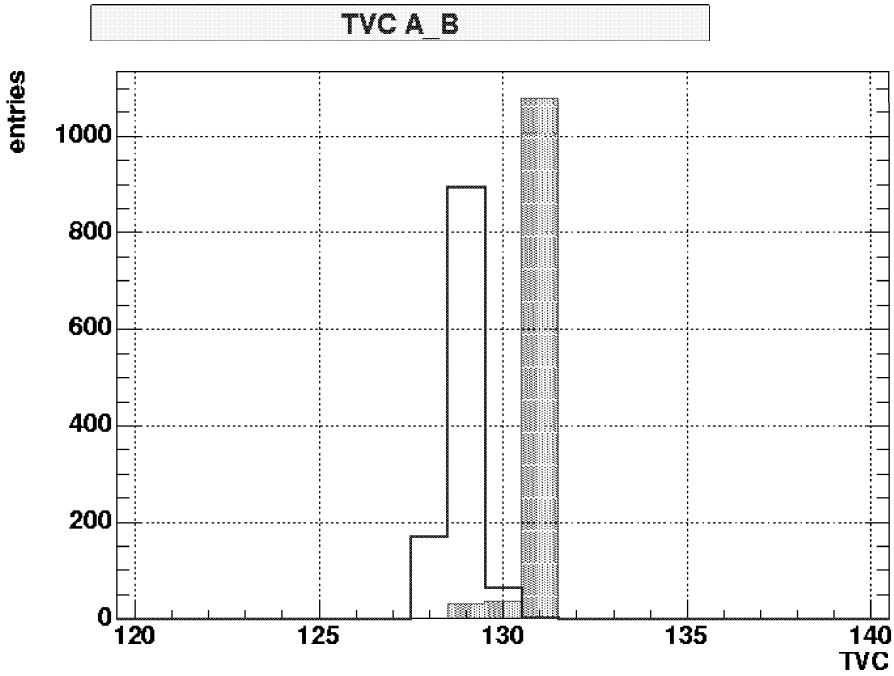


**Figure 4.14:** A more narrow distribution is obtained in the TVC distributions when both ARS TVCs are ploted separately. When they are calibrated separately a better time resolution is obtained.

be seen separately in the Figure 4.14.

In the pre-integration, the noise level was also measured and its possible sources analysed. This noise can affect either the AVC and the TVC distributions as can be seen in the Figure 4.15. Analyzing the AVC versus TVC distribution we can classify the picked up noise. On the one hand, we have not very intense noise signals which appear randomly in time. They are probably caused by the electronics. However, they are more intense when the slow control commands for the beacon configuration are sent (at the beginning or at the ending of the run). This time random noise reached an important high level in the first pre-integration tests made in November 2004. It had a characteristic sinusoidal-shape as can be seen in the Figure 4.17. However, it was greatly reduced in the last pre-integration tests (January 2005) due to some improvements in the shieldings of the beacon connections. For the time being, the random noise intensity has been reduced enough to be avoided with a typical L0 threshold level.

On the other hand, we have noise signals that appear correlated with the trigger clock pulser. This is known because these signals are synchronous in time and present a sharp distribution in TVC (see Figure 4.15 right). This noise is very difficult to reduce and changes from LED Beacon to LED Beacon, what forces us to do an individual measurement of the L0 threshold parameter for each LED Beacon in order to avoid

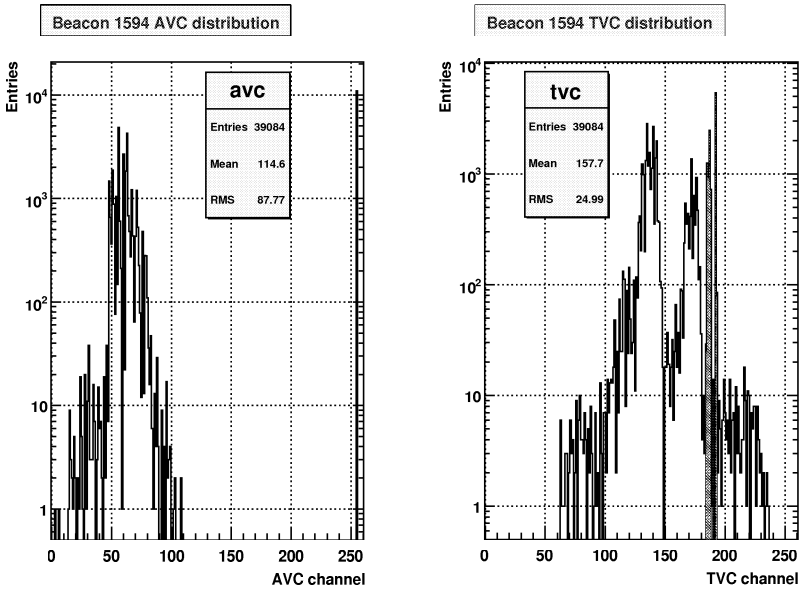


**Figure 4.15:** The AVC and TVC distributions for a noisy run. The distributions are clearly affected by the noise. In the AVC distribution (left side) the LED signal is completely saturated (AVC=255). In the TVC distribution (right side) the LED signal is highlighted in red.

it. In principle, the standard Optical Beacon ARS L0 threshold is enough to avoid the noisy signals. However, in some cases this L0 value has to be increased to higher values.

Both kind of noisy signals can be distinguish in the AVC versus TVC distribution (Figure 4.16).

It is crucial to eliminate as much as possible the noise in order to avoid erroneous values of the light time emission (Figure 4.17 right).

### 4.2.2 Laser Beacon pre-integration

The Laser Beacon was tested with the same idea of checking its correct operation once it is integrated in the ANTARES DAQ system. The setup used for the test was the same than the one used for the LED Beacon. Due to the Laser Beacon construction, it was no necessary to shelter it from the ambiental light. The laser signals were also recorded using a reference LCM.

The first signals obtained in WF mode showed that the signal recorded by the internal photodiode was too big to fit into the WF window in the laser ARS. This was reduced up to fit the WF window (Figure 4.18) by a 45%. The signal reduction was done in the transmission path from the internal photodiode to the ARS using a transformer.

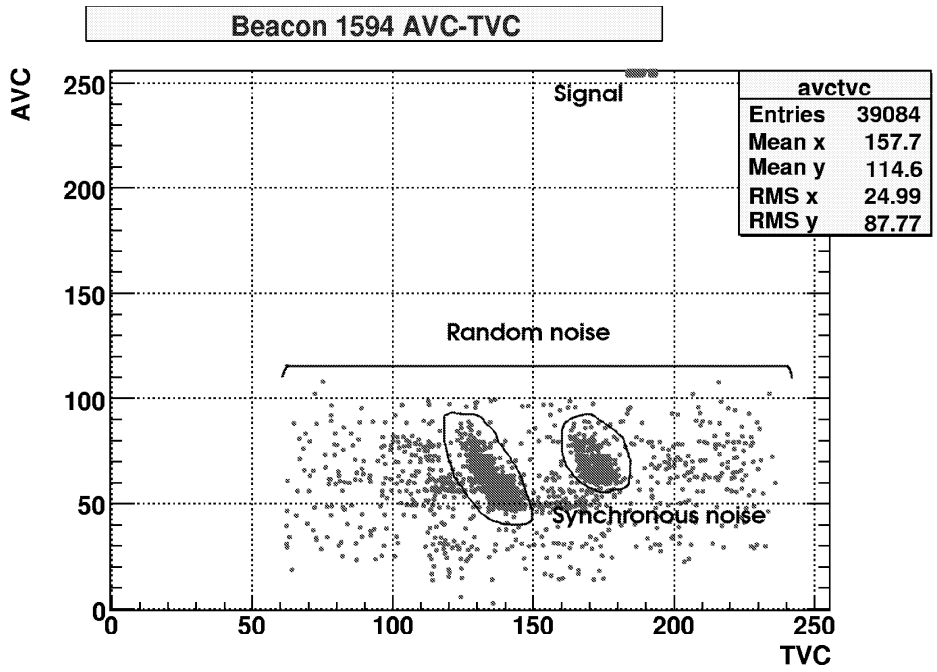


**Figure 4.16:** The AVC versus TVC distribution. Both kind of noises, synchronous and random, can be distinguished as well as the actual PMT signal.

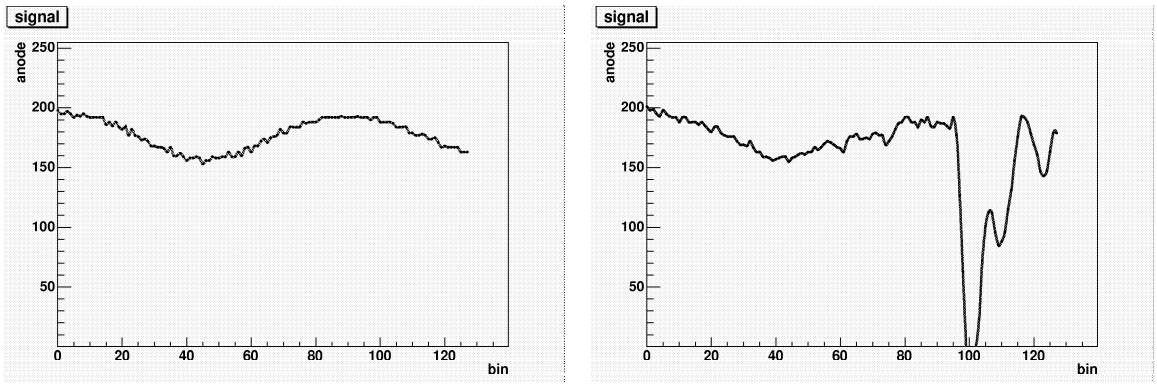


**Figure 4.17:** WF signal example of the time random noise recorded in the beacon ARS in the first tests made with the beacon (left side). This noise can appear in a few cases coupled to the PMT LED beacon signal (right side).

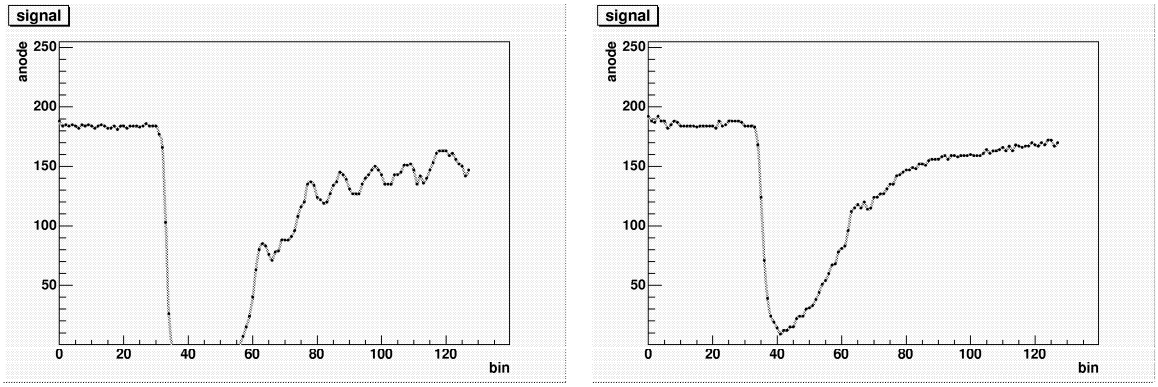


**Figure 4.18:** WF example of a recorded signal in the laser beacon ARS coming from the internal photodiode. The signal was reduced by a 45% in order to fit into the WF window.

The same noise sources as in the LED Beacon appear in the Laser Beacon. However, the level is lower probably due to the different electronic associated to the built-in photodiode. Therefore, with the standard L0 threshold values for the Optical Beacon ARSs, these noisy signals are completely avoided.

## 4.3 MILOM integration tests

The two Optical Beacons allocated in the MILOM line, were integrated with their final LCMs between the end of February and the beginning of March of 2005. In these tests, a more detailed study using the beacon ARS signals was performed.

### 4.3.1 MILOM LED Beacon tests

The setup used for the integration tests was basically the same than the one used in the pre-integration phase, with the only difference that now, each LED Beacon was tested with its own LCM foreseen in the MILOM line. This allowed a more detailed study of the beacon properties with its final configuration in the line.

In addition to the full operational tests, new tests for calibration analysis were performed. The first test was to check that the AVC and TVC distributions of one single LED were similar to those obtained when all the LEDs were flashing simultaneously. This can be confirmed looking at the Figures 4.13 and 4.19.

The Tables 4.1 and 4.2 present the mean values and the RMS values of the TVC and AVC distribution respectively for the *top* LEDs of the beacon when they are flashing one by one.

The final LED Beacon connections used in the beacon integration can distort the final PMT signal with respect to the one, more clean, taken in Valencia. Studies about

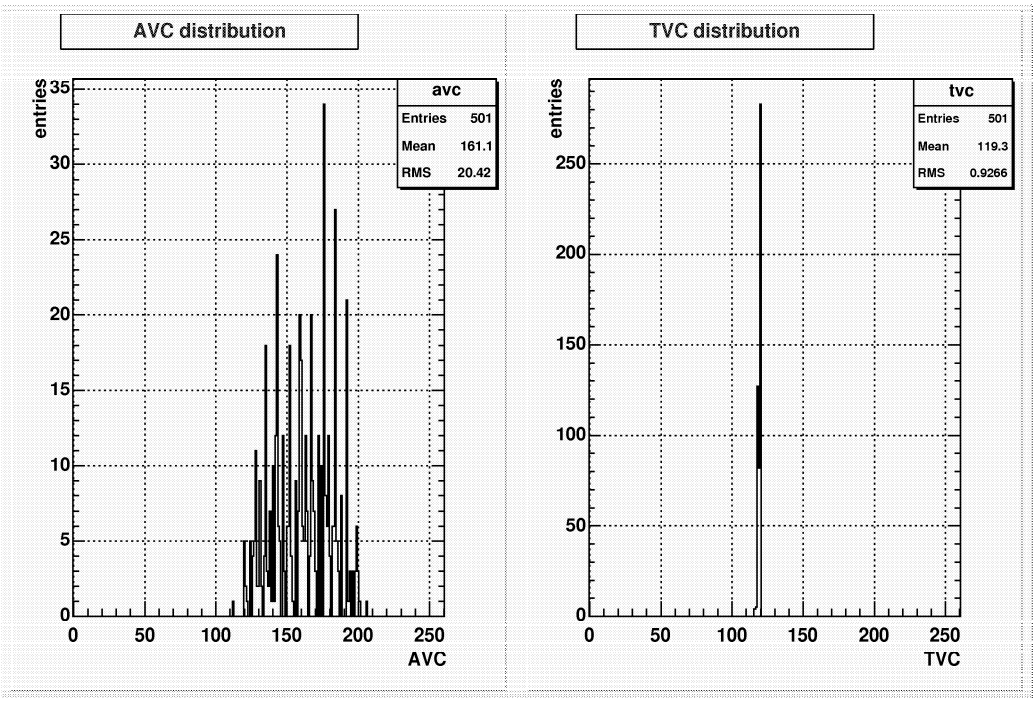


**Figure 4.19:** The AVC and TVC distributions for one single *top* LED of the beacon. The distributions are similar to the ones obtained when all the LEDs are flashing simultaneously.

| LED | Mean (ADC channel) | RMS | entries |
|---|---|---|---|
| 1 | 161 | 20 | 501 |
| 2 | 166 | 20 | 315 |
| 3 | 161 | 21 | 412 |
| 4 | 150 | 19 | 316 |
| 5 | 152 | 20 | 317 |
| 6 | 160 | 21 | 112 |
| All | 158 | 21 | 1973 |

**Table 4.1:** Table with the AVC mean values obtained flashing LED by LED independently for the *top* LEDs of the beacon used for the MILOM integration tests.

| LED | Mean (ADC channel) | RMS | entries |
|---|---|---|---|
| 1 | 119.3 | 0.9 | 501 |
| 2 | 117.5 | 1.2 | 315 |
| 3 | 119.6 | 0.7 | 412 |
| 4 | 119.7 | 0.7 | 319 |
| 5 | 119.4 | 0.9 | 317 |
| 6 | 118.3 | 1.3 | 112 |
| All | 119.1 | 1.2 | 1973 |

**Table 4.2:** Table with the TVC mean values obtained flashing LED by LED independently for the *top* LEDs of the beacon used for the MILOM integration tests.

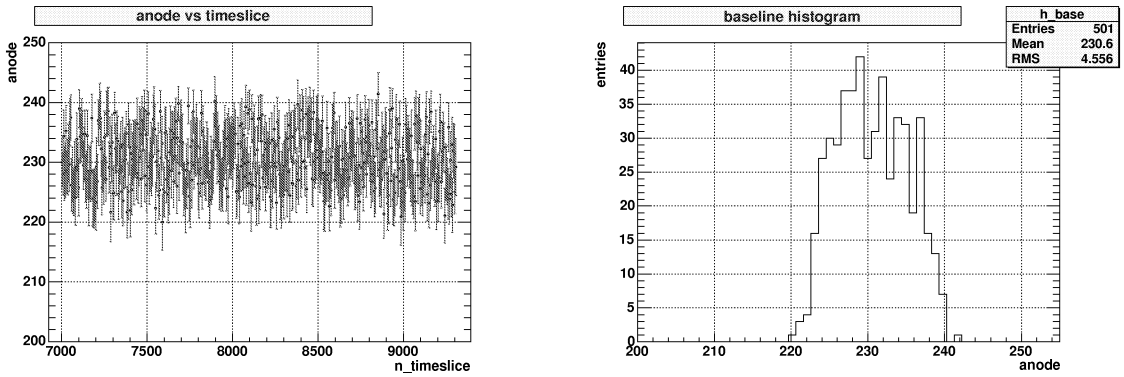


**Figure 4.20:** The baseline measurements for the ARS when only one single *top* LED was flashing. In the left side, the baseline values with its error as a function of time. The distribution of the baseline values is represented in the right side histogram.

how this effect can modify the signal shape and, therefore, the rise time measurements, has been done using the ARS signals coming from the small beacon PMT.

First of all, to compute the signal rise time, an estimation of the WF baseline was necessary in order to substract it from the signal. This baseline is computed averaging the values of the precedent points to the LED signal. The baseline was computed for every LED ARS signal. The obtained values are shown in the Figure 4.20 left. The error bars are the RMS of the points used for the baseline computation. The baseline average values of all the events for all the single *top* LEDs are presented in Table 4.3. The results among the *top* LEDs of each face are very similar.

With these baseline values, the rise time was computed fitting 5 WF signal points to a 4-degree polynomial. The 5 chosen points were the maximum in charge in the WF frame, the one forward point in time and the 3 backwards. The charge amplitude is computed as the difference in charge (anode) between the polinomial fit maximum and the baseline previously computed. An example of one WF signal fit is presented

| LED | Mean (ADC channel) | RMS | entries |
|---|---|---|---|
| 1 | 230.6 | 4.6 | 501 |
| 2 | 230.7 | 4.6 | 315 |
| 3 | 230.9 | 4.9 | 412 |
| 4 | 230.7 | 4.5 | 316 |
| 5 | 230.3 | 4.6 | 317 |
| 6 | 230.3 | 4.9 | 112 |
| All | 230.6 | 4.7 | 1973 |

**Table 4.3:** Table with the baseline mean values obtained flashing LED by LED independently for the *top* LEDs of the beacon used for the MILOM integration tests.

| LED | Mean(ns) | RMS | entries |
|---|---|---|---|
| 1 | 2.77 | 0.22 | 501 |
| 2 | 2.78 | 0.20 | 315 |
| 3 | 2.73 | 0.21 | 412 |
| 4 | 2.76 | 0.23 | 316 |
| 5 | 2.79 | 0.24 | 317 |
| 6 | 2.83 | 0.26 | 112 |
| All | 2.76 | 0.17 | 1973 |

**Table 4.4:** The rise time values obtained LED by LED for the *top* ones.

in the Figure 4.21.

The rise time studies were performed for all the groups of both MILOM LED beacons. The results obtained for all the LEDs flashing case and for 1 *top* LED can be seen in the Figure 4.22, where the rise time distribution are shown.

In the Table 4.4, the values for all the *top* LEDs of the same beacon flashing one by one are presented. The rise time is around 2.8 ns for all the *top* LEDs of the beacon. These values are greater than the typical rise time of $\sim$ 2 ns measured in Valencia as it was expected due to the more complex connections for the final electronics.

One more analysis done was the study of the flashing rate of the beacon and, therefore, the stability during a given run. In the Figure 4.23, a graph from one run with the LED Beacon flashing very precisely at 5 Hz can be seen, with a pause period during a change of the configuration parameters. This LED Beacon flashing rate has also been checked with the LED Beacons of the MILOM and Line 1. For instance, the LED Beacon in the MILOM has been working at 30 Hz. An unexpected LED Beacon rate can reveal the existence of any problem. For instance, a high noise would give an increment on the beacon ARS signals and therefore a rate increment.

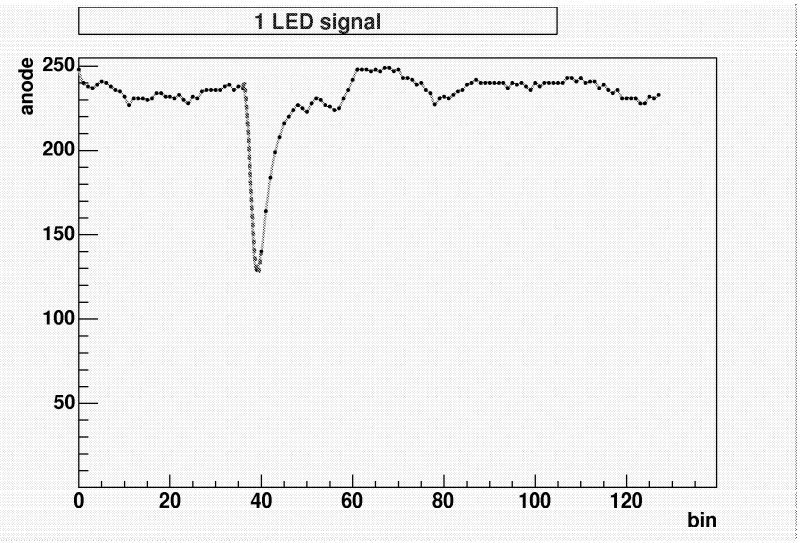


**Figure 4.21:** WF signal example obtained in the integration of the LED Beacon in the MILOM line with the fit used for the rise time calculation (dotted line).

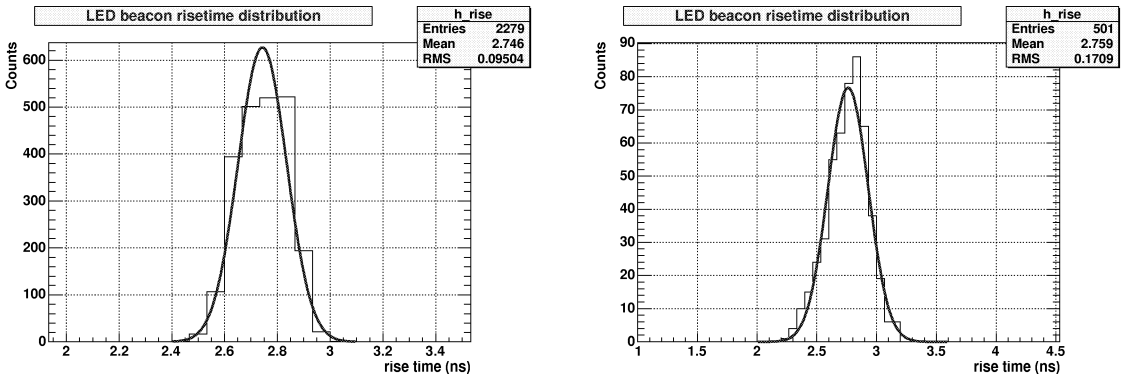


**Figure 4.22:** The rise time distribution for the LED Beacon when all the LEDs are flashing (left side) and when only one *top* LED is flashing (right side).

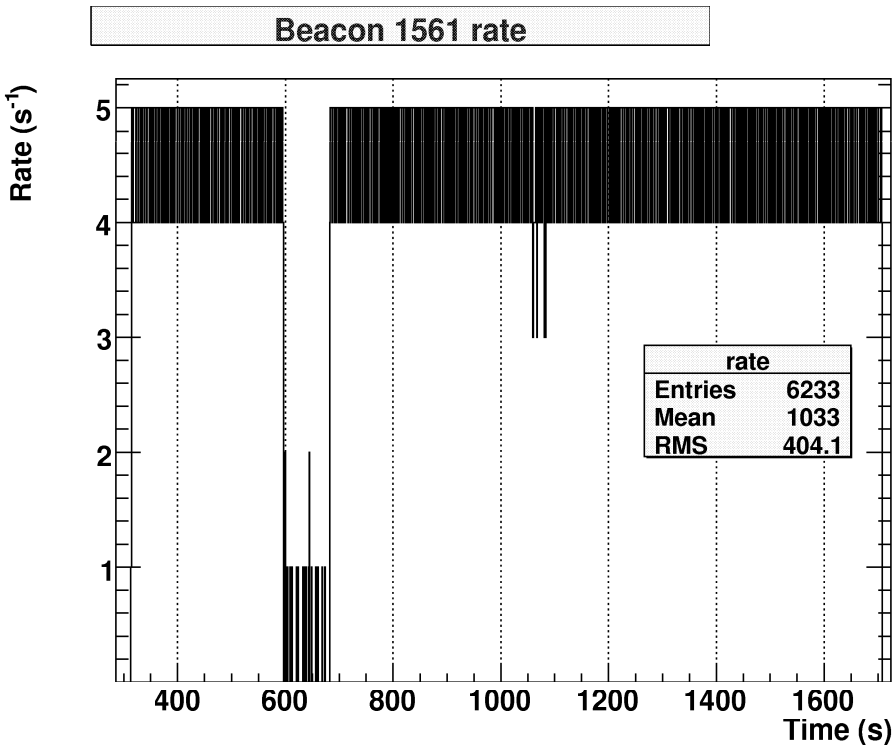


**Figure 4.23:** Flashing rate of the LED Beacon during a typical run. A pause period during a change of the configuration parameters (PMT gain and LED intensity) can be seen for this run.

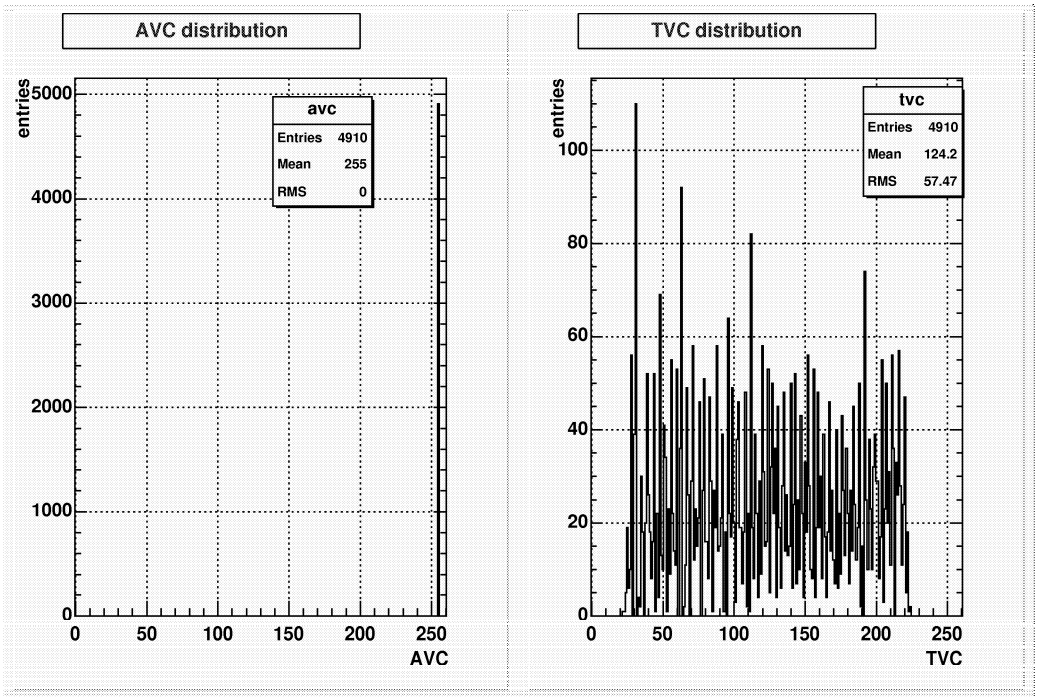


**Figure 4.24:** The AVC and TVC distributions for the run with the Laser Beacon. Due to the big width of the signal, the AVC is always saturated. The TVC values are randomly distributed due to the big Laser Beacon jitter in time emission.

### 4.3.2 MILOM Laser Beacon tests

The Laser Beacon integration was very quick because the Laser Beacon test was basically the same that was already done in the pre-integration period. A run was performed to check again its correct operation. The results for the AVC and TVC distributions are presented in the Figure 4.24. The AVC distribution is always saturated because of the big width of the laser signal. The TVC distribution is flat because the jitter in the laser time emission, after the trigger signal, is around hundreds of nanoseconds, while the TVC range is of 50 ns. Therefore, the TVC signal values are randomly distributed. The analysis of the rise time of the ARS signals coming from the internal photodiode with the Laser Beacon integrated, was also done. As in the rise time computation of the LED signal, the baseline estimation was necessary. The results were obtained with the same procedure, and can be seen in the left side of the Figure 4.25. Due to the longer rise edge of the Laser Beacon signal, the fit was done using 13 points. These were the points corresponding to the maximum value, the 11 previous points to the maximum and the point after the maximum. The fit was done to a 10-degree polynomial (Figure 4.25 right).

The rise time distribution for the laser run can be seen in the Figure 4.26. What is important in the rise time laser distribution is its stability ($\sigma \sim 0.3$ns) which means

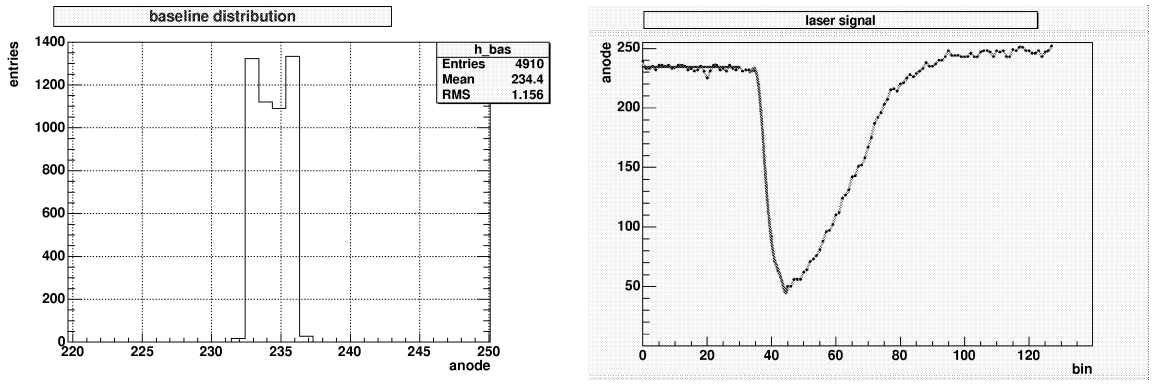


**Figure 4.25:** The Laser Beacon baseline distribution for the rise time computation (left). One example of laser WF fit for the baseline and rise time computations (right).

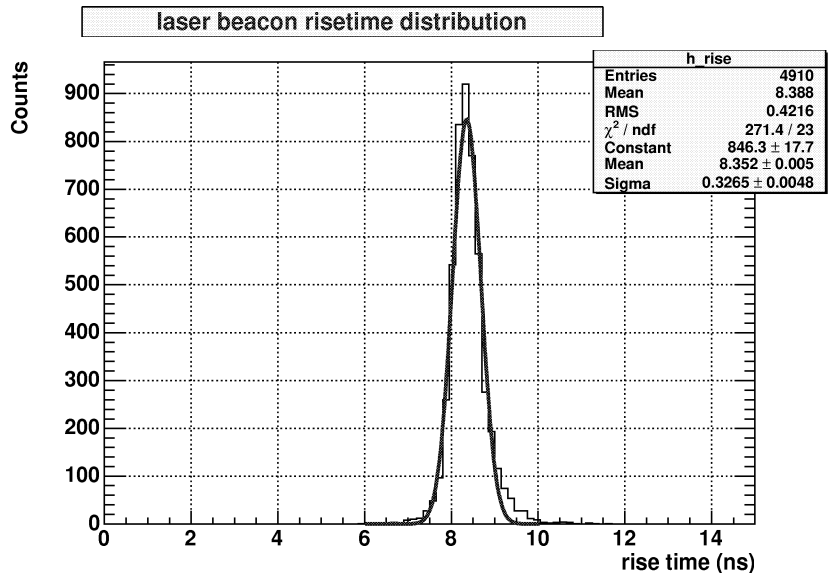


**Figure 4.26:** The Laser Beacon rise time distribution, taken from the WF signal recorded by the laser beacon ARS. This rise time is very stable with a $\sigma \sim 0.3$ ns.

that the signal shape seen by the ARS is very stable, i.e., it will not change from one laser flash event to another. This is crucial for good time off-sets computations.

## 4.4 Line 1 LED Optical Beacon integration

As all the lines in the ANTARES detector, the Line 1 contains four LED Beacons. They were tested between October and December of 2005. For these tests, the setup used was similar to the pre-integration setup. The main differences were the location of the LED Beacons, which were placed in the dark room as the OMs, and that every beacon was tested with its own and definitive LCM in the Line 1.

The analysis of the Line 1 integration tests, have been useful to decide the final test procedure for the detector line integration. Concerning the Optical Beacon integration, two tests have been proposed and finally adopted. On the one hand, the test with the laser by optic fibre as has been explained in Chapter 3. In this test, a specific fibre is used to illuminate the small internal PMT of the LED Optical Beacon. The $\mathrm{TVC}_{min}$ and $\mathrm{TVC}_{max}$ of both TVCs are obtained as well as the time off-set of the beacon ARS ($\Delta t$ parameter).

On the other hand, a functional test where the LED Beacon is illuminated by its own LEDs is performed as a proof of its proper operation. This test is also useful in order to check the noise level of the beacon and, therefore, to choose the appropriate L0 threshold value for the beacon ARS before the deployment.

The results obtained from the laser by optic fibre system for the $\mathrm{TVC}_{min}$ and $\mathrm{TVC}_{max}$ parameters of the beacon ARSs are presented in the Figure 4.27.

In the second test were the LED Beacon is flashing itself, everything presents a correct operation as can be seen in the Figure 4.28, where the AVC and TVC distribution of the 4 beacons of the Line 1 are shown

The noise level was checked with changeable levels from beacon to beacon (Figure 4.29). Finally, the ARS threshold values were selected to avoid the noise once the line is deployed.

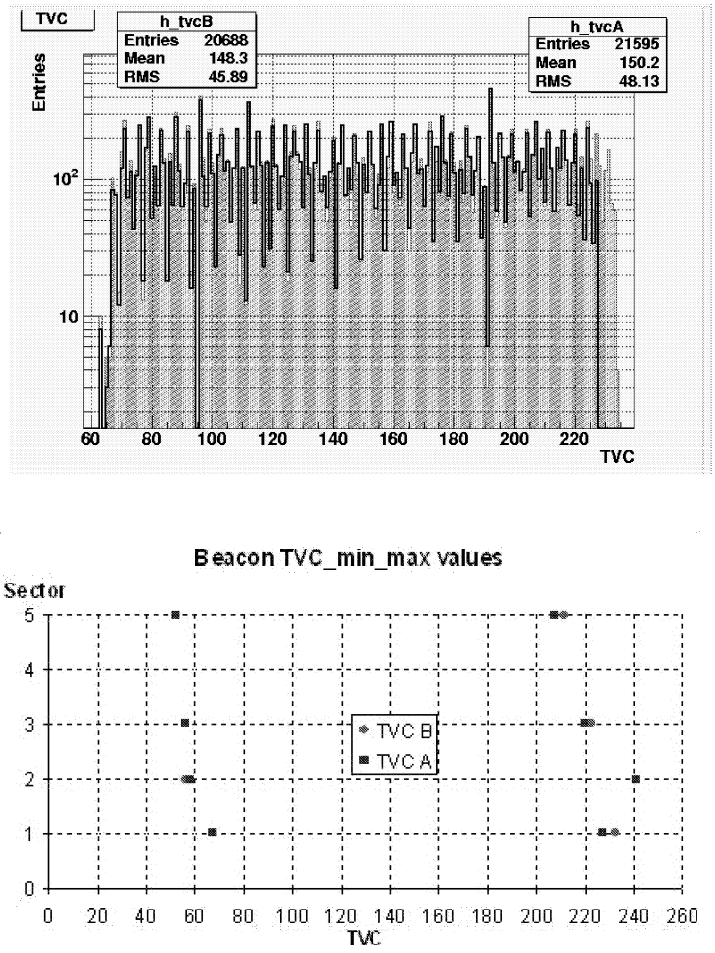


**Figure 4.27:** Example of the TVC flat distribution for one Optical Beacon devised for the Line 1 (up). Graph showing the $TVC_{min}$ and $TVC_{max}$ values of both TVCs, for the four beacons of the Line 1 (down).

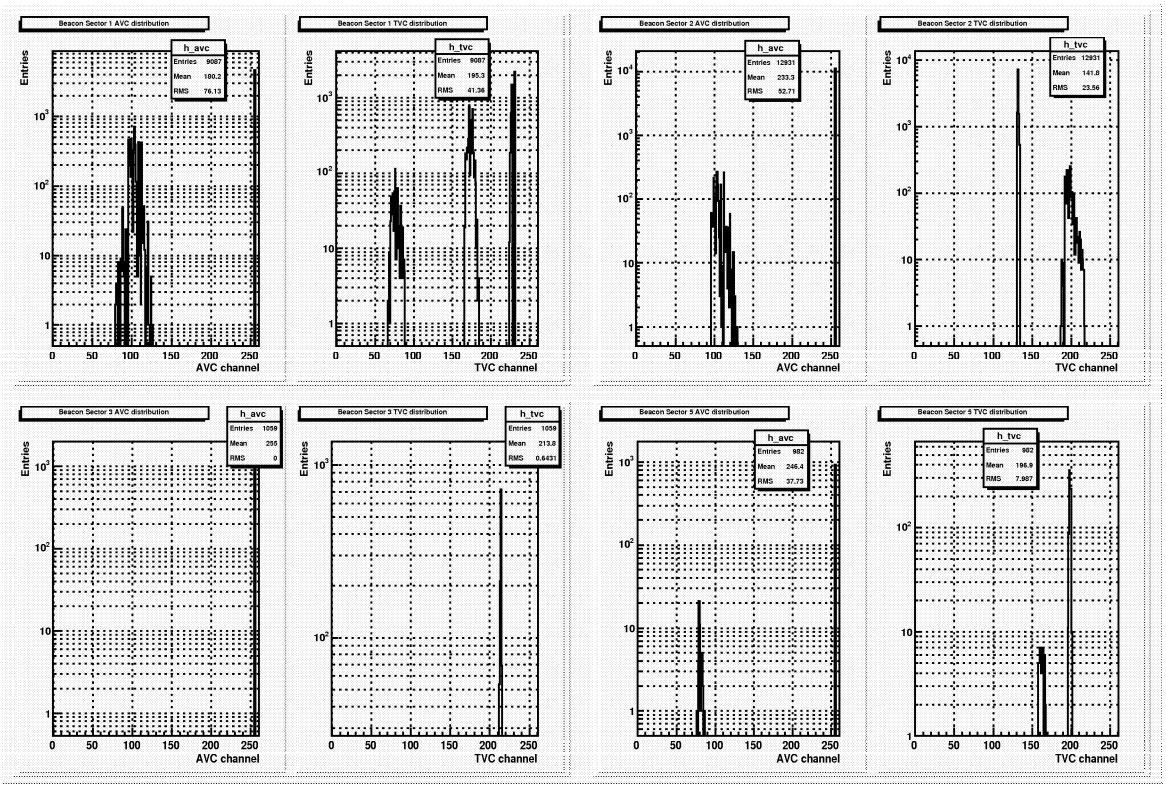


**Figure 4.28:** AVC and TVC distributions for the 4 LED Beacons of the Line 1. The AVC for the LED Beacon signal has been chosen in saturation (255) deliberately in order to distinguish the noise level in the beacon. In the TVC distributions the LED signal appears as the most narrow peak.

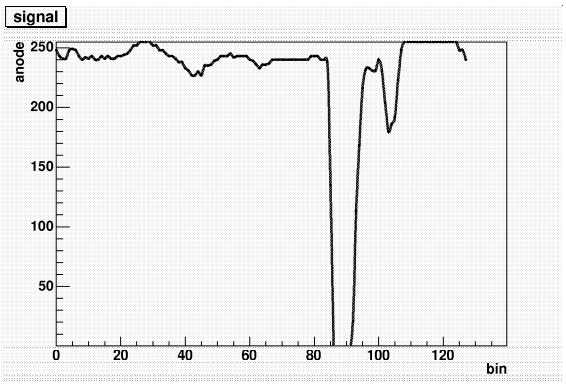


**Figure 4.29:** Example of the LED beacon WF signal obtained with the final beacon LCM. The noise induced by the trigger clock pulser can be noticed just before the LED Beacon signal.

# Chapter 5

# Data analysis of the MILOM line

After the integration tests of the instrumentation line, the MILOM was deployed and connected during the spring of 2005. This represented a very important success since the MILOM line provided the first results with the final components of the detector. In this chapter we present a review of the most relevant measurements carried out with the MILOM line concerning the Optical Beacons.

## 5.1 Results from the LED Beacon

The MILOM line is equipped with two LED Beacons. However, due to the MILOM configuration (Figure 2.25), only one beacon can be tested with the OMs supported by the line. Therefore, we will focus on the results obtained for the lower Optical Beacon as it is shown in the schematic view of the Figure 5.1.

The notation for the 3 OMs in the storey above the LED Beacon is the following. They are called OM_0, OM_1 and OM_2 and the ARSs associated to each OM are called ARS_0 and ARS_1 for OM_0, ARS_2 and ARS_3 for OM_1, and ARS_4 and ARS_5 for OM_2. The ARS reading the small LED Beacon PMT signal is called ARS_6.

First of all, the correct operation of the LED Beacon was tested. The AVC and TVC distributions for the ARS which is in charge of the readout of the internal PMT were measured again giving values as expected (Figure 5.2). The rate of the LED Beacon were confirmed, and no noise signals appear in the data acquisition of the ARS_6.

### 5.1.1 Risetime measurement

In addition, the WF signals were also studied. With these signals the rise time was computed in order to see if the signal shape had changed. The rise time values were computed in the same way as has been explained in the previous chapter. The Figure 5.3 shows the rise time distribution obtained when all the LEDs of the beacon were flashing simultaneously. The mean rise time value of 2.7 ns taken at the sea with the WF signals agrees with the value obtained in the dark room tests.

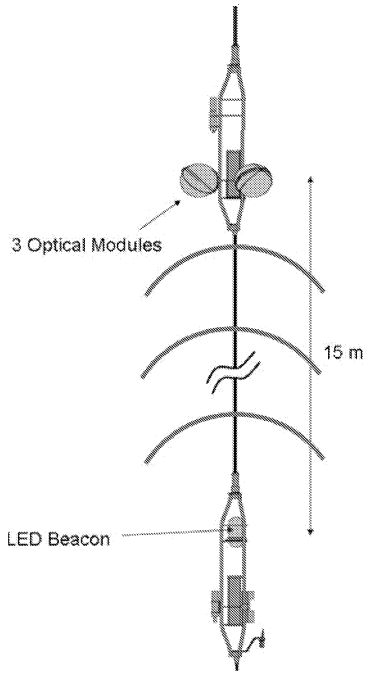


**Figure 5.1:** Schematic view of the relevant MILOM part for the LED Beacon runs.

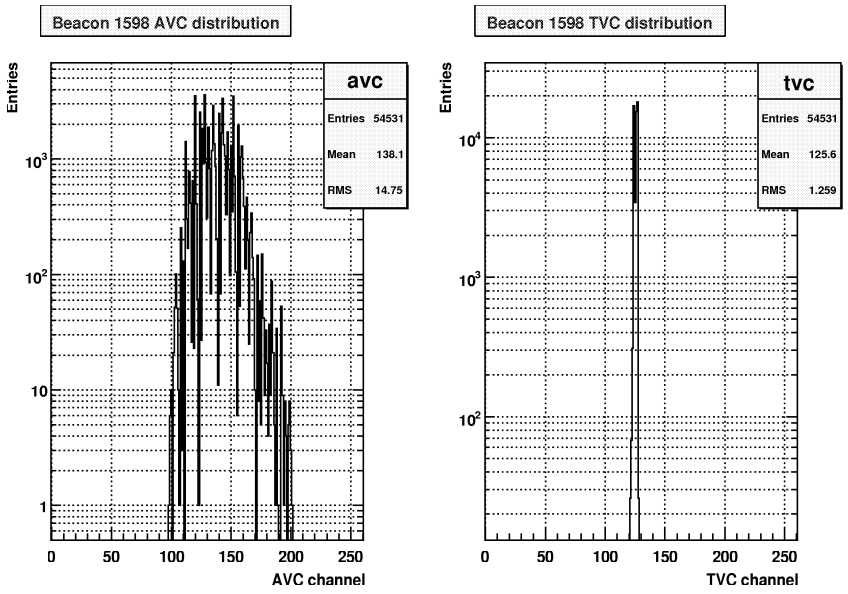


**Figure 5.2:** The AVC and TVC distributions from a MILOM LED Beacon run in the water, with maximum LED light intensity and one half of the maximun PMT gain.

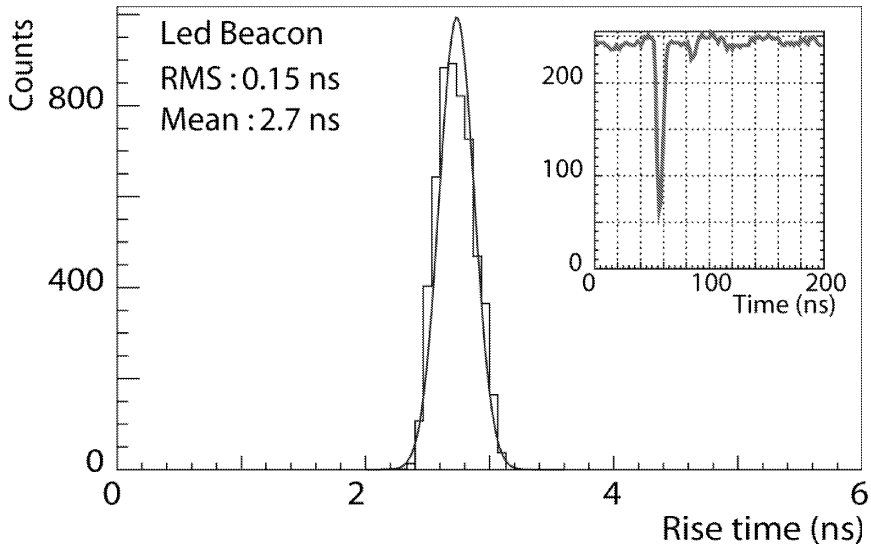


**Figure 5.3:** Rise time distribution of the LED Beacon once deployed in the sea. An example of a LED WF signal is overprinted in the upper right corner.

### 5.1.2 AVC and TVC OM distributions

Once it is confirmed that the beacon is flashing, the following test is to study how the AVC and TVC distributions of the Optical Modules are modified when the LED Beacon is flashing. The differences are evident if we compare the data recorded by the OMs in a run with the LED Beacon switched off, and the data recorded in a run with the LED Beacon flashing. In this sense, saturated hits appear in the AVC distribution when the LED Beacon is activated (Figure 5.4). Moreover, the LED Beacon synchronous light gives an overpopulated region in the TVC distribution (Figure 5.5).

### 5.1.3 Time resolution

A measurement of the time resolution and the time off-sets ($\Delta$t parameters) of the OMs can be done when the OMs are illuminated by the lower LED Beacon. First of all, we can measure the time difference between the LED light emission recorded in the ARS_6, and the signal recorded on each ARS (2 ARS per OM) of the 3 OMs. An example of these time difference distributions obtained in a MILOM LED Beacon run is shown in the Figure 5.6. In this computation, only saturated hits in charge (AVC) from both ARSs (LED Beacon and OM) were used. Therefore, the walk correction was not taken into account.

Since the LED Beacon is seen as a common isotropical light emitter for the 3 OMs placed above, another relevant measurement to do is the OM-OM time difference distribution obtained when the LED Beacon is flashing. These distributions allow us to measure the OM time off-sets in situ, and compare with the values previously measured

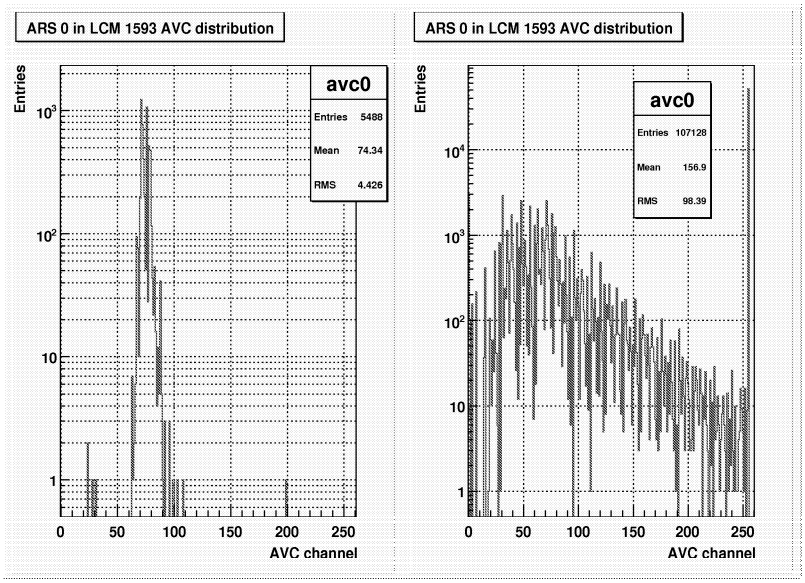


**Figure 5.4:** AVC distributions recorded by the ARS_0 of the OM_0 for a run with (right) and without (left) the LED Beacon flashing.

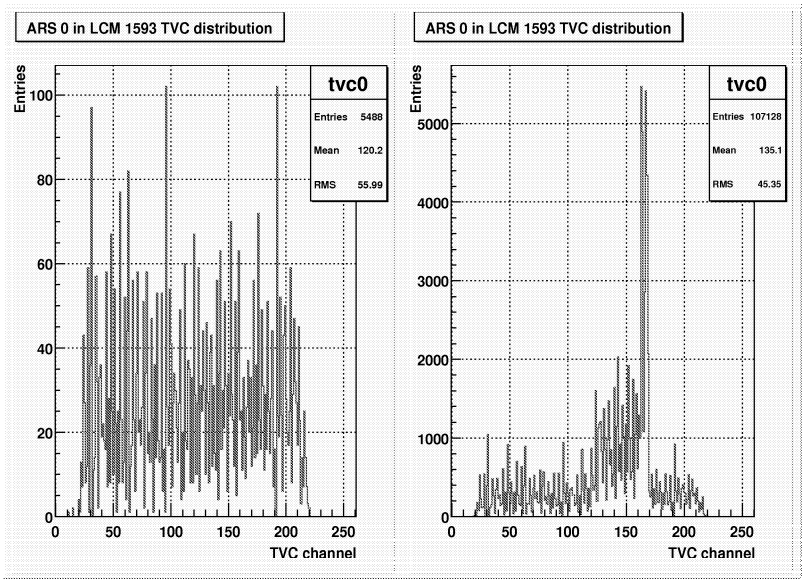


**Figure 5.5:** TVC distributions recorded by the ARS_0 of the OM_0 for a run with (right) and without (left) the LED Beacon flashing.

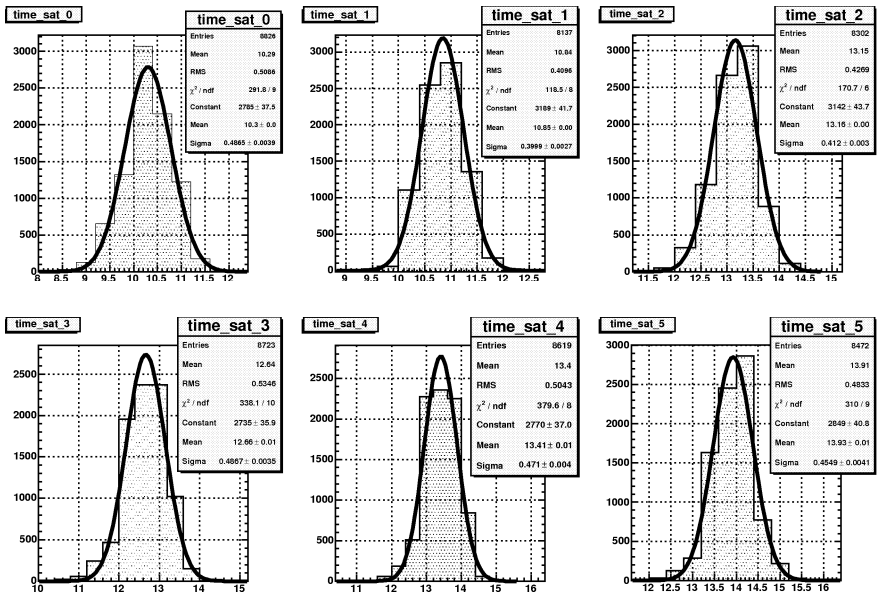


**Figure 5.6:** Time difference between the ARSs in the 3 OM of the MILOM line and the ARS_6 located in the lower LED Beacon.

in the dark room. The Figure 5.7 shows the time difference distributions between OMs (for both ARS in each OM) using the time recorded in the ARS_0 OM_0 as reference. The mean values of the time off-sets ($\Delta t$s) for one LED Beacon are summarized in the Table 5.1. As can be seen, the values are compatible with the ones obtained in the MILOM integration test at the dark room, with a maximun difference around $\sim 0.24$ ns between them.

From the OM-OM and OM-Beacon time difference distributions, it is possible to estimate the time resolution of one single OM. The average resolution for the OM-OM distribution is $\sigma \sim 0.56$ ns as can be seen in the Figure 5.7. Since this accounts for the fluctuations on both OMs, the resolution for one single OM can be estimated as $\sigma/\sqrt{2}$. The value for this run is $\sim 0.4$ ns.

For the OM-Beacon distribution, the time resolution for one single OM appears in the relation:

$$\sigma = \sqrt{\sigma_{OM}^2 + \sigma_{LOB}^2}$$

The $\sigma_{LOB}$ contribution is small due to the fast rise time of the small PMT (0.78 ns), so that the fluctuations are dominated mainly by the OM contribution. Therefore, the resolution obtained in the OM-Beacon distribution is slightly higher than the expected for one single OM. An averaged value of $\sigma \sim 0.45$ ns is obtained for the same run, in agreement with what is expected for the one single OM time resolution. The previous OM resolution values ($\sim 0.4$ ns) have been obtained for high intensity light pulses. Therefore, the resolution is fully dominated by the intrinsic electronic resolution and

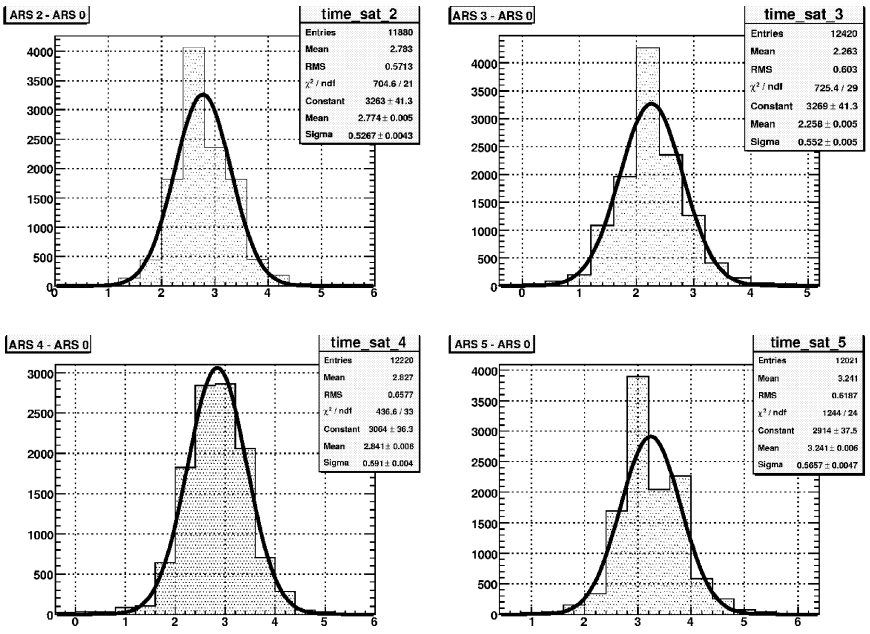


**Figure 5.7:** Time difference between the ARSs of the OM_1 and 2 in the MILOM storey using as reference the time recorded in the ARS_0 of OM_0.

not by the PMT transit time spread (TTS).

The OMs resolution together with the positioning resolution (∼10 cm) guarantees the expected angular accuracy of $< 0.3^o$ with the ANTARES telescope.

### 5.1.4 Time stability

The time stability of the LED Beacon flashing has also been checked. The parameter considered to measure the stability was the OM-Beacon time difference computed in the LED Beacon runs, during a 45 days period between 30th November, 2005 and 26th January, 2006. For these runs the PMT gain and the LED intensity were fixed to 1/2

| ARS | dark room $\Delta$t | sea $\Delta$t |
|---|---|---|
| 2 | 3.0 | 2.8 |
| 3 | 2.5 | 2.3 |
| 4 | 2.6 | 2.8 |
| 5 | 3.0 | 3.2 |

**Table 5.1:** Mean values of the time differences between the OMs taking the ARS_0 OM_0 as reference. Both values obtained in the dark room test and in the sea are shown.

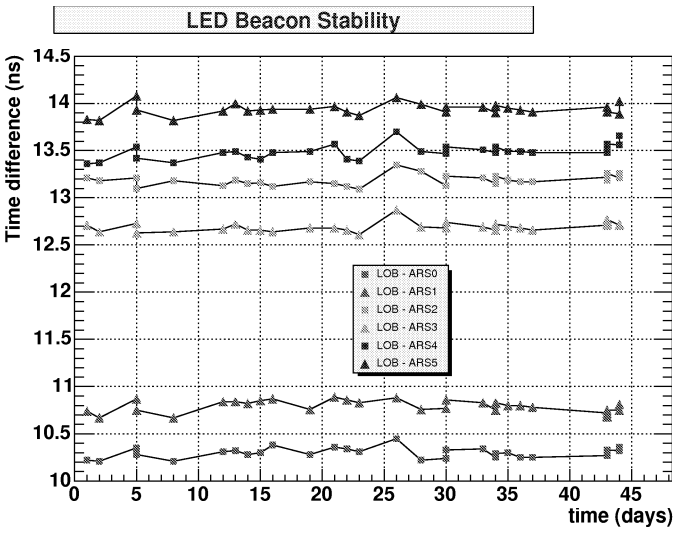


**Figure 5.8:** Time evolution of the mean time difference between the ARS_6 of the LED Beacon and the ARSs of the MILOM OMs. A good stability of the LED Beacon flashing can be noticed.

| ARS | Relative mean average (ns) | RMS | Max-min (ns) |
|---|---|---|---|
| 0 | 10.30 | 0.05 | 0.24 |
| 1 | 10.79 | 0.06 | 0.22 |
| 2 | 13.19 | 0.05 | 0.26 |
| 3 | 12.69 | 0.05 | 0.26 |
| 4 | 13.49 | 0.08 | 0.34 |
| 5 | 13.94 | 0.06 | 0.26 |

**Table 5.2:** Summary table with the results of the stability measurements.

of the maximum and the maximum values respectively. In the Figure 5.8 we can see the stability plot where the greater time difference for the same ARS is around 0.34 ns. Notice that the values of the time difference OM-Beacon are not absolute but relative. This is because the clock-phase and the time off-set ($\Delta$t) are not considered in the computation. The results are summarized in the Table 5.2, where the mean values of the OM-Beacon time differences for each ARS are presented, as well as the RMS and the maximum time difference. An idea of the systematic error can be obtained when more than one LED Beacon run is performed during the same day. For these runs, the greater time difference was around 0.1 ns.

Both TVC and AVC values of the LED Beacon, were also checked during the same time period (Figure 5.9). They were stable and showed a RMS of $\sim$ 0.8 and $\sim$ 0.2 channels respectively.

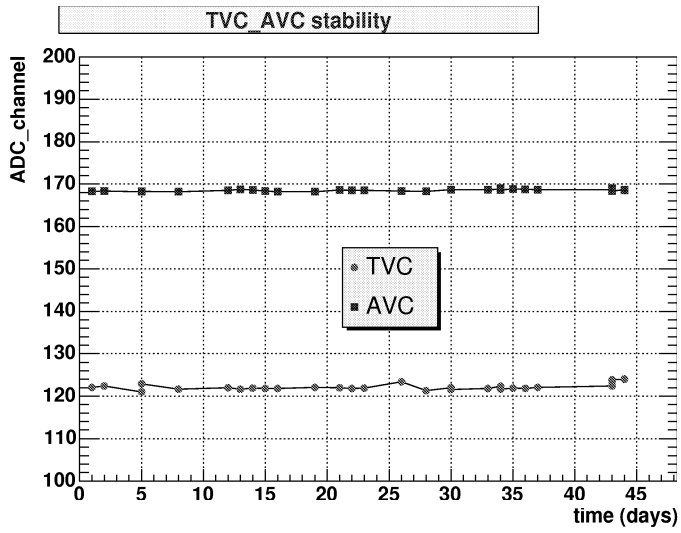


**Figure 5.9:** Time evolution of the AVC and TVC mean values taken from the LED Beacon daily runs during a 45 days period. A good stability in the LED Beacon runs can be noticed.

## 5.2 Results from the Laser Beacon.

The Laser Beacon, which does not emit in the upward direction to avoid sedimentation effects, is not devised to illuminate the MILOM line itself, but the other 12 lines of the detector. Therefore, very long runs are needed in order to get enough statistics of the laser hit coincidences. On the other hand, these hits are due mainly to scattered photons. In the Figure 5.10, examples of time difference distributions of Laser Beacon-OM and OM-OM from a 50 minutes run, are shown. In the Beacon-OM distribution, a clear tail can be seen probably due to the scattered photons. The OM-OM distribution is peaked around 0 as it is expected. However, the lack of statistics, as it is shown in the Figure 5.10 in the right side, together with the fact that the distribution is dominated by scattered photons provides a big 60 ns RMS which makes difficult to obtain any time off-set measurement with enough precision.

However, the laser photodiode signal has been analysed as well as its rise time, as was done in the integration tests. In the Figure 5.11 the rise time measurements for a Laser Beacon run can be seen, as well as a WF laser signal overprinted in the plot. Results are similar to the ones obtained in the dark room tests. This confirms the correct laser operation.

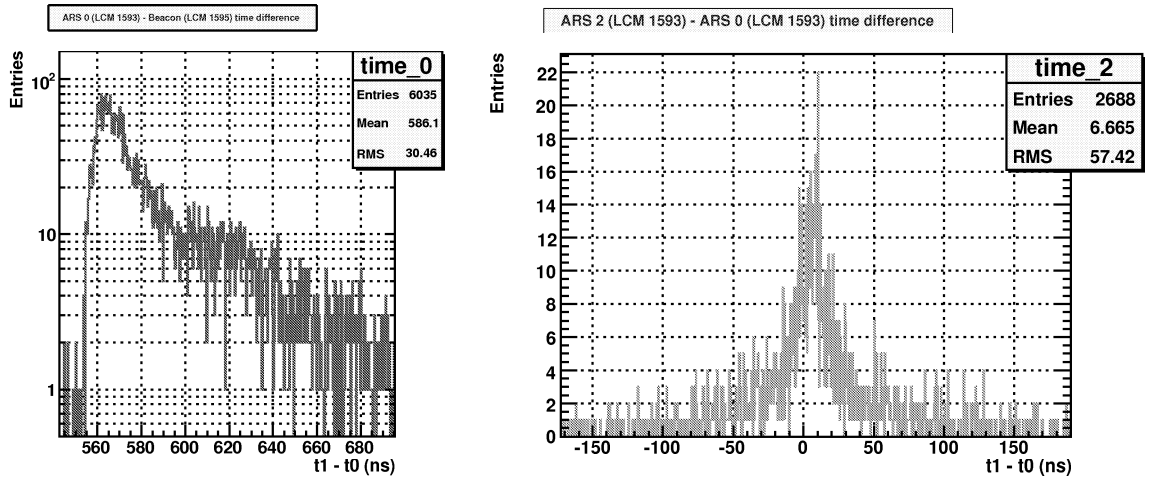


**Figure 5.10:** Time difference between ARS_0 from the MILOM storey, with respect to the Laser Beacon ARS, in a 50 minutes Laser Beacon run (left side). Time difference between ARS_2 from the MILOM storey, with respect to ARS_0, when the Laser Beacon is flashing (right side).

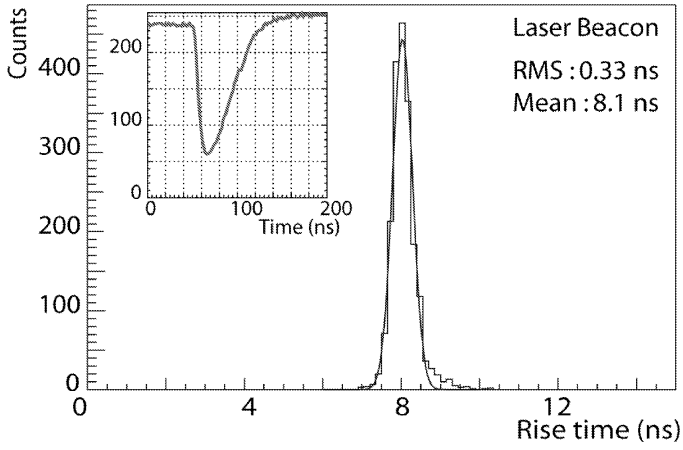


**Figure 5.11:** Rise time distribution of the Laser Beacon once deployed in the sea. An example of the laser WF signal is overprinted in the upper left corner.

# Conclusions

This research work is focussed mainly on the study of the Optical Beacons (LED and Laser) devised for the time calibration of the ANTARES neutrino telescope. The Optical Beacons play a fundamental role in the calibration task because they allow us to measure the time off-sets of the detector in situ. The water optical properties can also be studied with the Optical Beacon system and spatial calibration cross-checks can be performed.

In order to acquire a more general understanding of the detector, an introduction to the high-energy neutrino astronomy has been given, as well as a general overview of the ANTARES detector. A brief description of the time calibration systems has also given because of its intrinsic relation to the Optical Beacon system.

## Integration tests with Optical Beacons

The properties of the Optical Beacons have been explained in detail. In particular, the information about how they flash and how the flash time emission is measured.

First of all, the test bench and the test procedures developed in the Valencia laboratory to test and accept the Optical Beacons, are explained. In this sense, this work has contributed to establish the measures and methods to assure a correct operation of the Optical Beacons once they are deployed in the sea.

The studies made in Valencia has been complemented with the tests performed in the integration phase with the Optical Beacons being controlled by the ANTARES DAQ system.

The most relevant results of these tests are the following:

- **LED Beacon**:

  - A synchronization better than 0.3 ns face to face is achieved in the Valencia laboratory for the LED Optical Beacons. This synchronization level is good enough and does not affect the rise edge of the PMT signal when all the LEDs are flashing, as has been shown in the Monte Carlo simulation. A sharp and stable rise edge is crucial to achive a good time resolution.

  - The charge and time distributions obtained for the LED Beacon with the DAQ system, show a perfect agreement with the distributions obtained in the test

bench at Valencia, both for the whole beacon flashing and for the beacon flashing by groups.

- Although the noise level has been reduced significantly from the first test, an appropriate one-by-one election of the L0 threshold is necessary to avoid the noise signals.

- **Laser beacon**:

- The Laser Beacon provides an energy stable signal in time which can be measured by its built-in photodiode with a time jitter lower than 50 ps.

- The charge and time distributions obtained for the Laser Beacon with the DAQ system, show a perfect agreement with the distributions obtained in the test bench at Valencia.

- The beacons working on the MILOM line and Line 1 once in situ, have shown a perfect operation as was expected from the Valencia and integration tests.

## First results in the sea with the instrumentation line

The good results of the tests concerning the Optical Beacons in the different laboratories has culminated with the instrumentation line (MILOM) deployment. With the MILOM, the first signals from the Optical Beacons were recorded, and the first in-situ time calibration parameters measurements, were performed.

The most significant results obtained with the MILOM line are the following:

- The first Optical Beacon signals from the internal small PMT (LED Beacon) and built-in photodiode (Laser Beacon), were recorded in the beacon ARSs.

- Similar charge, time and rise time distributions were measured for the beacons, both for the line in the laboratory and for the line in the sea.

- The AVC and TVC distributions of the OMs were clearly modified when the beacon was flashing.

- The time differences between the OMs showed a good agreement with the calibration parameters previously measured in the laboratory.

- The LED Beacon has shown a good reliability during the first year of MILOM operation, as has been seen in the stability studies.

- The beacon measurements in the MILOM have shown a relative time resolution of $\sim 0.4$ ns for the Optical Modules. Together with the performance of the acoustic positioning system ($\sim$ 10 cm resolution), this time resolution allows to achieve an angular resolution of $< 0.3$ degree with the ANTARES detector. This angular

resolution will permit us, once the whole detector will be deployed, the detection of extraterrestrial sources with an unprecedented accuracy in neutrino telescopes.

# Bibliography


[1] Hess, V.F., "Über Beobachtungen der durchdringenden Strahlung bei sieben Freiballonfahrten," *Physik. Zeitschr.,* **13**, (1912): 1084.

[2] Simpson, J.A., "Elemental and Isotopic Composition of the Galactic Cosmic Rays," *Annual Review of Nuclear and Particle Science,* **33**, (2000): 323–382.

[3] Greisen, K., "End to the cosmic-ray spectrum?," *Phys. Rev. Lett.,* **16**, (1966);

Zatsepin, G.T. and Kuzmin V.A., "Upper limit of the spectrum of cosmic rays," *Pisma Zh. Eksp. Teor.,* **4**, (1966): 114.

[4] Fermi, E., "On the origin of the cosmic radiation," *Phys. Rev.,* **75**(8), (1949): 1169.

[5] Protheroe, R.J. and Clay, R.W., "Ultra High Energy Cosmic Rays," *Publ.Astron.Soc.Pac.,* **21**, (2004): 1–22.

[6] Lagage, P.O. and Cesarsky C.J., "The maximum energy of cosmic rays accelerated by supernova shocks," *Astron. Astrophys.,* **125**, (1983): 249–257.

[7] Bednarek, W. and Protheroe, R.J., "Ontribution of nuclei accelerated by gamma-ray pulsars to cosmic rays in the Galaxy," *Astroparticle Physics,* **16**, (2002): 397–409.

[8] Biermann, P.L., "Cosmic rays. 1.The cosmic ray spectrum between $10^4$ GeV and $3{\times}10^9$ GeV," *Astronomy and Astrophysics,* **271**, (1993): 649.

[9] Erlykin, A.D. and Wolfendale A.W., "On the Origin of Cosmic Rays in the PeV - EeV Energy Range," *29th International Cosmic Ray Conference Pune,* **00**, (2005): 101–104.

[10] Protheroe R.J and Johnson, P.A., "Are topological defects responsible for the 300 EeV cosmic rays?," *Nucl.Phys.Proc.Suppl.,* **48**, (1996): 485–487.

[11] Halzen, F. and Hooper D., "Neutrinos from the Annihilation or Decay of Superheavy Relic Dark Matter Particles," *Proceedings of Dark Matter 2002,* (2002).

[12] Wibig, T. and Wolfendale A.W., "No 'cut off' in the High Energy Cosmic Ray Energy Spectrum," (2004), astro-ph/0406511.

[13] Kanbach, G. et al., "The project EGRET (Energetic Gamma-Ray Experiment Telescope) on NASA's Gamma-Ray Observatory (GRO)," *Space Sci.Rev.,* **49**, (1988): 69.

[14] MAGIC Collaboration: Albert, J. et al., "Discovery of VHE gamma-ray emission from 1ES1218+30.4," *The Astrophysical Journal,* **642**), (2006): L119–L122.

[15] Bahcall, J.N. and Serenelli A.M., "New solar opacities, abundances, helioseismology, and neutrino fluxes," *The Astrophysical Journal,* **621**, (2005): L85–L88.

[16] Gaisser, T.K. and Honda, M., "Flux of atmospheric neutrinos," *Annu. Rev.Nucl.Part.Sci.,* **52**, (2002): 153.

[17] Waxman, E. and Loeb, A., "TeV Neutrinos and GeV Photons from Shock Breakout in Supernovae," *Phys. Rev. Lett.,* **87**, (2001): 071101.

[18] Aharonian, F.A. et al., "High-energy particle acceleration in the shell of a supernova remnant," *Nature,* **432**, (2004): 75.

[19] Khélifi, B. et al., "TeV gamma-ray observations of pulsar wind nebulae with the HESS detector," *Advances in Space Research,* **35**, (2005): 1148–1151.

[20] Wagnera, R.M. et al., "Article Title," *29th International Cosmic Ray Conference Pune,* **00**, (2005): 101–106.

[21] Bednarek, W.; Burgio, G.F. and Montaruli, T. "Galactic discrete sources of high energy neutrinos," *New Astron.Rev.,* **49**(1), (2005): 1–21.

[22] Kouveliotou, C.; Duncan, R. and Thompson, C., "Magnetars," *Scientific American,* (February 2003): 34–41.

[23] Zhang, B. et al., "High-energy neutrinos from magnetars," *The Astrophysical Journal,* **595**, (2003): 346–351.

[24] Gaisser,T.K.; Halzen, F. and Stanev, T., "Particle astrophysics with high energy neutrinos," *Physics Reports,* **258**, (1995): 173–236.

[25] Distefano, C.; Guetta, D.; Waxman, E. and Levinson A., "Neutrino Flux Predictions for Known Galactic Microquasars," *The Astrophysical Journal,* **575**, (2002): 378–383.

[26] Burgio, G.F., "Detecting high-energy neutrinos from microquasars with the ANTARES telescope," *Proceedings V Microquasar Workshop,* (2004).

[27] Aharonian, F. et al., "The H.E.S.S. survey of the Inner Galaxy in very high-energy gamma-rays," *Astrophys.J.,* **636**, (2006): 777–797.

[28] Hill, G.C., "Detecting neutrinos from AGN: New fluxes and cross sections," *Astrop. Phys.,* **6**, (1997): 215–217.

[29] Stecker, F.W., "High-energy neutrinos from active galactic nuclei," *Phys. Rev. Lett.,* **66**, (1991): 2697.

[30] Protheroe, R.J., "High Energy Neutrinos from Blazars," *Proc. of the IAU Colloquium 163, Accretion Phenomena and Related Outflows,* (1996), astro-ph 9607165 .

[31] Stecker, F.W., "A Note on High Energy Neutrinos from AGN Cores," *Phys.Rev. D,* **72**, (2005): 107301.

[32] Piran, T., "Gamma-ray bursts and the fireball model," *Physics Reports,* **314**, (1999): 575–667.

[33] Dar, A. and De Rújula, A., "Towards a complete theory of gamma-ray bursts," *Physics Reports,* **405**, (2004): 203–278.

[34] Halzen, F., "Lectures on High-Energy Neutrino Astronomy," *Lectures presented at the International WE Heraeus Summer School on Physics with Cosmic Accelerators,* (2004), astro-ph/0506248.

[35] Waxman, E. and Bahcall, J., "High Energy Neutrinos from Cosmological Gamma-Ray Burst Fireballs," *Phys. Rev. Lett.,* **78**(12), (1997): 2292–2295.

[36] Kachelriess, M., "Ultimate Energy Particles in the Universe," *Comptes Rendus Physique,* **5**, (2004): 441–452, hep-ph/0406174.

[37] Lai, K.C. and Chen, P., "A Lower Bound on Neutrino Mass and Its Implication on The Z-burst Scenario," (2005), astro-ph/0511340.

[38] Gelmini, G. and Kusenko, A., "Unstable superheavy relic particles as a source of neutrinos responsible for the ultrahigh-energy cosmic rays," *Phys.Rev.Lett.,* **84**, (2000): 1387.

[39] Romeyer, A., "Antares Sensitivity to Diffuse High Energy Neutrino Fluxes," *Proceedings ElectroWeak Interactions and Unified Theories,* (2002).

[40] Waxman, E. and Bahcall, J., "High energy neutrinos from astrophysical sources: An upper bound," *Phys. Rev. D,* **59**, (1998): 023002.

[41] Loeb, A. and Waxman E., "The Cumulative Bakground of High-Energy Neutrinos from Starburst Galaxies," (2006), astro-ph/0601695.

[42] SNO Collaboration: Ahmad, Q.R. et al., "Direct Evidence for Neutrino Flavor Transformation from Neutral-Current Interactions in the Sudbury Neutrino Observatory," *Phys.Rev.Lett.,* **89**, (2002): 011301.

[43] K2K Collaboration: Aliu, E. et al., "Evidence for muon neutrino oscillation in an accelerator-based experiment," *Phys.Rev.Lett.,* **94**, (2005): 081802.

[44] Markov, M.A., *Proceedings of the Annual International Conference on High Energy Physics at Rochester,*(New York, 1960).

[45] Gandhi, R. et al., "Neutrino Interactions at Ultrahigh Energies," *Phys.Rev. D,* **58**, (1998): 093009.

[46] Particle Data Group: Eidelman, S. et al., "Review of Particle Physics," *Phys. Lett. B,* **592**, (2004): 1.

[47] ANTARES Collaboration: Aslanides, E. et al., "A Deep Sea Telescope for High Energy Neutrinos," *preprint CPPM-P-1999-02, DAPNIA 99-01, IFIC/99-42, SHEF-HEP/99-06,* (1999), astro-ph/9907432.

[48] ANTARES Collaboration: Amram, P. et al., "Background Light in Potential Sites for the ANTARES Undersea Neutrino Telescope," *Astropart.Phys.,* **13**, (2000): 127–136.

[49] ANTARES Collaboration: Amram, P. et al., "Sedimentation and Fouling of Optical Surfaces at the ANTARES Site," *Astropart.Phys.,* **19**, (2003): 253–267.

[50] ANTARES Collaboration: Aguilar, J.A. et al., "Transmission of light in deep sea water at the site of the Antares neutrino telescope," *Astropart.Phys.,* **23**, (2005): 131–155.

[51] ANTARES Collaboration: Amram, P. et al., "The ANTARES Optical Module," *Nucl.Instrum.Meth. A,* **484**, (2002): 369–383.

[52] ANTARES Collaboration: Aguilar, J.A. et al., "Study of Large Hemispherical Photomultiplier Tubes for the ANTARES Neutrino Telescope," *Nucl.Instrum.Meth. A,* **555**, (2005): 132–141.

[53] Heck, D. et al., "CORSIKA: A Monte Carlo Code to Simulate Extensive Air Showers," *Forschungszentrum Karlsruhe Report,* **FZKA-6019**, (1998).

[54] Scapparone, E., "HEMAS: a Monte Carlo code for hadronic, electromagnetic and TeV muon components in air shower," *Invited talk at International Workshop on Simulation and analysis methods for large neutrino detectors,* (1998), physics/9902043.

[55] Kalmykov, N.N.; Ostapchenko, S.S. and Pavlov, A.I., "Quark-gluon-string model and EAS simulation problems at ultra-high energies," *Nucl.Phys.B (Proc. Suppl.),* **52B**, (1997): 17–28.

[56] Ranft, J., "Dual parton model at cosmic ray energies," *Phys.Rev.D,* **51**, (1995): 64–84.

[57] Antonioli, P., "A three-dimensional code for muon propagation through the rock: MUSIC," *Astro. Phy.,* **7**, (1997): 357.

[58] Sokalski, I.A.; Bugaev, E.V. and Klimushin, S.I., "MUM: flexible precise Monte Carlo algorithm for muon propagation through thick layers of matter," *Phys. Rev. D,* **64**, (2001): 074015.

[59] Carminati, G; Margiotta, A and Spurio, M., "MUPAGE: a MUon GEnerator from PArametric formulas," *ANTARES internal note. ANTARES-Phys/2006-003.*

[60] Bailey D.J.L., "Genhen v5r1: Software Documentation," *ANTARES internal note. ANTARES-Software/2002-004.*

[61] Ingelman, G.; Edin, A. and Rathsman J., "LEPTO 6.5 - A Monte Carlo Generator for Deep Inelastic Lepton-Nucleon Scattering," *Comput.Phys.Commun.,* **101**, (1997): 108–134.

[62] Pumplin, J. et al., "New Generation of Parton Distributions with Uncertainties from Global QCD Analysis," *JHEP,* **0207**, (2002): 012.

[63] Sjostrand, T., "PYTHIA 5.7 and JETSET 7.4 Physics and Manual," *Comput.Phys.Commun.,* **82**, (1994): 74, hep-ph/9508391.

[64] Barr, G.D., "The separation of signals and background in a nucleon decay experiment," *PhD thesis, University of Oxford,* (United Kingdom, 1987).

[65] Jadach, S. et al., "The $\tau$ decay library TAUOLA, version 2.4Article Title," *Comput.Phys.Commun.,* **76**, (1993): 361.

[66] Navas, S. and Thompson, L., "KM3 User Guide and Reference Manual," *ANTARES internal note. ANTARES-Software/1999-011.*

[67] Brunner, J., "GEASIM: User manual," *ANTARES internal documentation.* http://antares.in2p3.fr/internal/software/geasim.html.

[68] Romeyer, A. and Stolarczyk, Th., "Reconstruction algorithms: a handbook for developers," *ANTARES internal note.ANTARES-SOFT-2001-001.*

[69] DUMAND Collaboration: Babson, J. et al., "Cosmic-ray muons in the deep ocean," *Phys.Rev.D,* **42**, (1990): 3613.

[70] Wischnewski, R., "The Baikal Neutrino Telescope - Results and Plans," *Int.J.Mod.Phys. A,* **20**, (2005): 6932–6936.

[71] Lowder, D.M. et al., "Observation of muons using the polar ice cap as a Cerenkov detector," *Nature,* **353**, (26 September 1991): 331–333.

[72] The IceCube Collaboration: Achterbergt, A. et al., "The IceCube Collaboration: contributions to the 29th International Cosmic Ray Conference (ICRC 2005), Pune, India, Aug. 2005," (2005), astro-ph/0509330.

[73] Goldschmidt, A., "The IceCube," *Proceedings of the 27th International Cosmic Ray Conference,* (Hamburg, Germany: 7-15 August 2001): 1237–1240.

[74] Klein, S.R., "First Results from IceCube," *presented at PANIC05,* (Santa Fe 24-28 October 2005), astro-ph/0601269.

[75] The NESTOR Collaboration: Aggouras, G. et al., "Operation and performance of the NESTOR test detector," *Nucl. Instr. and Meth. in Phys. A,* **552**, (2005): 420–439.

[76] The NESTOR Collaboration: Aggouras, G. et al., "A measurement of the cosmic-ray muon flux with a module of the NESTOR neutrino telescope," *Astroparticle Physics,* **23**, (2005): 377–392.

[77] Capone, A., "Site characterization for a $km^3$ scale deep underwater astrophysical neutrino observatory in the mediterranean sea," *Prepared for 26th International Cosmic Ray Conference,* (Salt Lake City, Utah, 17-25 August 1999).

[78] "Design Study for a Deep Sea Facility in the Mediterranean for Neutrino Astronomy and Associated Sciences," http://www.km3net.org/publications.php.

[79] Aguilar, J.A., "MILOM's LED beacon results. High Intensity," *talk in ANTARES Collaboration meeting,* (Ravenna, Italy 14-17 November 2005).

[80] Kapustinsky, J.S. et al., "A fast timing light pulser for scintillation detectors," *Nucl. Instr. and Meth. in Phys. A,* **241**, (1985): 612–613.

[81] Carmona, E et al., "Measurement of the jitter of the time difference between the Laser Beacon internal photodiode and several light detectors used as external references," *ANTARES internal note. ANTARES-Cali/2002-001.*

[82] Oracle Corporation. http://www.oracle.com/.

[83] Lachartre, D., "ARS1 Analogue Ring Sampler & ARS_CONV Users Manual Version 1.9," *ANTARES internal note.ANTARES-Elec/2000-6.*

[84] Carmona, E., "Estudio de fotomultiplicadores de gran fotocátodo para el telescopio submarino de neutrinos ANTARES," *Diploma thesis, Universitat de València* (1999).

[85] Carmona, E., "Study of the event reconstruction and expected performances for the point-like sources of the future ANTARES neutrino telescope," *PhD thesis, Universitat de València* (2003).

[86] Heijboer, A., "Track reconstruction and Point Source Searches with ANTARES," *PhD thesis, NIKHEF, Amsterdam* (2004).

[87] Zornoza, J.D., "Sensitivity to Diffuse Fluxes and Energy Spectrum Reconstruction in the ANTARES Neutrino Telescope," *PhD thesis, Universitat de València* (2005).

[88] ANTARES Collaboration: Aguilar, J.A. et al., "The data acquisition system of the ANTARES neutrino telescope," in preparation.